POLITECNICO
MILANO 1863

School of industrial and information Engineering
Master of science in Engineering Physics

Broadband Stimulated Raman Scattering: towards time-encoded detection

Supervisor:
Prof. Dario POLLI
Co-supervisor:
Carlo Michele VALENSISE

Author:
Federico VERNUCCIO
Student ID: 897993

Academic Year 2018-2019

The process of scientific
discovery is, in effect,
a continual flight from wonder.

Albert Einstein

Abstract

Coherent Raman scattering (CRS) is a class of third-order light-matter interactions used for non-invasive, label-free and non-destructive imaging in biological samples, with application in the field of biology, medicine and chemistry. It is based on the Raman scattering effect that exploits the vibrational modes of molecules to differentiate them. Indeed, each sample has a chemical structure that determines a peculiar vibrational spectrum, which provides a signature that can be exploited for the identification of molecules. The two most widely applied implementations of CRS are Coherent Anti-Stokes Raman scattering (CARS) and Stimulated Raman Scattering (SRS).
In this thesis, the theory, implementations and applications of Coherent Raman Scattering to perform imaging and spectroscopy will be discussed. Chapter 1 describes all the physical processes at the basis of CRS and its main implementations. Chapter 2 deals with the main physical effects leading to white light generation. Chapter 3 explains linear propagation in dielectric media of ultrashort-pulses, emphasizing the topic concerning pulse propagation in single-mode fibers and Chapter 4 describes Frequency Resolved Optical Gating (FROG), a technique to characterize ultrashort pulses.
Chapter 5 focuses the attention on the description of the experimental setup which has been completely realized in the laboratory by me and my supervisors. The setup is meant to implement broadband CRS, through which one can acquire a full Raman spectrum of the sample under analysis, allowing one to distingush different components within a heterogeneous system. Using a 268 fs laser pulse at 1035 nm , 60 W average power and working at 2 MHz repetition rate, we generate two beams. The first one, the pump, is a narrowband beam at 1035± 1 nm and 1 ps duration shrunk in bandwidth by means of an etalon; the second one, called 'Stokes', is produced through white light generation in a YAG-crystal such that it has a broad spectrum spanning 1050-1500 nm and 200 fs duration. These two beams are spatially and temporally synchronized and collinearly sent to the sample. After the sample, the vibrational spectrum is retrieved measuring the CARS signal by means of a spectrometer and implementing two novel time-encoded techniques for SRS detection, namely Photonic-Time Stretch SRS (PTS-SRS) and Fourier Transform SRS (FT-SRS). Together with the setup description, all the measurements and techniques involved in the characterization of the pulses are discussed. Eventually, measurements of CARS and FT-SRS spectra of some solvents, generally used as test samples, are shown.

Sommario

Lo Scattering Raman Coerente (dall'inglese *Coherent Raman Scattering*, CRS) è una classe di interazioni radiazione-materia del terzo ordine utilizzate per l'imaging non invasivo, senza marcatori e non distruttivo in campioni biologici, con applicazione nel campo della biologia, della medicina e della chimica. Si basa sull'effetto di scattering Raman che sfrutta i modi vibrazionali delle molecole per differenziarle. In effetti, ogni campione ha una struttura chimica che determina uno spettro vibrazionale peculiare. Tale spettro fornisce una firma che viene sfruttata per l'identificazione delle molecole. Le due implementazioni più ampiamente utilizzate di CRS sono lo Scattering Coerente Raman Anti-Stokes (indicato anche con l'acronimo inglese CARS, da *Coherent anti-Stokes Raman Scattering*) e lo Scattering Raman Stimolato (indicato con l'acronimo inglese SRS, da *Stimulated Raman Scattering*).

In questa tesi verranno discussi la teoria, le implementazioni e le applicazioni dello Scattering Raman Coerente per la spettroscopia e la microscopia. Il capitolo 1 descrive tutti i processi fisici alla base del CRS e le sue principali implementazioni. Il capitolo 2 tratta i principali effetti fisici che portano alla generazione di luce bianca. Il capitolo 3 spiega la propagazione lineare in mezzi dielettrici di impulsi ultracorti, ponendo l'accento sulla propagazione degli impulsi nelle fibre a singolo modo e il capitolo 4 descrive la FROG (*Frequency Resolved Optical Gating*), una tecnica per caratterizzare gli impulsi ultracorti.

Il capitolo 5 focalizza l'attenzione sulla descrizione della configurazione sperimentale che è stata completamente realizzata in laboratorio da me e dai miei supervisori. Lo schema sperimentale ha lo scopo di implementare il CRS a banda larga, attraverso il quale è possibile acquisire uno spettro Raman completo del campione in analisi, consentendo di distinguere componenti diversi all'interno di un sistema eterogeneo. Usando un impulso laser a 268 fs a 1035 nm, 60 W di potenza media e lavorando a una frequenza di ripetizione di 2 MHz, generiamo due raggi. Il primo, la pompa, è un fascio a banda stretta a 1035$\pm$1 nm e durata 1 ps, la cui banda è ristretta per mezzo di un etalon; il secondo, chiamato *Stokes*, è prodotto attraverso la generazione di luce bianca in un cristallo YAG in modo tale da avere un ampio spettro che copre dai 1050 ai 1500 nm e durata 200 fs. Questi due raggi sono sincronizzati spazialmente e temporalmente e inviati collinearmente al campione. Dopo il campione, lo spettro vibrazionale viene recuperato misurando il segnale CARS per mezzo di uno spettrometro e implementando due nuove tecniche codificate nel tempo per il rilevamento del segnale SRS, vale a dire *Photonic Time Stretch-SRS* (PTS-SRS) ed SRS a trasformata di Fourier (*Fourier Transform SRS*, FT-SRS) . Insieme alla descrizione del setup,

vengono discusse tutte le misure e le tecniche coinvolte nella caratterizzazione degli impulsi. Alla fine, vengono mostrate le misurazioni degli spettri CARS e FT-SRS di alcuni solventi, generalmente utilizzati come campioni di prova.

Contents

List of Figures

List of Tables

Chapter 1

Coherent Raman scattering

1.1 Introduction

This chapter introduces Coherent Raman scattering (CRS) microscopy, starting from the motivational point of view, highlighting the main advantages this technique offers, passing through a theoretical description of the optical processes involved and finally presenting the state of the art of the main implementations in microscopy.

Nowadays, in life science researchers aim in the realization of microscopic technique capable of characterize the main components of an investigated sample, thus giving a complete characterization of its morphological details at the submicrometer scale. Different approaches have been used in the history to do that, each one different from the other for the level of sensitivity and molecular selectivity they offer [1]. The most popular imaging technique used in biology is the fluorescence microscopy [2] [3]. It uses exogenous (such as dyes or semiconductor quantum dots), or endogenous (such as fluorescent proteins), markers, which, on the one hand, offers a superb sensitivity down to the single molecule limit, but, on the other hand, can perturb the investigated system [12] [13]. This is particularly true for small molecule, for which the size of the marker is comparable or even bigger than that of the molecule itself. Finally, cells suffer phototoxicity which is further enhanced using fluorescent labels. For this reason there is the necessity of intrinsic, label-free imaging methods in life science and bio-medicine that do not require the addition of any fluorescent molecule. One label-free method is the vibrational absorption microscopy [4] that uses mid-infrared (MIR) light ($\lambda = 3 - 10\mu m$) which is resonant with the vibrational transitions of the specimen. However, the required long wavelengths result in poor spatial resolution and very short penetration depth due to water absorption.

Spontaneous Raman scattering [5] [21] overcomes these limits using a single mode in the visible or near-infrared at frequency ω_p (pump) to generate a mode at frequency ω_s (Stokes), that is emitted spontaneously. The characteristic vibrational frequency can be derived by doing the difference of the two frequency. During the process, the pump excites the molecule to a virtual state and then the system spontaneously relaxes towards the ground state emitting a photon at ω_s (Fig. 1.1). Since a molecule has several vibrational modes, the resulting spontaneous,

incoherent response is a wide spectrum red-shifted with respect to the pump frequency.

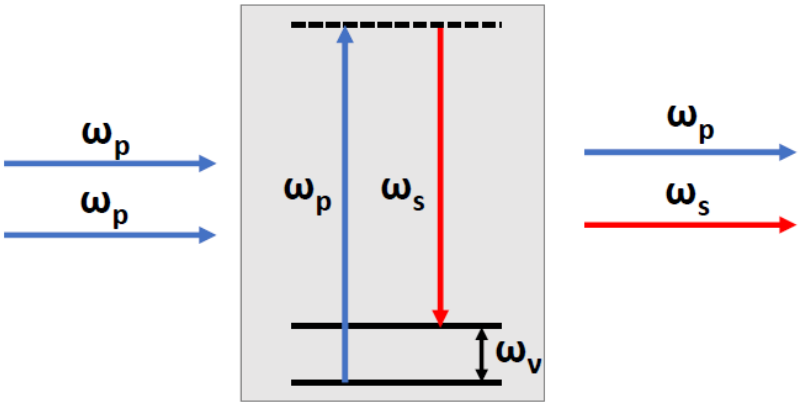

Figure 1.1: Schematic of the energy levels involved in Spontaneous Raman scattering.

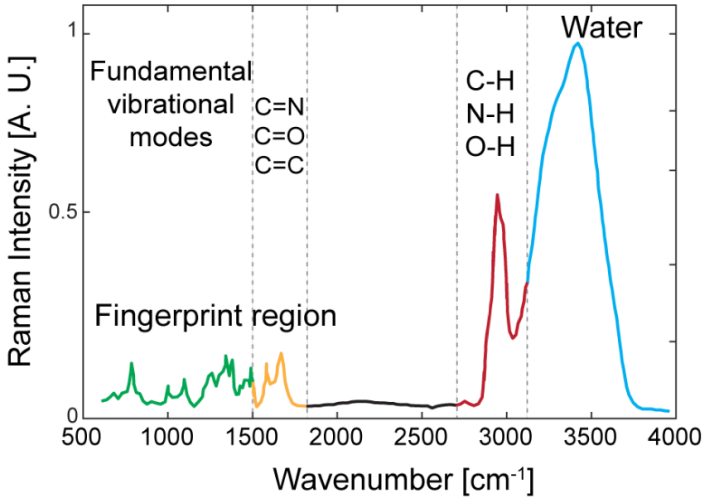

Figure 1.2: Stimulated Raman spectrum of P22 virus at 80 μg μL^{-1} concentration in H_2O buffer at 20° C, highlighting most relevant vibrational transitions. From [11]

In a typical Raman spectrum there are two vibrational frequency intervals of interest, belonging to specific chemical structures. The most important interval for chemical identification is the so-called fingerprint region in the low wavenumber (600-1800 cm^{-1}) portion of the spectrum. Here the spectrum contains the contributions from proteins and nucleic acids. In particular, these vibrations are associated to the stretching or deformation of carbon atoms bonded with nitrogen (C-N stretch), hydrogen (C-H rock, bend or scissoring) or other carbon atoms (C-C stretch). Moreover, in the 1500-1800 cm^{-1} frequency interval, you can identify double bonds such as C=N, C=O and C=C. The second region of interest

is the high wavenumber window (2700-3100 cm^{-1}) where you can identify the stretching of the hydrogen bonds (C-H, N-H, O-H). Eventually, for wavenumber beyond 3100 cm^{-1} a very broad peak of water is found (Fig. 1.2).
The main drawback of SR microscopy is that it has a very low scattering cross-section, about 10-12 orders of magnitude lower than the absorption cross-section of molecules, resulting in a weak incoherent emitted signal.

Compared to spontaneous Raman scattering, CRS techniques can produce much stronger vibrationally sensitive signals [6] [7]. CRS employs a sequence of spatially and temporarily synchronized narrowband light pulses to set up and detect a vibrational coherence within the ensemble of molecules inside the laser focus [14] [15]. In particular, it uses a combination of two light pulses at frequency ω_p (pump) and ω_s (Stokes), respectively, impinging onto the sample such that the coherent Raman interaction depends on oscillatory motions in the material at the frequency $\omega_\nu = \omega_p - \omega_s$. Through this process, it is possible to make all the molecules within the focal volume of the two beams to oscillate in phase such that the resulting signal is enhanced with respect to the incoherent Spontaneous Raman (SR) counterpart. The popularity of CRS techniques [16] [17] in optical microscopy is intimately related to these much improved signal levels, which have enabled the fast scanning capabilities of CRS microscopes [20]. In general, CRS techniques offer a more detailed control of the Raman response of the medium than what is available through spontaneous Raman techniques and allow a more direct probing of the molecular coherences that govern the Raman vibrational response [18] [19]. CRS thus provides the following advantages:

- In comparison to fluorescence microscopy it is label free, since it does not require fluorophores or staining;
- It works out of resonance, that is there is no population transfer into the electronic states, minimizing photobleaching and damage to biological samples;
- It gives a much stronger signal with respect to that of SR microscopy, allowing higher imaging speeds;
- Being a nonlinear microscopy, it works only into the focal volume, allowing much more control of the response of the medium and 3D sectioning capability;
- Since it uses wavelengths in the visible or NIR region of the spectrum, it guarantees an higher penetration depth through the tissues with respect to MIR techniques. Furthermore, working with wavelength into the infrared it reduces phototoxicity and damage of the cells;

The two most important CRS techniques which are used to study the vibrational spectrum of the molecules are coherent anti-Stokes Raman scattering (CARS) and stimulated Raman scattering (SRS). In the SRS processes, the interactions with the pump and Stokes fields leads to a stimulated emission at the frequency of the

Stokes beam, resulting in a Stokes-field amplification (stimulated Raman gain, SRG) and in a pump-field attenuation (stimulated Raman loss, SRL). While, in the CARS process, the vibrational information is retrieved by making the sample interact with a third beam, called probe beam, generating a coherent radiation at the anti-Stokes frequency ($\omega_{aS} = \omega_{pr} + \omega_\nu$). Typically, this third beam is the pump itself, thus having $\omega_{aS} = \omega_p + \omega_\nu$.

1.2 Nonlinear Optical Processes

Both linear and nonlinear optical processes can be understood by considering the interaction between the field of the electromagnetic radiation and the charged particles of the sample. For a field in the visible or near-infrared the oscillating frequency is around 10^3 THz. Such driving frequency is too high for the nuclei to follow adiabatically the oscillations of the fields, while the electrons being lighter can follow them. As a result of this interaction, the bound electrons are slightly displaced from their equilibrium positions and an induced electric dipole moment arises [7]:

$$\vec{\mu}(t) = -e * \vec{r}(t) \tag{1.1}$$

where e is the charge of the electron and $\vec{r}(t)$ the extent of the displacement. From classical electromagnetism, the macroscopic polarization of the sample is:

$$\vec{P}(t) = N\vec{\mu}(t) \tag{1.2}$$

If the applied electric field is weak (compared to the field that binds the electrons to the nuclei), we can consider that the displacement of the electron from its equilibrium position is small enough that the binding potential can be approximated as an harmonic potential. Consequently the polarization will depends linearly on the electric field. So, it is possible to write:

$$\vec{P}(t) = \epsilon_0 \chi \vec{E}(t) \tag{1.3}$$

where ϵ_0 is the electric permittivity in vacuum and χ is the susceptibility of the material.
On the other side, for stronger electric fields, the binding potential can no longer be assumed harmonic, since anharmonic effects start to appear. In this case, still assuming that the anharmonic contribution to the harmonic potential is relatively small, we can expand the polarization in power series in the field:

$$\begin{aligned} \vec{P}(t) &= \epsilon_0 \left[\chi^{(1)} \vec{E}(t) + \chi^{(2)} \vec{E}^2(t) + \chi^{(3)} \vec{E}^3(t) + ... \right] \\ &= \vec{P}^{(1)}(t) + \vec{P}^{(2)}(t) + \vec{P}^{(3)}(t) + \dots \end{aligned} \tag{1.4}$$

where $\chi^{(n)}$ is the n-th order susceptibility and $\vec{P}^{(n)}$ is the n-th order contribution to the polarization.
CRS can be understood considering the third order contribution to the polarization $\vec{P}^{(3)}(t)$. The magnitude of the effect depends on the third-order susceptibility

$\chi^{(3)}$. It is possible to estimate the magnitude of the third-order susceptibility by considering that non linear effect arises when the applied electric field becomes comparable with the field that binds the electrons to the nuclei. This atomic field is $E_a \approx 2 \cdot 10^7$ esu (in electrostatic unit), than it is expected that the third-order contribution to polarization gets comparable with the linear polarization $P^{(1)} \approx P^{(3)}$. Under this condition $\chi^{(1)} E_a \approx \chi^{(3)} E_a^3$, such that $\chi^{(3)} \approx 3 \cdot 10^{-}15$, a value which is close to actual value of some materials.

1.3 Classical Description of light-matter interaction in CRS

To better understand the CRS processes, it is necessary to highlight the relationship between the electron displacement and the electric field of the electromagnetic radiation. The light-matter interaction can be described assuming to work in the adiabatic approximation, which states that the nuclei, having a mass which is approximately 2000 times bigger than the electron mass, cannot follow the oscillation of the electric field, while the electron, being lighter, will oscillate and it is possible to associate to them an adiabatic electron potential which depends on the nuclear coordinates. Therefore, the electronic polarizability $\alpha(t)$, which links the electric dipole moment to the driving electric field, will be influenced by the nuclear modes. Under this assumption, the magnitude of the electric dipole moment is (we omit vectorial notation for simplicity) :

$$\mu(t) = \alpha(t) E(t) \tag{1.5}$$

Assuming no nuclear modes the polarizability can be approximated as a constant α_0, but in the presence of nuclear modes we can expand the electronic polarizability in a Taylor series in the nuclear coordinate Q:

$$\alpha(t) = \alpha_0 + \left(\frac{\partial \alpha}{\partial Q}\right) Q(t) + ... \tag{1.6}$$

At this point, the nuclear motion along Q can be assumed to be that of a classical harmonic oscillator:

$$Q(t) = 2Q_0 \cos\left(\omega_\nu(t) + \phi\right) = Q_0 \left[e^{i(\omega_\nu(t)+\phi)} + e^{-i(\omega_\nu(t)+\phi)}\right] \tag{1.7}$$

where Q_0 is the amplitude of the nuclear motion, ω_ν is the vibrational frequency of the nucleus and ϕ is the phase of the nuclear vibrational mode. Writing the incoming field as $E(t) = Ae^{-i\omega_p t} + c.c.$, then the electric dipole moment is:

$$\mu(t) = \alpha_0 A e^{-i\omega_p t} + A \left(\frac{\partial \alpha}{\partial Q}\right)_0 \left\{e^{-i(\omega_p - \omega_\nu)t + i\phi} + e^{-i(\omega_1 + \omega_\nu)t - i\phi}\right\} + c.c. \tag{1.8}$$

The first term on the right hand-side is related to the Rayleigh scattering at the incident frequency. The second and third terms are at frequency $\omega_s = \omega_p - \omega_\nu$ and frequency $\omega_{as} = \omega_p + \omega_\nu$,respectively, and are called Stokes and anti-Stokes contribution. These two last terms have an amplitude which is proportional to the

quantity $\partial\alpha/\partial Q$ which describes how the polarizability varies along the nuclear mode.

1.4 Spontaneous Raman Scattering signal

In Eq.1.8 it has been highlighted that the Stokes and anti-Stokes component are proportional to the amplitude of the emitted electric field at the two shifted frequencies. It is then possible to express the Raman-shifted signal in the framework of the classical model. The following analysis will focus on the Stokes signal, but an analog approach can be followed to derive also the anti-Stokes component. From electrodynamics, it is known that the amplitude of the electric field at frequency ω_s emitted by an oscillating dipole along $\vec{r}$ in scalar form is [7]:

$$E(\omega_s) = \frac{\omega_s^2}{4\pi\epsilon_0 c^2} |\mu(\omega_s)| \frac{e^{ikr}}{r} \sin\theta \tag{1.9}$$

where k is the wave vector of the radiated field, c is the speed of light, θ is the angle relative to the dipole axis, r is the position of the dipole location with respect to the observation point and $|\mu(\omega_s)|$ is the amplitude of the electric dipole moment at frequency ω_s.
The energy flux which is radiated along $\vec{r}$ by the electric dipole is calculated as the time-averaged Poynting flux S and can be written as [7]:

$$S(\omega_s) = \frac{\epsilon_0 c}{2} |E(\omega_s)|^2 \tag{1.10}$$

Integrating it over the unit sphere it is possible to express the intensity of the Stokes signal as:

$$I(\omega_s) = \frac{\omega_s^4}{12\pi\epsilon_0 c^3} Q_0^2 |A|^2 \left|\frac{\partial\alpha}{\partial Q}\right|^2 \tag{1.11}$$

From Eq.1.11 the intensity of the stokes signal scales with the fourth power of the frequency ω_s and it depends on the $\left|\frac{\partial\alpha}{\partial Q}\right|^2$ and with the intensity of the incident beam $I_0 = |A|^2$. The phase ϕ of the Stokes signal depends on the nuclear mode oscillation. At equilibrium, the phase of the signal related to a given electric dipole is completely uncorrelated to that radiated from a second dipole, such that the overall signal is incoherent and the intensity is given by the product between the intensity emitted by a single dipole and the number of scatterers in the sample. Sometimes, it is more convenient to define a Raman cross-section which is an area expressing the Raman scattering efficiency of a molecule. Given a sample whose length is z and with a molecular density N, the intensity of the Stokes signal can be written as:

$$I(\omega_s) = Nz\sigma(\omega_s) I_0 \tag{1.12}$$

Comparing Eq.1.12 with Eq.1.11, it is evident that the Raman scattering cross-section is directly proportional to $\left|\frac{\partial\alpha}{\partial Q}\right|^2$.

1.5 Coherent Raman Scattering

With respect to spontaneous Raman where there is a single incident field impinging onto the sample, in the coherent Raman processes two incident fields induce oscillations in the molecular electron cloud. These oscillations form an effective a force along the vibrational degree of freedom, which drives the nuclear vibrational modes. The nuclear modes will spatially coherent modulate the refractive properties of the material, such that a third field arriving onto the sample will experience this modulation and give rise to the Stokes and the anti-Stokes signal. Assuming that the vibrational mode of the nucleus is that of a damped harmonic oscillator with resonant frequency ω_ν, we can write the electric field of two incoming beams which are called Pump and Stokes as:

$$E_1(t) = A_1(t)e^{-i\omega_1 t} + c.c \tag{1.13}$$

$$E_2(t) = A_2(t)e^{-i\omega_2 t} + c.c \tag{1.14}$$

where ω_1 and ω_2 are the frequency of the pump and that of the Stokes which, by assumption, are far from the vibrational frequency of the oscillator. In this way, the nuclei cannot be driven by the oscillation of the incident fields, while the electrons can follow them. If the intensity of the two fields are large enough, non linear processes can occur such that the electrons start to oscillate at the frequency $\Omega = \omega_1 - \omega_2$. Hence, the two fields will exerts a force onto the nuclear vibrational mode :

$$F(t) = \left(\frac{\partial \alpha}{\partial Q}\right)_0 \left[A_1 A_2^* e^{-i\Omega t} + c.c\right] \tag{1.15}$$

Therefore, the nuclear displacement Q obeys to the following equation of motion:

$$\frac{d^2Q(t)}{dt^2} + 2\gamma\frac{dQ(t)}{dt} + \omega_\nu Q(t) = \frac{F(t)}{m} \tag{1.16}$$

where γ is the damping constant, m is the reduced mass of the nuclear oscillator and ω_ν is the resonance frequency of the harmonic oscillator. Looking for a solution of the form :

$$Q(t) = Q(\Omega)e^{-i\omega t} + c.c. \tag{1.17}$$

The nuclear displacement will oscillate at Ω with an amplitude:

$$Q(\omega_\nu) = \frac{1}{m}\left(\frac{\partial \alpha}{\partial Q}\right)_0 \frac{A_1 A_2^*}{\omega_\nu^2 - \Omega^2 - 2i\Omega\gamma} \tag{1.18}$$

From Eq.1.18 it is evident that the nuclear displacement depends on the amplitude of the Pump and Stokes field and on the term $\left(\frac{\partial \alpha}{\partial Q}\right)_0$ which express the variation of the polarizability with the nuclear position. Moreover, it also depend on the frequency detuning between ω_ν and Ω, indeed, the amplitude of the nuclear motion is large when Ω matches the resonance frequency of the oscillator.

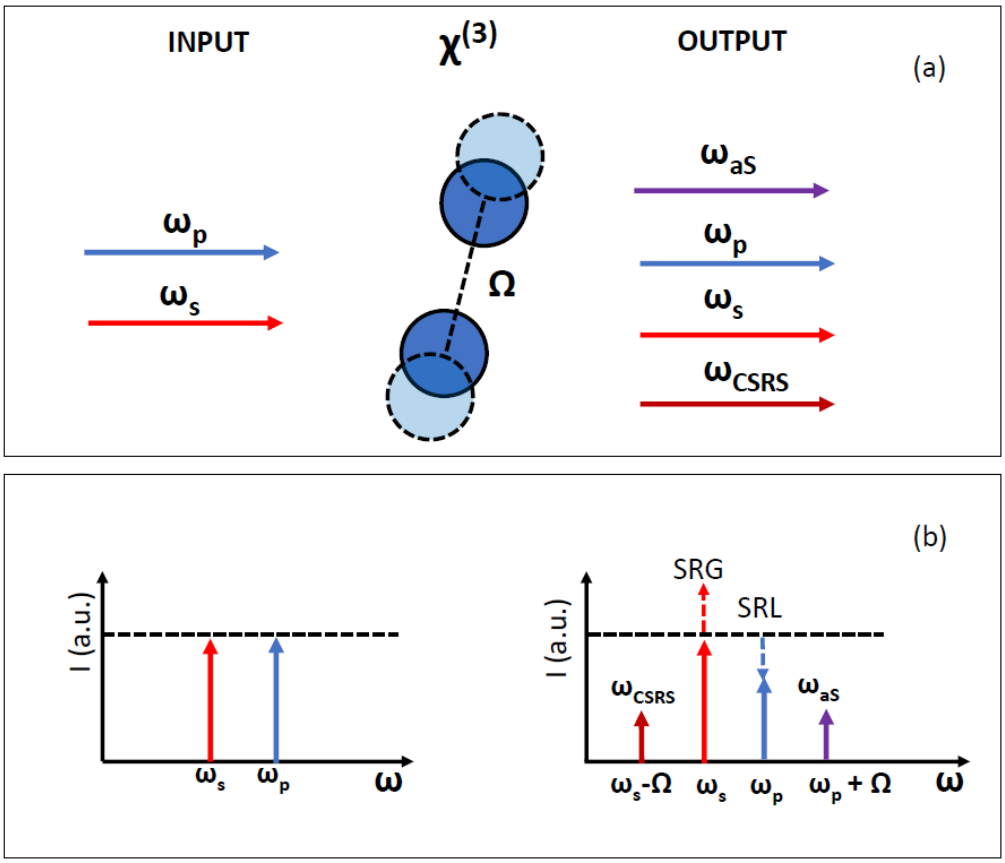

Figure 1.3: Conceptual scheme for the four possible CRS signals generation. (**a**) Two input fields at frequency ω_p (pump) ans ω_s (Stokes) interact with a Raman active $\chi^{(3)}$ medium (the biatomic molecule), generating four different fields at the output (CARS, SRL, SRG, CSRS). (**b**) Conceptual representation in the frequency domain of the non-linear optical processes, where the two input fields interacting with the $\chi^{(3)}$ medium will generate other two side-bands fields that are frequency shifted of an amount Ω correspondent to the vibrational transition of the biatomic molecule.

Using Eq. 1.2, 1.5 and 1.6, the polarization can be expressed as:

$$P(t) = N\left[\alpha_0 + \left(\frac{\partial\alpha}{\partial Q}\right)_0 Q(t)\right]\left\{E_1(t) + E_2(t)\right\} \tag{1.19}$$

Insertig in this expression of the polarization Eq. 1.13, 1.14 and 1.17, the non-linear polarization is written as:

$$P_{NL}^{(3)}(t) = P_{CSRS}e^{-i(\omega_2-\Omega)t} + P_{SRG}e^{-i\omega_2 t} + P_{SRL}e^{-i\omega_1 t} + P_a S e^{-i(\omega_1+\Omega)t} \tag{1.20}$$

where $\omega_{CSRS} = \omega_2 - \Omega$ is the coherent Stokes Raman scattering frequency, $\omega_{SRG} = \omega_2$ is the Stokes frequency and the relative polarization is responsible for stimulated Raman gain , $\omega_{SRL} = \omega_1$ is the pump frequency and the relative polarization is responsible for stimulated Raman gain and $\omega_{aS} = \omega_1 + \Omega$ is the coherent anti-Stokes Raman scattering frequency(see Fig. 1.3). The amplitude

of the polarization of the anti-Stokes signal is :

$$P(\omega_{aS}) = \frac{N}{m}\left(\frac{\partial\alpha}{\partial Q}\right)_0^2 \frac{A_1^2 A_2^*}{\omega_\nu^2 - \Omega^2 - 2i\Omega\gamma} = 6\epsilon_0\chi_{NL}(\Omega)A_1^2A_2^* \tag{1.21}$$

where the non linear susceptibility is defined as:

$$\chi_{NL}(\Omega) = \frac{N}{6\epsilon_0 m}\left(\frac{\partial\alpha}{\partial Q}\right)_0^2 \frac{1}{\omega_\nu^2 - \Omega^2 - 2i\Omega\gamma} \tag{1.22}$$

Similarly for the other frequency component we can write:

$$P(\omega_{CSRS}) = 6\epsilon_0\chi_{NL}^*(\Omega)A_2^2A_1^* \tag{1.23}$$

$$P(\omega_2) = 6\epsilon_0\chi_{NL}^*(\Omega)\left|A_1\right|^2 A_2 \tag{1.24}$$

$$P(\omega_1) = 6\epsilon_0\chi_{NL}(\Omega)\left|A_2\right|^2 A_1 \tag{1.25}$$

The induced polarization in the material produces four signal at four different frequencies, two of them are at the fundamental frequencies of the pump and the Stokes, while the other two are new frequencies which correspond to the Stokes and the anti-Stokes coherent Raman signals.

Energy flow in coherent Raman scattering

To describe the energy flow in Coherent Raman Scattering and understand what are the amplitudes of the different fields after the interaction with the sample, one can adopt a classical model starting from Maxwell's equations and deriving the wave propagation equation in the plane wave approximation. As it is already known, the electric and magnetic field, $\vec{E}$ and $\vec{H}$ in vacuum are influenced by charge density ρ and by the current density $\vec{J}$. Moreover, if the electromagnetic field propagate in a medium, it is useful to define two new fields which are the electric displacement $\vec{D}$ and the magnetic induction $\vec{B}$, which are defined as :

$$\vec{D} = \epsilon_0\vec{E} + \vec{P} \tag{1.26}$$

$$\vec{B} = \mu_0(\vec{H} + \vec{M}) \tag{1.27}$$

where ϵ_0 and μ_0 are the electrical and magnetic permittivity of the vacuum, $\vec{P}$ and $\vec{M}$ are the polarization density and the magnetization density of the medium, defined at the first order as:

$$\vec{P}^{(1)} = \epsilon_0\chi_e^{(1)}\vec{E} \tag{1.28}$$

$$\vec{M}^{(1)} = \chi_m^{(1)}\vec{H} \tag{1.29}$$

where $\chi_e^{(1)}$ and $\chi_m^{(1)}$ are the first order electric and magnetic susceptibility which depend on the material. For our discussion, we are interested in the third-order non linear processes; since the response of the medium to an incoming field is described by the polarization density, in the hypothesis of an isotropic, centro-symmetric and non magnetic medium, it follows that :

$$\vec{P} = \vec{P}^{(1)} + \vec{P}^{(3)} = \epsilon_0 \chi_e^{(1)} \vec{E} + \epsilon_0 \chi_e^{(3)} \vec{E} \cdot \vec{E} \cdot \vec{E} \tag{1.30}$$

By assuming to have a non magnetic medium ($\vec{M} = 0$,$\chi_m = 0$) and that there are no current and charge density sources ($\rho = 0$,$\vec{J} = 0$), we can write down the following Maxwell's equation:

$$\vec{\nabla} \times \vec{E} = -\frac{\partial \vec{B}}{\partial t} \tag{1.31}$$

$$\vec{\nabla} \times \vec{H} = \frac{\partial \vec{D}}{\partial t} \tag{1.32}$$

$$\vec{\nabla} \cdot \vec{B} = 0 \tag{1.33}$$

$$\vec{\nabla} \cdot \vec{D} = 0 \tag{1.34}$$

From which it is possible to derive the following wave equation for a medium with a refractive index n:

$$\vec{\nabla}^2 \vec{E} - \frac{1}{c^2} \frac{\partial^2}{\partial t^2} \vec{E} = \mu_0 \frac{\partial^2}{\partial t^2} \vec{P} \tag{1.35}$$

By substituting in $\vec{P}$ the expression in Eq. 1.30, we can write :

$$\vec{\nabla}^2 \vec{E} - \frac{n^2}{c^2} \frac{\partial^2}{\partial t^2} \vec{E} = \frac{1}{\epsilon_0 c^2} \frac{\partial^2}{\partial t^2} \vec{P}^{(3)} \tag{1.36}$$

This equation can be used in the so called four-wave mixing approach in which we consider three incoming fields which interact with the sample and a fourth field which corresponds to the response of the sample. We can work in the plane wave approximation and derive the expression of the signal emitted by the sample. By assumption, the incident fields are plane waves with constant amplitude and phase in the transverse plane (x,y) which propagate along the z direction. Moreover, without loss of generality, the fields are polarized along the $\hat{x}$ direction. In four-wave mixing, one can write Eq. 1.36 for the three incoming fields $\vec{E_1}$, $\vec{E_2}$, $\vec{E_3}$ and for the signal field $\vec{E_a}$. Considering that the generic expression of the incoming fields is :

$$\vec{E_j}(z,t) = \frac{1}{2} \left(A_j(z) e^{i(k_j z - \omega_j t)} + A_j^*(z) e^{-i(k_j z - \omega_j t)} \right) \hat{\vec{x}} \; for \; j = 1,2,3 \tag{1.37}$$

where ω_j, k_j and A_j are the angular frequency, the wavevector and the amplitude of the incident j-th field. Moreover, it is possible to write a general expression of the induced third-order polarization in the nonlinear Raman-active material as:

$$\vec{P}^{(3)}(z,t) = \frac{1}{8} \epsilon_0 \chi_e^{(3)}(\Omega) A_1(z) A_2^*(z) A_3(z) e^{i[(k_1 - k_2 + k_3)z - \omega_4 t]} \hat{\vec{x}} + c.c \tag{1.38}$$

From Eq. 1.38, it is evident that the induced polarization oscillates at frequency $\omega_4 = \omega_1 - \omega_2 + \omega_3$ and emerges from the medium's boundaries with a forward and backward propagating waves propagating along the z direction with wave vector k_4. For a forward-propagating plane wave, it is possible to look for a solution as:

$$E_4(z,t) = \frac{1}{2}\left(A_4(z)e^{i(k_4 z-\omega_4 t)} + c.c.\right) \tag{1.39}$$

Inserting this ansatz in Eq. 1.36 and adopting the slowly varying envelope approximation (SVEA), which assumes that the variation of the amplitude A_4 of the wave is incrementally small over a distance on the order of the optical wavelength, it is possible to write for the amplitude A_4:

$$\frac{\partial A(z)}{\partial z} = i\frac{\omega_4}{8n_4 c}\chi_e^{(3)}(\Omega)A_1(z)A_2^*(z)A_3(z)e^{i\Delta k z} \tag{1.40}$$

where $\Delta k = k_1 - k_2 + k_3 - k_4$ is the wave vector mismatch along the z axis between the wave vector of the polarization field $k_1 - k_2 + k_3$ and the wave vector of the emitted field k_4. Assuming of working in the parametric approximation, such that the amplitudes of the incident fields remain constant, it is possible to find a solution for a propagation from $z = 0$ to $z = L$:

$$A_4(L) = i\frac{\omega_4}{8n_4 c}\chi_e^{(3)}(\Omega)A_1(z)A_2^*(z)A_3(z)\mathrm{sinc}\left(\frac{\Delta kL}{2}\right)e^{i\Delta kL/2} \tag{1.41}$$

This equation shows the importance the significance of the extent of the wave vector mismatch for the efficient build-up of the coherent radiation field amplitude.. Indeed, when the phase mismatch $\Delta\phi = \Delta kL$ is zero, being $\mathrm{sinc}(0) = 1$, the amplitude of the radiated field will be maximized. Having a null phase mismatch means that the phase of the nonlinear polarization remains the same of the phase of the signal during propagation. Since the medium is dispersive usually the wave vector mismatch is not zero and the effective coherence is mantained only over a coherence length $L_c = 2\pi\ |\Delta k|$. So far, the case of forward-propagating plane wave has been discussed. For the case of backward-propagating wave, following the same approach, it is possible to find a wavevector mismatch which is $\Delta k = 2k_4$, consequently the coherence length is much smaller than the wavelength λ_4 of the radiating field, that is $L_c = \lambda_4/2n_4$ and so it is not possible to appreciate the signal which is propagating in the direction $-z$. This signal can be detected only if the sample has a thickness which is lower that the coherence length L_c.

1.6 Coherent anti-Stokes Raman scattering (CARS)

Coherent anti-Stokes Raman scattering (CARS) is the result of the frequency mixing between one pump-photon at frequency ω_p, one Stokes photon at frequency ω_s and one probe photon at frequency ω_{pr} to generate one anti-Stokes photon at frequency $\omega_{aS} = \omega_p + \omega_p r - \omega_s$. Typically, in CARS the four wave-mixing approach is executed considering the degenerate case where the field 1 and 3 correspond to the pump ($E_1 = E_2 = E_p$) at frequency ω_p and the field 2 corresponds to the Stokes beam ($E_2 = E_s$) at frequency ω_s. The radiating field (E_{as}) oscillates at the anti-Stokes frequency $\omega_{as} = 2\omega_p - \omega_s$ and has a wavevector

$k_{as} = 2k_p - k_s$. Under this assumption it is possible to derive the anti-Stokes field after a propagation of length L in the Raman active medium as :

$$E_{aS}(L) \propto -i\chi_e^{(3)}(\Omega)E_p^2 E_s^* \text{sinc}\left(\frac{\Delta kL}{2}\right) e^{i\Delta kL/2} \tag{1.42}$$

where $\Delta k \equiv k_{aS} + k_s - 2k_p$ is the wave vector mismatch that derives from the energy ($\omega_{aS} = 2\omega_p - \omega_s$) and momentum conservation, and E_p and E_s^* are the pump and the complex conjugate Stokes fields, respectively. The wave vector phase match sets, on the one hand, the maximum interaction length for efficient CARS conversion and, on the other hand, the direction where the CARS field will be emitted (k is a vector). Since when we detect, we measure the intensity, which is proportional to the squared modulus of the field, it is possible to write the intensity of the anti- Stokes signal as:

$$I(\omega_{aS}) \propto |A_{as}(L)|^2 \propto \left|\chi_e^{(3)}(\Omega)\right|^2 I_p^2 I_s L^2 \text{sinc}^2\left(\frac{\Delta kL}{2}\right) \tag{1.43}$$

From Eq. 1.43 one can highlight some important features of CARS signal. First, the CARS signal is proportional to the square amplitude of the nonlinear susceptibility $\chi_e^{(3)}(\Omega) = \chi_e^{(3)}(\omega_{aS}; \omega_p, -\omega_s, \omega_p)$. Since $\chi_e^{(3)}$ is proportional to the density of scattering molecules, the CARS signal depends quadratically on the number of molecules in the interaction volume. The quadratic dependence implies that the CARS signal is particularly strong for media that contain a high concentration of scattering molecules. Under the assumption of tight focusing condition, which is the typical scenario in microscopy experiments using high numerical-aperture objectives, the interaction length becomes small and the phase-matching condition relaxes ($\Delta k \neq 0$), thus we can neglect ΔkL and set it to zero. In this way the CARS intensity will be:

$$I_{aS} \propto |E_{aS}(L)|^2 \propto \left|\chi_e^{(3)}\right|^2 I_p^2 I_s L^2 \tag{1.44}$$

From Eq. 1.44 it is possible to note that the intensity of the anti-Stokes signal has a quadratic dependence on the interaction length, a quadratic dependence on the pump intensity and linear on the Stokes intensity and a quadratic dependence on the third-order non-linear susceptibility.
Notice that, in the case of forward-detected CARS (F-CARS) signals, a small wave vector mismatch is caused by the dispersion of the medium. It will results in a coherence length of the order of 0.8-1 mm, which is quite large for microscopy application, in which the nonlinear interaction length is generally of the order of a micrometer. Consequently, in F-CARS, the dispersion induced phase mismatch introduces no significant effects on the signal. In the case of epi-detected CARS (E-CARS) signals, a significant wave vector mismatch of $|\Delta k| = 2\,|k_{aS}|$ is introduced for the backward propagating wave, which corresponds to coherence length of the order of 0.2-0.3 μm in water. So the phase-mismatch induced backward propagation is only relevant in E-CARS microscopy applications where a nanoscopic object is being studied whose axial dimension, which here determines the nonlinear interaction length, does not exceed the coherence length.

The spectral shape of CARS signal is strongly dependent on the frequency behavior of the third-order non-linear susceptibility, as it is suggested by Eq. 1.44. In particular, two contributions take part to the total $\chi_e^{(3)}$: one resonant contribution $\chi_R^{(3)}$ related to the Raman effect (see eq. 1.22) and one non-resonant contribution $\chi_{NR}^{(3)}$ related the pure electronic response of the material. In general, it is possible to write the overall third-order non-linear susceptibility as:

$$\chi_e^{(3)}(\Omega) = \chi_R^{(3)} + \chi_{NR}^{(3)} = \Re\{\chi_R^{(3)}(\Omega)\} + i\Im\{\chi_R^{(3)}(\Omega)\} + \chi_{NR}^{(3)} \tag{1.45}$$

where:

$$\Re\{\chi_R^{(3)}(\Omega)\} \propto N\frac{\omega_\nu - \Omega}{(\omega_\nu - \Omega)^2 + \gamma^2} \tag{1.46}$$

$$\Im\{\chi_R^{(3)}(\Omega)\} \propto N\frac{\gamma}{(\omega_\nu - \Omega)^2 + \gamma^2} \tag{1.47}$$

$$\chi_{NR}^{(3)} = C \tag{1.48}$$

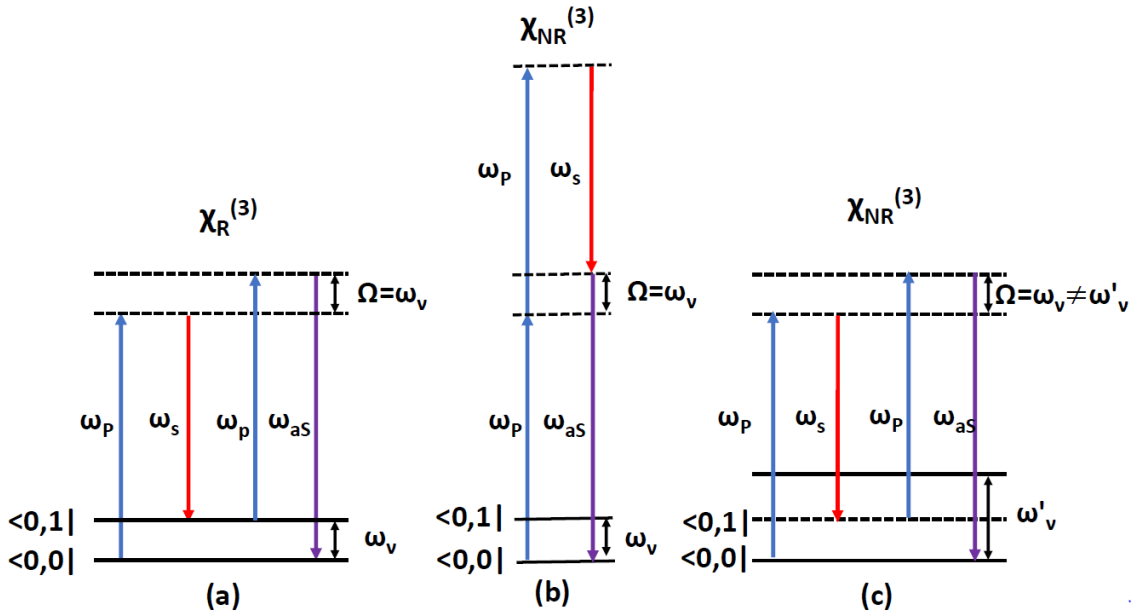

Figure 1.4: Schematic of the possible four-wave mixing light matter interactions, through Jablonski diagrams (solid lines are real level and dashed lines virtual levels), leading to the same anti-Stokes signal at frequency ω_{aS}. The subscript p, s, aS stands for pump, Stokes and anti-Stokes, respectively. **(a)** Resonant CARS signal diagram for target molecule with resonant frequency ω_ν ($\Omega = \omega_p - \omega_s = \omega_\nu$), that leads to $\chi_R^{(3)}$ contribution. **(b)** Non-resonant FWM signal diagram due to the pure electronic response of the target molecule, that leads to $\chi_{NR}^{(3)}$ contribution. **(c)** Non-resonant FWM signal diagram due to the pure electronic response of a non-target molecule with resonance frequency $\omega'_\nu(\Omega = \omega_p - \omega_s \neq \omega'_\nu)$, that leads to $\chi_{NR}^{(3)}$ contribution.

$\chi_R^{(3)}$ is a complex quantity and has a spectral dependence that follows, near the resonances, the typical resonance shape, for the imaginary part, and a dispersive-like shape, for the real part (see Fig.1.5.a). The imaginary part is the resonance

Raman response related to the nuclear vibrational motions, it has the typical Lorentzian line-shape of spontaneous Raman spectra (in proximity of the resonance frequency). The real part, on the other hand, is related to the electronic non-resonant contribution $\chi^{(3)}_{NR}$, which is tipically referred to as non-resonant background (NRB) and which arises from the fact that four-wave mixing processes, in addition to the resonant CARS process, compete simultaneously to generate a signal at the anti-Stokes frequency ω_{aS}. While CARS process is mediated by Raman vibrational resonances, the other processes, originating from the four-wave-mixing , can exchange energy via the third-order non linear susceptibility of the molecules even in absence of real Raman vibrational transitions (since the energy and momentum conservation is preserved). For example, in a biological samples, typically, there are not only the target molecules but also others present, like the solvents molecules which usually do not share the same vibrational resonances as the studied ones. Therefore, these non-target molecules cannot contribute to the resonant term of the susceptibility but they can give electronic non-resonant contributions, by interacting with the incoming fields, at the same CARS frequency ω_{aS} through the $\chi^{(3)}_{NR}$, as it is depicted in Fig. 1.4 (c). Moreover even the target molecules take part to the non-resonant contribution of the signal at the anti-Stokes frequency ω_{aS} (Fig. 1.4(b)), along with the resonant contribution (Fig. 1.4(a)). Since the NRB resulting from the $\chi^{(3)}_{NR}$ contribution is instantaneous (only virtual level are involved in the interaction) and frequency not specific (no real electronic/vibrational transitions are involved), it has a flat response in the spectral domain. Both the signals coming $\chi^{(3)}_{R}$ and $\chi^{(3)}_{NR}$ are coherent and at the same frequency ω_{aS}.

From Eq. 1.44, it is evident that the CARS signal intensity is proportional to $\left|\chi^{(3)}_{e}\right|^2$, so it is possible to rewrite the intensity as :

$$\begin{aligned} I_{aS} \propto \left|\chi^{(3)}_{e}\right|^2 &= \left|\Re\{\chi^{(3)}_{R}(\Omega)\} + i\Im\{\chi^{(3)}_{R}(\Omega)\} + \chi^{(3)}_{NR}\right|^2 = \\ &= \left|\Re\{\chi^{(3)}_{R}(\Omega)\}\right|^2 + \left|\Im\{\chi^{(3)}_{R}(\Omega)\}\right|^2 + \left|\{\chi^{(3)}_{NR}(\Omega)\}\right|^2 + 2\left|\Re\{\chi^{(3)}_{R}(\Omega)\}\right| \cdot \left|\chi^{(3)}_{NR}\right| \end{aligned} \tag{1.49}$$

Eq. 1.49 states that the frequency independent contribution of the NRB does not merely add a constant background to the resonant CARS signal, that, if it was, it would be easy to remove it. Instead, by looking at the last term of the equation, there is an interference term that causes distortions of the CARS resonant signal. Fig. 1.5 reports the CARS signal considering each single contribution given by the real and imaginary part of the resonant electric susceptibility (Fig.1.5.a) and than considering the overall contribution for different value of the NRB ($\chi^{(3)}_{NR}$) with respect to the resonant component ($\chi^{(3)}_{R}$) in Fig.1.5.b. We note that, in presence of a non-resonant contribution the overall signal does not have the typical symmetric shape of a Lorentzian curve, but it is asymmetric with a red-shift of the peak and the presence of a offset. Moreover, as the NRB increases the amount of distortion relative to the overall signal gets larger as well, making harder the recognition of diluted species present in a medium.

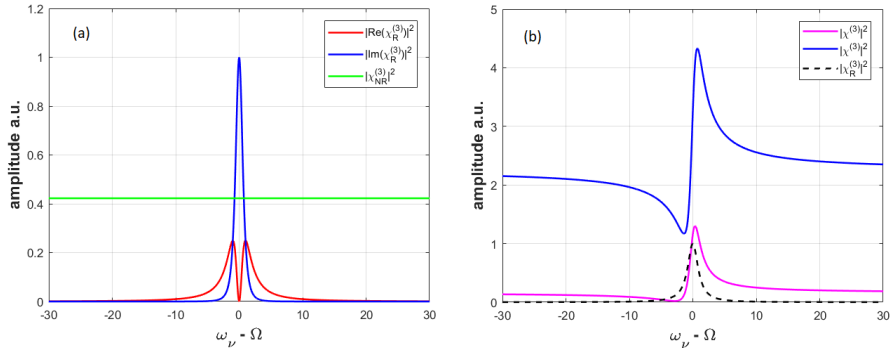

Figure 1.5: Spectral shape of the CARS signal and of the different $\chi^{(3)}$ contributions from eq. 1.49. **(a)** Spectral shape of $\left|\Im\{\chi_R^{(3)}(\Omega)\}\right|^2$ (blue curve), of $\left|\Re\{\chi_R^{(3)}(\Omega)\}\right|^2$ (red curve) and $\left|\{\chi_{NR}^{(3)}(\Omega)\}\right|^2$ (green line). **(b)** Cars overall signal $\propto \left|\chi_e^{(3)}\right|^2$ considering different strength of the NRB: $\left|\chi_{NR}^{(3)}/\chi_R^{(3)}\right| = 0$ (black dashed curve), $\left|\chi_{NR}^{(3)}/\chi_R^{(3)}\right| = 0.4$ (purple curve) and $\left|\chi_{NR}^{(3)}/\chi_R^{(3)}\right| = 1.5$ (blue curve).

In the case of dilute target molecules $\left|\chi_R^{(3)}(\Omega)\right|^2 << \left|\chi_{NR}^{(3)}(\Omega)\right|^2$, it is possible to simplify Eq. 1.44 to $I_{aS} \propto \left|\{\chi_{NR}^{(3)}(\Omega)\}\right|^2 + 2\left|\Re\{\chi_R^{(3)}(\Omega)\}\right| \cdot \left|\chi_{NR}^{(3)}\right|$ and the consequent signal to noise ratio (SNR) in CARS detection becomes [24]:

$$SNR_{CARS} \propto \frac{2\left|\Re\{\chi_R^{(3)}(\Omega)\}\right| \cdot \left|\chi_{NR}^{(3)}\right| \cdot I_p^2 \cdot I_s}{\alpha\left|\chi_{NR}^{(3)}\right|^2 \cdot I_p^2 \cdot I_s + \left|\chi_{NR}^{(3)}\right| \cdot I_p \cdot \sqrt{I_s}} \xrightarrow[\alpha\to 0]{} 2\left|\Re\{\chi_R^{(3)}(\Omega)\}\right| \cdot \left|\chi_{NR}^{(3)}\right| \cdot I_p^2 \cdot \sqrt{I_s} \tag{1.50}$$

where $\alpha\left|\chi_{NR}^{(3)}\right|^2 \cdot I_p^2 \cdot I_s$ is the low-frequency intensity noise carried by the NRB (due to 1/f noise of the excitation laser) and $\left|\chi_{NR}^{(3)}\right| \cdot I_p \cdot \sqrt{I_s}$ is the shot noise related to the NRB. In the case of shot noise limited measurements, which means to consider small value of α, the resulting SNR is the one reported in Eq. 1.50.

1.7 Stimulated Raman scattering (SRS)

Stimulated Raman scattering is another process which belongs to the class of coherent Raman scattering processes. With respect to CARS that probes vibrational coherences in the Raman active medium, SRS monitors directly the vibrational population states, through the same third-order non-linear susceptibility. SRS utilizes the same excitation scheme of CARS, where two narrowband input fields interact with the Raman active sample and when the frequency detuning Ω between them ($\omega_p - \omega_s = \Omega$) matches a Raman active molecular vibration at frequency ω_ν an excited vibrational population with energy $\hbar\omega_\nu$ is created in the sample through the third-order non-linear susceptibility $\chi_e^{(3)}$. In this way,

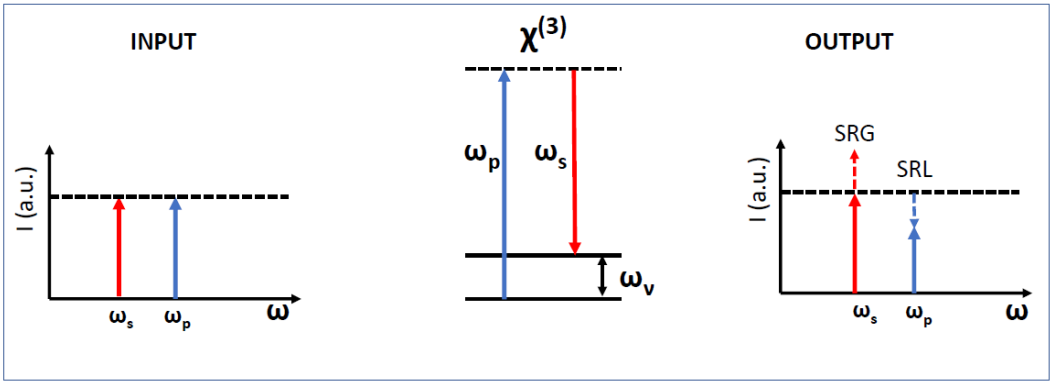

Figure 1.6: Schematic of the SRS light-matter interaction (where SRG stands for stimulated Raman gain ans SRL for stimulated Raman loss). The subscribts p ans s stands for pump and Stokes, respectively. Energy level diagram in the intensity representation through Jablonski diagrams (dashed lines are virtual levels and solid lines real levels)

together with a nonlinear polarization at frequency ω_{aS} (CARS), the formation of third order nonlinear polarization at the frequencies of the input fields takes place. The optical heterodyne phenomenon between the input fields and the generated nonlinear fields, irradiated by the nonlinear polarizations, manifests itself as the stimulated Raman gain (SRG) of the Stokes field and the stimulated Raman loss (SRL) of the pump field (Fig. 1.1), which carry the same Raman information. Quantum mechanically, the picture of the process is the following: the interaction with the Raman active material leads to the absorption of a pump photons at frequency ω_p (that is annihilated) and the emission of a Stokes photon at frequency ω_s (that is created), while the energy difference between the two photons $\hbar(\omega_p - \omega_s)$ is absorbed by the material for energy conservation. Since energy is deposited in the material after the interaction, SRS belongs to the so called nonlinear dissipation processes where, after the non-linear interaction, an exchange of energy between the laser fields and the medium takes place. CARS, on the other hand, is a parametric generation process because only the fields involved in the non-linear interaction exchange energy, while the medium, at the end of the interaction, remains in the ground-state.

In Fig. 1.1 is shown the Jablonski diagram of the SRS process which is similar to that of the SR process, the only difference is the occupation number of the relative photon modes. Indeed, in spontaneous Raman scattering, the pump mode at frequency ω_p is occupied with a high number of photons , $n_p >> 1$, while the Stokes mode at frequency ω_s is initially empty, $n_s = 0$. The occupation number, after the Raman interaction, become $n_p - 1$ for the pump ans $n_s + 1$ for the Stokes, where the Stokes photon is generated from vacuum field. This treatment is also valid for SRS, with the only difference that the initial occupation number for the Stokes mode is high, $n_s >> 1$. In this way it is possible to define an amplification factor, associated to the stimulating effect of SRS, as the ratio between the photon

generation in SRS and spontaneous Raman [23]:

$$\frac{W_{SRS}}{W_{spont}} = \frac{\sigma_{Raman} n_p (n_s + 1)}{\sigma_{Raman} n_p} = (n_s + 1) \tag{1.51}$$

where σ_{Raman} is the Raman scattering cross-section. Since for SRS both pump and Stokes are present simultaneously in the sample, the net increase in the emission rate is proportional to the number of photons in the Stokes mode (typically $n_s > 10^7$). This means that the information on Raman transitions can be retrieved much faster in SRS than in SR scattering by many orders of magnitude. The expression for the amplitude of SRG and SRL can be obtained using a four-wave mixing approach. Within the plane wave approximation, we can still consider the degenerate case where the sample interact with one pump beam at frequency ω_p and one stokes beam at frequency ω_s, which will propagate in the forward direction along the z-axis. In case of stimulated Raman gain (SRG) process, considering the detection of the Stokes field at frequency ω_s and defining the third-order nonlinear susceptibility $\chi_e^{(3)}$, it is possible to derive the expression of the amplitude of the forward-propagating stimulated Raman signal for which the wave vector mismatch is $\Delta k = -k_p + k_s + k_p - k_s = 0$ [7]:

$$A_s^{stim}(L) = i \frac{\omega_2}{8 n_2 c} \left\{ \chi_e^{(3)}(\Omega) \right\}^* A_p^* A_s A_p L \tag{1.52}$$

Given that, the stimulated field has an angular frequency similar to the frequency of the Stokes field, hence, the two contributions will interfere at the detector. Hence, the forward-detected SRG itensity of the radiation at frequency ω_s is:

$$I(\omega_s) \propto \left| A_s(L) + A_s^{stim}(L) \right|^2 = I_s + \left| \chi_e^{(3)} \right|^2 I_p^2 I_s L^2 + 2 \Im \chi_e^{(3)}(\Omega) I_p I_s L \tag{1.53}$$

The first term on the right hand side is the intensity of the Stokes beam, which we assumed remains virtually unattenuated during the non linear process. The second term is the intrinsic SRS signal, which shows a similar dependence on the incident beam intensities, the $\chi_e^{(3)}$ of the material and the propagation length L as the CARS signal. Indeed, the intrinsic SRG signal is of similar magnitude of the CARS signal. The last term is the interference between the incident Stokes field and the stimulated Raman field at the detector. Note that if $\chi_e^{(3)}$ is purely real, the interference term disappears, however close to resonance $\Im\{\chi_e^{(3)}\} \neq 0$, the interference term is non-vanishing. Using modulation techniques, this interference term can be electronically isolated from the remaining terms in Eq. 1.53. Under the assumption that the amplitude of the incident Stokes laser field is much higher than that of the stimulated Raman field amplitude ($A_s >> A_s^{stim}$), the quantity which is physically detected in an SRG experiment is the change in intensity of the Stokes beam:

$$\Delta I(\omega_s) \propto 2 \Im\{\chi_e^{(3)}(\Omega)\} I_p I_s L \tag{1.54}$$

From Eq. 1.54, we see that the plane wave model predicts that the SRG signal is proportional to the length L at the interaction volume, as well as, it has a linear dependence on the pump and on the Stokes beams (I_p and I_s). It is important

to point out that it depends on the imaginary part of the third-order nonlinear susceptibility $\chi_e^{(3)}$. At the vibrational frequency $\Omega = \omega_\nu$, it has positive value, hence, it results in a gain of the intensity of the Stokes field. It implies that the SRG signal results from the constructive interference between the incident Stokes field and the radiated field at ω_s[1]. The analogous equation describing the forward-detected stimulated Raman loss (SRL) signal is obtained by exchanging the subscript s and p and by inverting the sign of the imaginary part of the third-order nonlinear susceptibility. The quantity physically detected in an SRL process is then:

$$\Delta I(\omega_1) \propto -2\Im\{\chi_e^{(3)}(\Omega)\} I_p I_s L \tag{1.55}$$

For the same consideration we have done for the SRG case, the SRL signal represents a loss in intensity in the ω_p channel and it derives from a destructive interference between the pump field and the induced field at ω_p.

For completeness, it is important to underline that so far we have discussed the case of forward-detected SRS (F-STS) signal. While the forward-propagating stimulated Raman field is always phase-matched with the incident field, in the epi-detected SRS (E-SRS) there is a non zero wave vector phase match. Indeed it results in $|\Delta k| = 2|k_s|$ for SRG signal and $|\Delta k| = 2|k_p|$ for SRL signal. Consequently, the backward-propagation-induced phase mismatch will determine an effective coherence length L_c which is very small in water (0.3 or 0.4 μm for light beams in the NIR) and so it is only relavant in microscopy applications where a nanoscopic object is being studied whose geometry does not exceed the coherence length.
The consequent signal-to-noise ratio (SNR) in SRS is expressed as [24]:

$$SNR_{SRG} = \frac{2\Im\chi_e^{(3)}(\Omega) I_p I_s}{\alpha I_s + \sqrt{I_s}} \xrightarrow[\alpha \to 0]{} 2\Im\chi_e^{(3)}(\Omega) I_p \sqrt{I_s} \tag{1.56}$$

$$SNR_{SRL} = \frac{2\Im\chi_e^{(3)}(\Omega) I_p I_s}{\alpha I_p + \sqrt{I_p}} \xrightarrow[\alpha \to 0]{} 2\Im\chi_e^{(3)}(\Omega) I_s \sqrt{I_p} \tag{1.57}$$

where αI_s (αI_p) is the laser intensity noise of the Stokes (pump) beam and $\sqrt{I_s}$ ($\sqrt{I_p}$) is the shot noise of the Stokes (pump) beam intensity. By applying modulation-transfer geometry coupled with high-frequency modulation and detection with lock-in amplifiers, it is possible to remove the low frequency component of the laser intensity noise and obtain almost shot-noise limited detection SRS measurements approaching 10^{-7} sensitivity in 1 s (see Appendix A).

1.8 SRS vs CARS

SRS and CARS are two techniques that allows us to probe the vibrational modes of the sample, they both are based on the illumination of the sample with two

[1]SRG is tipically defined as: $SRG = \frac{\Delta I_{SRG}(\omega_s)}{I_S}$. SRL in the same way is defined as: $SRL = \frac{\Delta I_{SRL}(\omega_p)}{I_p}$.

beams (pump and Stokes) at ω_p and ω_s, such that they probe the same vibrational state of the speciman, that is $\Omega = \omega_p - \omega_s$. The main difference between the two is how the information is translated in terms of the amplitude and phase of the emitted electric fields. As we have seen in previous sections (1.6 and 1.7), in CARS the information comes from the field oscillating at the anti-Stokes frequency, instead for SRS the information is embedded on the losses of the pump (SRL) or on the gain of the Stokes signal (SRG). From an experimental point of view, it implies the use of two different approaches to extract from the measured signal the given Raman vibrational information.
The most relevant SRS advantages over CARS are:

- SRS signal is free from NRB and directly proportional to the Raman cross-section σ_{Raman}, thus one can directly compare the SRG/SRL signal with the data already known in litterature. On the other hand, CARS is affected by NRB and it is difficult to do a direct comparison of the spectra.

- SRS signal scales linearly with the concentration of molecule inside the sample, thus one can retrieve also a quantitative information about the target molecules, without any problem about the fact that they are present in high or low concentration. In CARS there is a quadratic dependance on the concentration of target molecules, it means that in case of low concentration of the target molecules it is difficult to distinguish the signal from the NRB.

- Two-photon fluorescence overlaps the spectral region of CARS signal, limiting its interpretation. While SRS, being at lower frequency, is not distorted by this process.

- While SRS is automatically phase-matched, therefore a well-defined point-spread function can be used to perform image deconvolution, CARS signals depends on phase-matching condition fulfillment and the quadratic dependence on the concentration on molecule makes the applicability of deconvolution methods very hard.

- SRS detection sensitivity can reach shot-noise limit, by working at high modulation frequency and using lock-in detection system which removes laser fluctuations. In CARS, it is very hard to reach such a sensitivity limit, because of the presence of NRB.

CARS has some advantages with respect to SRS:

- CARS signal is easier to be detected with respect to SRS since it is nearly a background-free process, since it is spectrally separated by the two input fields. Instead, in SRS you must detect a small variation on the number of photons on a large background (pump and Stokes) and so sophisticated techniques are needed to detect them.

- CARS can straightforwardly implemented in the broadband modality, enabling the detection of more chemical species at once. In SRS, the broadband modality requires a particular technological design to detect the full vibrational spectrum of the speciman.

Coherent anti-Stokes Raman Scattering	**Stimulated Raman Scattering**
Parametric generation process	Energy transfer process
Existence of NRB	Absence of NRB
Distorted complex spectrum	Identical spectrum to spontaneous Raman
Limited by laser intensity noise	Shot-noise limited sensitivity
Quadratic concentration dependence	Linear concentration dependence
Non-existence of the point-spread function	Existence of the point spread function
Presence of spatial coherence artifacts	Absence of spatial coherence artifacts
Contamination by two-photon fluorescence	Not affected by background fluorescence

Table 1.1: Comparison between CARS and SRS

Main characteristics of the two techniques are reported in Table 1.1.

1.9 Main implementantions of CRS microscopy

CRS implementations can be distinguished in "single-frequency" CRS and Broadband CRS [11]. Single-frequency CRS is characterised by narrowband pump and Stokes pulses whose duration is of the order of few picoseconds and whose frequency are properly chosen in order to match a proper vibrational transition of the specimen. To implement single-frequency CRS is necessary to provide that at least one of the two beam should be tunable to probe the different vibrational modes of the sample. In terms of wavelength, it is better to work with pulses in the NIR, from 700 to 1500 nm in order to minimize photodamage and increase the penetration depth into the tissue. Moreover, optical power higher than 10-100 mW are needed to clearly measure the CARS/SRS signal.
The single-frequency regime has been successfully employed to track the presence of a molecular species with a specific and rather isolated Raman response,but it does not allow one to distinguish components within an heterogeneous system such as cells or tissues.
Broadband CRS overcomes this limitation providing the full vibrational spectrum of the sample, as it is done in SR, but at the same time it has the high imaging acquisition speed proper of the CRS techniques. It is possible to distinguish two different categories of broadband CRS:

- hyperspectral CRS, which makes use of a single frequency CARS/SRS configuration with narrowband pump and Stokes pulses, whose frequency detuning is rapidly scanned to acquire the full CARS/SRS spectrum;
- multiplex CRS, in which at least one pulse between pump and Stokes is broadband and the CARS/SRS spectrum is recorder either in the frequency domain by a multichannel detector or in the time domain by using a Fourier transform approach.

In the following main implementations for broadband CARS and SRS are discussed, highlighting the main advantages and possible developments of the techniques.

1.9.1 Hyperspectral CARS

In Hyperspectral CARS, a fixed narrowband pump and a tunable narrowband Stokes simultaneously excite a sample and the generated CARS spectrum is acquired by tuning the Stokes beam and so changing the frequency detuning. A method to rapidly change the frequency detuning is the spectral focusing (SF) technique, in which broadband temporally chirped femtosecond pump and Stokes pulses are used to excite the sample (see Fig.1.7). Indeed, temporally chirped pulses have an instantaneous frequency which varies with a quadratic dependence on time within the temporal envelope of the pulse. Writing the electric field of the chirped pulse with a Gaussian temporal profile as:

$$E(t) = E_0 e^{\left[-\left(\frac{t^2}{2\tau_p^2} + i\alpha t^2\right)\right]} \tag{1.58}$$

where α is the so-called chirp parameter and considering two femtosecond pulses whose carrier frequencies are ω_p and ω_s, which are both equally chirped with the same parameter α, it turns out that the instantanous frequency detuning (IFD) between them is:

$$IFD(t) = \omega_p - \omega_s + 2\alpha\Delta t \tag{1.59}$$

Therefore, by scanning the delay Δt between the two pulses, while maintaining their temporal overlap, it is possible to select and probe a different vibrational mode of the sample.

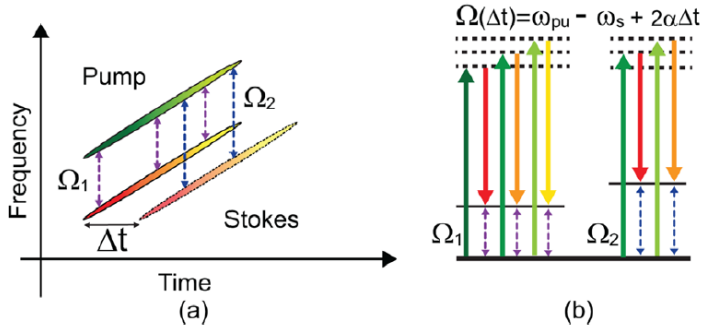

Figure 1.7: a) Sketch of spectral focusing, showinf the time-dependent frequencies of pump and Stokes pulses; b) level excitation scheme. From [11]

1.9.2 Multiplex CARS

In Multiplex CARS, a narrowband pump with duration of few picoseconds and a broadband Stokes with duration of few hundreds of femtoseconds are used to detect the CARS signal by means of a spectrometer. The early studies on this new technique were reported by Müller and Schins [25] and by Cheng et al. [26], CARS signal was limited only to $\approx 200\text{cm}^{-1}$ in the C-H stretching region, with acquisition time of fraction of a second. An upgraded multiplex CARS system with thousands of cm^{-1} spectral coverage was reported by Kee and Cicerone [27]

and by Kano and Hamaguchi [28] [29], in which the pump beam is bandpass filtered in a way such that it becomes narrowband, while the Stokes one undergoes spectral broadening in a nonlinear fiber or in a photonic crystal fiber (PCF).
In multiplex CARS pump and Stokes are collinearly combined and focused on the sample and the CARS signal, after short-pass filtering, is detected via a spectrometer combined with a CCD. The response signal coming from the interaction of the two laser pulses with the sample is mixed with the NRB, which distorts the lineshapes with respect to those measured in SR. This distortion is particularly relevant in the fingerprint region, where the resonant contribution is weak.

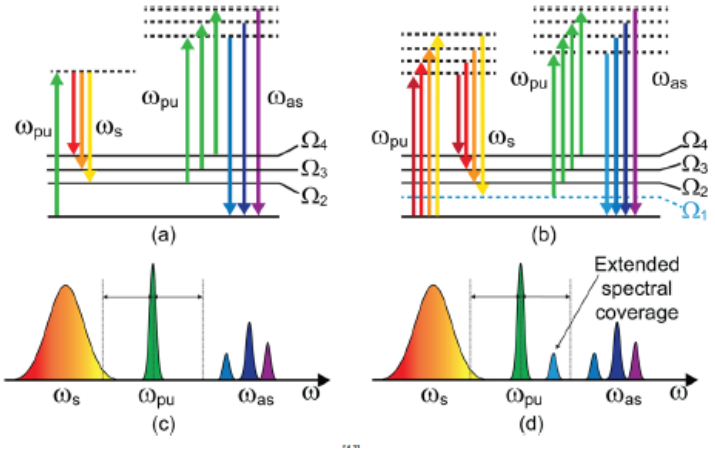

Figure 1.8: Different Cars excitation mechanism. a,c) Two-color mechanism. b,d) Three-color mechanism (ISRS). From [11]

There are two different mechanism which have been implemented By Cicerone et al. to detect signals that are too weak in the critical fingerprint region, these mechanism are called the two-color and the three-color processes. In the two-color process (Fig.1.8.a/c), the narrowband pulse acts as pump and the broadband one as Stokes, enabling one to access a frequency range of thousands of cm^{-1}. In the three-color mechanism (Fig.1.8.b/d), the broadband pulse acts as both pump and Stokes, generating the vibrational coherence by the so-called impulsive stimulated Raman scattering (ISRS) mechanism. ISRS, is a time-domain, single-pulse version of SRS, in which the different frequency components of a single broadband pulse simultaneously excite virtual levels and stimulate the emission down to vibrational levels of the ground state. The ISRS process creates a vibrational coherence in all modes with frequencies falling within the excitation laser bandwidth, provided that the pulse has a temporal duration close to the TL value, so that all frequencies interact nearly simultaneously with the sample. This vibrational coherence is then read out by a further interaction with the narrowband probe pulse, which generates the CARS signal [11].

An elegant approach to effectively remove the NRB is the so-called Time-Resolved CARS. It uses the three color configuration (Fig. 1.9 (a))in which the Stokes beam (ω_s) and the pump beam (ω_{pu}) are temporally synchronized broadband pulses and the probe beam (ω_{pr}) is delayed with respect to the other beam of a time Δt.

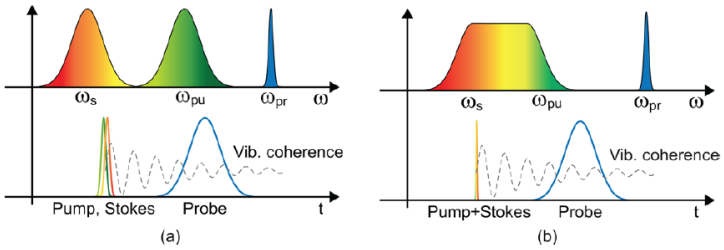

Figure 1.9: TR-CARS pulse sequence in the three-color configuration (a) and in the two.color configuration (b) with the vibrational coherence generated by ISRS.. From [11]

In this way, the resonant non linear susceptibility $\chi_R^{(3)}$, which corresponds to the vibrational coherence generated by the pump and Stokes pulses and persists for few picoseconds, is sampled by the probe pulse. On the other hand the NRB, which is generated by the four-wave mixing process $\omega_{aS} = \omega_{pu} - \omega_s + \omega_{pr}$ mediated by the nonresonant nonlinear susceptibility $\chi_{NR}^{(3)}$, is completely suppressed since it would require temporal overlap of pump, Stokes and probe pulses. The drawback of this technique is that the probe signal interacts with a vibrational coherence that has decayed with a dephasing time $t_{2\nu}$, leading to a reduction of the useful CARS signal by $e^{-2\Delta t/T_{2\nu}}$.

Another alternative solution to suppress the NRB is to use the so-called Fourier Transform approach (FT-CARS). This technique is a time-domain technique which is performed using two time delayed ultrashort pulses (the pump and the probe) with duration shorter than the period of the higher vibrational frequency of interest. The pump pulse excites a vibrational coherence in the sample by ISRS, thus modulating in time the refractive index. The probe pulse will be affected by the time-varying refractive index and gets periodically blue- and red-shifted, thus generating both Stokes and anti-Stokes components. The anti-Stokes component are filtered and its energy is recorded in function of the delay between the pump and the probe. By Fourier transforming it, once get the CARS spectrum. This techniques has the capability of suppressing the NRB, by cancelling out the contribution at the zero delay and it has a good spectral resolution which can be increase by extending the time scanning. Nevertheless, it has some drawbacks, indeed, it can access only the fingerprint region, the high peak power of the ultrashort pulses can lead to photodamage of the samples and time-scanning can slow-down the measurement process.

1.9.3 Hyperspectral SRS

So far we have discussed the different techniques to retrieve the CARS spectrum while using a broadband approach. As regards the broadband SRS techniques it is possible to distinguish also in this case the Hyperspectral and the Multiplex SRS. First SRS measures were acquired while working at single freqeuncy using a picosecond OPOs [30], the first attempts to enhance the chemical speci-

ficity through a parallel or sequential acquisition of several vibration modes were based on the tunability of the OPO themselves. However, since the OPOs has intrinsically a limited tuning speed, the acquisition of SRS images is time consuming [31] [32]. A possible solution to this problem, is the so called spectrally tailored excitation SRS (STE-SRS) [33], which relays in highly specific imaging of a chemical species in the presence of other interfering species, based on a tailored multiplex excitation of its vibractional spectrum. STE-SRS uses a broadband pump and a narrowband Stokes and measures the SRG of the Stokes with a single detector. The spectrum of the pump pulse is shaped with a SLM (spatial light modulator) in such way that it predominantly excites the vibrational resonances of the target species; to suppress the contribution from interfering species, a second tailored pump spectrum is also prepared which targets the resonance of those species. The two tailored pump spectra are then rapidly alternated and the difference between the two SRS spectra is measured, thus effectively suppressing the contribution of the interfering species (see Fig. 1.10).

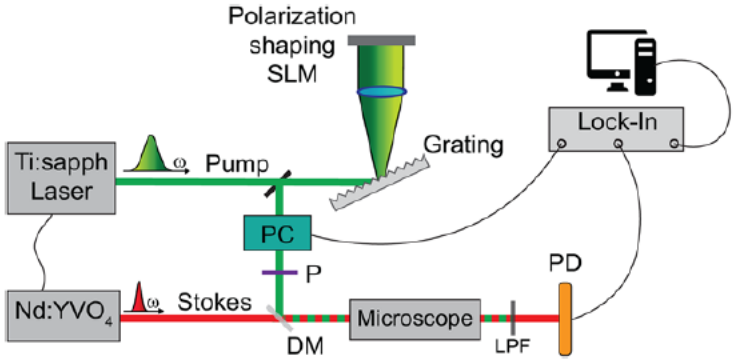

Figure 1.10: STE-SRS setup. DM, dichroic mirror; LPF, long pass filter; P, polarizer; PC, Pockels cell; PD, photo detector; SLM, spatial light modulator. From [11]

The imaging speed af a hyperspectral SRS microscope has been further increased by using an approach based on a very low noise detection chain and on the possibility to scan the frequency detuning between pump and Stokes beams with a millisecond time response (Ozeki et al.) [34]. In recent years a number of hyperspectral SRS setups have been developed based on the SF approach, where the scanning speed has been increased to a point to be able to interrogate each pixel at variable frequency detuning, tipically within $30 - 60\ \mu s$. The first attempts in these direction were based on motorized translation stage, which is a time-sonsuming procedure that limits the overall acquisition speed [36]. Recently, these limitations have been overcomed by using rapid scanning optical delay lines whose designs have been borrowed from optical coherence tomography [37].

1.9.4 Multiplex SRS

In multiplex SRS, the principle scheme is similar to that shown in Fig.1.11. A laser system produces a narrowband pump and a broadband Stokes which are

synchronized, collinearly combined and sent to the sample (into the microscope). The pump pulse, after the sample, is removed with a short-pass wavelength filter, while the broadband Stokes is sent to a multichannel detector, which can e either digital (spectrograph + CCD) or analog (diffraction grating+ photodiode array+ multichannel lock-in amplifier). Each photodiode array, like in a commercial spectrometer, record the intensity of a different spectral portion of the incoming pulse and thus it is possible to reconstruct the broadband pulse spectrum. Then if a modulator, which could be as in our setup an acousto-optic modulator, is placed on the pump beam path, one can calculate the SRG signal as the difference between the Stokes signal in the pump ON and pump OFF states via a lock-in amplifier. In order to measure this signal is therefore necessary that each photodiode is connected to a lock- in amplifier, hence, a multi-channel lock-in amplifier is required to perform the measurement. This approach for multiplex SRS has three main drawbacks:

- the spectral resolution of the system is limited by the number of photodetectors that are possible to integrate in the photodiode array and by the grating properties;
- the complexity of the experimental setup in terms of allignments of the beam into the photodiode array;
- the cost of a multi-channel lock-in amplifier is very high.

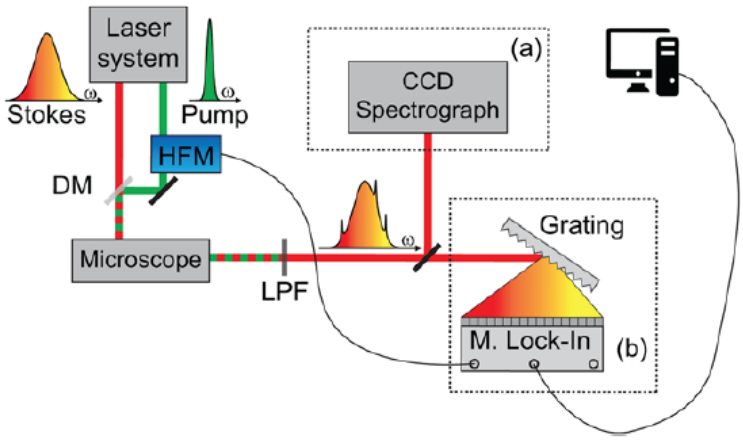

Figure 1.11: Principle of multiplex SRS detection: a) using a spectrometer; b) using a multichannel lock-in amplifier. From [11]

An alternative approach, which overcome these limitations, for high-speed single shot spectra detection is to use the *photonic time stretch* (PTS) approach. The PTS approach which is also known as dispersive FT spectroscopy, is a powerfull technique for single-detector measurement of ultrashort pulse spectra at high repetition rates. It consists in temporally stretching the pulse to be measured, tipically by a long optical fiber, to a duration of a few nanoseconds, so that it can

be accurately sampled by a high-frequency analog-to-digital converter (ADC). In fact, optical fibers are dispersive materials, which means that different optical wavelengths travel at different velocities inside the material since its refractive index is strongly wavelength dependent ($n = n(\lambda)$) (for more details see 3.2). Without time stretching, single shot time profiles would be varying too fast to be correctly reconstructed by ADCs. By calibrating the dispersion introduced by the optical fiber, each point of the sampled temporal profile can be associated to a specific wavelength, thus allowing one to perform the measurement of single-shot spectra at repetition rates up to tens of megahertz. Recently Saltarelli et al. [38] and Dobner et al. [39] applied the PTS approach to the detection of broadband SRS spectra. The experimental setup consists of a narrowband pump and a broadband Stokes which are combined and sent in a collinear configuration towards the sample, the pump is modulated at high frequency and the Stokes spectra after the sample are detected on a single-shot by the PTS technique, retrieving the SRG spectra by digital demodulation with a high-speed ADC card instead of a lock-in amplifier.

Another approach for broadband SRS is based on FT detection of the SRG/SRL spectrum and is referred to as *Fourier Transform-SRS* (FT-SRS). As in FT-CARS is used a single photodetector and thus a single-channel lonk-in amplifier, however here the FT approach is used to detect the Stokes spectrum rather than the Raman spectrum, thus calling for much higher accuracy of the interferometer due to the one order of magnitude higher sampled frequencies. It relies on the time-domain measurement of spectra. It employs a narrowband pump and a broadband Stokes which are synchronized and focused on the sample. The pump beam is modulated at high frequency, typically at half the laser repetition rate. In this case, the Stokes beam which is filterd after the sample, is sent to a linear interferometer that creates two collinear identical replicas of the pulse, with variable relative delay Δt. The two replicas interfere onto a single detector, giving rise to an interferogram in function of the delay Δt, called "Stokes Interferogram". According to the Wiener-Khinchin theorem [40] , the FT of the interferogram with respect to Δt gives the spectrum of the Stokes pulse. The SRG signal of the Stokes beam modifies the interferogram generating tails at long delays. In this way, the FT of the new interferogram results in a different spectrum of the Stokes which shows gain in the form of sharp peaks at specific Stokes frequencies. By computing the so called differential transmission as the difference between the pumped and unpumped Stokes spectra and normalizing over the unpumped Stokes spectrum, one obtains the SRG spectrum. In order to distinguish on the Stokes spectrum the pump-induced modification, it is necessary to work at high-speed modulation transfer and to use lock-in detection. Thanks to the linearity of the FT operator, the difference of the FTs of the two interferograms is equal to the FT of their difference. We take advantage of this property, by first obtaining directly the difference of the two Stokes pulse interferograms using a lock-in amplifier.

In FT-SRS the two delayed replicas are generated through a common-mode birefrigent interferometer called Translating-Wedge-based Identical pulses eNcod-

ing System (TWINS) [46] [47]. It is a passive delay line capable of generating two pulse replicas with attosecond control of their relative delay, thanks to its common-path geometry.
In TWINS, the energy of the input beam is equally distributed into two perpendicularly polarized components that collinearly propagate along the fast and slow axes of the birefringent material. The delay between the two pulses can be controlled by varying the thickness of the birefringent material, inserting the wedges in and out of the beam through a motorized translation stage. In the standard TWINS configuration,a polarizer at the output projects the two replicas into a common polarization state (at 45° with respect to the two orthogonal polarization directions), to observe their interference.
Currently, the time required for the acquisition of a single FT-SRS spectrum is limited to a fraction of a second by the translation speed of the birefringent wedges. However, there are two strategies that can be used to decrease the measurement time by several orders of magnitude: step scanning and undersampling. The first consists in recording a full SRS image for a given interferometer delay, and performing the FT operation for all pixels in parallel only at the end of the measurement. The second strategy consists in sampling the interferogram at a frequency lower than the Nyquist limit, thus considerably reducing the number of points.

Chapter 2

Supercontinuum generation

This chapter deals with the theoretical description of the process leading to the white light generation (WLG). WLG is a very complex process which involves many nonlinear effects which come into play into a material when the impinging light intensity overcomes a proper threshold. The supercontinuum generation has been one of the most challenging part of our setup, since we aimed to generate a broad Stokes beam covering the spectral range above 1035 nm trying to make it as stable and spectrally wide as possible. A good level of stability, sometimes even higher with respect to that of the fundamental beam that induces the process, can be reached thanks to the intrinsic nature of the filamentation process [8]; on the other side a wide spectral bandwidth can be obtained acting on the intensity of the pump beam, provided that it remains below the damage threshold of the YAG crystal we used for WLG [8].
As it will be presented in Chapter 5, we managed to generate a broadband beam with a spectrum spanning from 1050 nm to 1500 nm and a stability expressed in terms of rms (rms $= \sigma_{\text{energy}}/\langle E \rangle$) around 0.5 %.

2.1 Introduction

Supercontinuum (SC) generation is one of the most spectacular and visually perceptible effects produced by the nonlinear propagation of intense ultrashort laser pulse in a transparent medium. The physical process leading to the SC generation in transparent bulk media can be understood in the framework of femtosecond filamentation [8]. It is a very complex process which involved an intricate coupling between spatial and temporal effects: diffraction, group velocity dispersion, self-focusing, self-phase modulation and multiphoton absorption and ionization. In the space domain, the interplay of these effects leads to the formation of a narrow light channel, termed "light filament" which propagates over extended distances much larger than the typical diffraction length and which leaves a narrow luminous plasma trail in its wake. In the time domain, the pulse undergoes dramatic transformations: pulse splitting or compression, pulse front steepening, and generation of optical shocks. These transformations altogether produce a broadband, spatially, and temporally coherent emission with a low angular divergence (supercontinuum), which is accompanied by the generation of colored

conical emission that is emitted at different angles with respect to the propagation axis. In case of formation of the filament in air, the conical emission is tipically longer than a meter and requires energy of the order of several millijoule. In solids or liquids, using ultrashort laser pulses, it is possible to exploit non-linear optical effects for the generation of filamentation and of the supercontinuum and the required energy is of the order of several microjoule and a conical emission length from few mm to few cm.

2.2 Self-focusing of Laser Beams

When shining a material with a very intense pulse, the response of matter to the electric field is not only due to the linear susceptibility $\chi^{(1)}$ but it is also due to nonlinear terms of the polarization density, which can be written as in Eq.1.4. If we consider a non-centrosymmetric material, the main term among the polarization terms is the third order one, being $\chi^{(2)} = 0$. Therefore, the dielectric polarization becomes,neglecting higher order terms:

$$\vec{P}(t) = \epsilon_0 \left(\chi^{(1)} \vec{E}(t) + + \chi^{(3)} \vec{E}^3(t) \right) \tag{2.1}$$

Recalling that the refractive index of the medium is defined as:

$$n = \sqrt{1 + \chi} \tag{2.2}$$

From Eq.2.1 it is possible to derive:

$$\chi = \chi^{(1)} + \chi^{(3)} |E^2(t)| \tag{2.3}$$

Combining Eq.2.3 and Eq.2.2 the *optical Kerr effect* establishes that:

$$n = n_0 + n_2 I \tag{2.4}$$

where $I = \epsilon_0 c n_0 |E^2|/2$ is the field intensity and n_2 is the nonlinear refractive index coefficient, related to $\chi^{(3)}$ by the relation:

$$n_2 = \frac{3\chi^{(3)}}{4\epsilon_0 c n_0^2} \tag{2.5}$$

The coefficient n_2 is positive for most of the dielectric media which means that during the propagation a laser beam induces an increase of the refractive index of the medium proportionally to the intensity. Hence, for a Gaussian beam with a peak of intensity in the center, it means that the beam is exposed to a higher index at the center and a lower index at the edges. Since the effect on the beam is similar to that of a lens, it is called *Kerr-induced self-focusing effect*. Self-focusing effect is a cumulative effect along the propagation as it makes the beam more intense in the center, enhancing the refractive index and in the absence of any saturation effect, self-focusing would end up in a catastrophic collapse at a finite propagation distance.

Moreover, self-focusing always compete with diffraction [41]. Indeed, the intensity-dependent refractive index modifies the phase of the propagating beam but it is the action of diffraction which conveys the changes in the phase induced by non linearity and ultimately leads to self-focusing. In case of a cylindrically symmetric Gaussian beam, the competition between diffraction and self-focusing is determined by the beam power. There is a critical value, called critical power P_{cr} at which the diffraction and self-focusing nonlinearity are exactly balanced. In this case the beam shape remains fixed and the pulse is called *soliton* or *Townes mode*. The value of the critical power has been derived using a model which takes into account only these two processes during the light-matter interaction and it is:

$$P_{cr} = \frac{3.72\lambda^2}{8\pi n_0 n_2} \tag{2.6}$$

Under this ideal model, it turns out that the Townes mode is not stable. This means that if we assume that the Townes mode could be generated in the laboratory, any small perturbation of the beam amplitude or phase would likely be amplified and prevent the beam to propagate as an invariant Townes mode. The physical meaning of this power is that above P_{cr}, the Kerr nonlinearity overcomes diffraction and the beam shrinks upon itself and undergoes a collapse singularity at a finite propagation distance , while below P_{cr}, diffraction overcomes self-focusing and the beam will spread.

2.3 Self-phase Modulation of Laser Pulses

Considering a time-dependent intensity profile, the refractive index varies also in time. The time dependence of the refractive index is responsible of a nonlinear change in the phase of the pulse which can be written as [8]:

$$\Phi_{nl}(t) = \frac{\omega_o}{c} n_2 \int_0^L I(t,z)dz \tag{2.7}$$

where L is the propagation distance inside the medium. If the medium is short enough for the intensity variation along z to be negligible, the nonlinear phase becomes $\Phi_{nl}(t) = \frac{\omega_o}{c} n_2 I(t) L$. It means that a nonlinear phase shift is accumulated during the pulse propagation, this is the reason why this effect is called *self-phase modulation*. This effect will results in a time-varying instaneous frequency:

$$\omega(t) = \omega_0 + \partial\omega(t) \tag{2.8}$$

where $\partial\omega(t) = -(\omega_0 L/c)\, n_2 \partial I/\partial t$.
For a Gaussian laser pulse of duration t_p the variation of the instantaneous frequency is :

$$\partial\omega(t) = 4\frac{\omega_0 L}{c t_p^2} n_2 I_0 t e^{\left(-2\frac{t^2}{t_p^2}\right)} \tag{2.9}$$

The effect leads to the generation of new frequencies, leading to a negative shift of the instantaneous frequency at the leading edge of the pulse and a positive

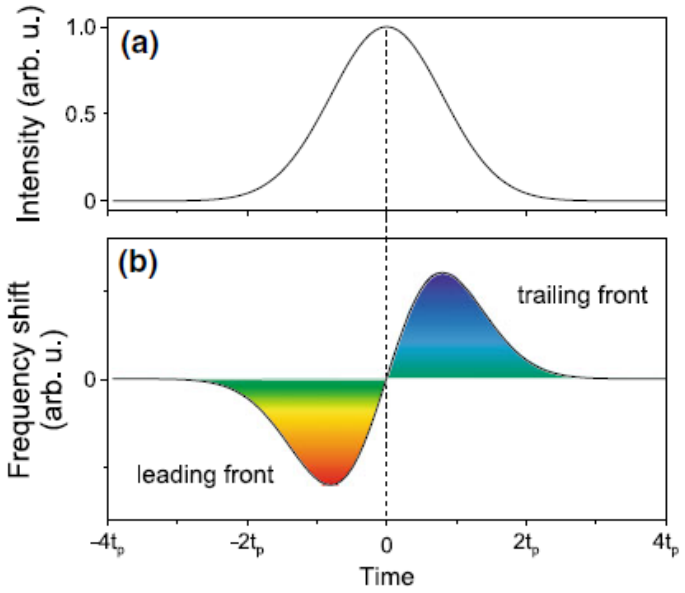

Figure 2.1: Self-phase modulation of a Gaussian pulse (a) which produces a variation of the instantaneous frequency with time (b). From [8]

shift of the instantaneous frequency at the trailing edge of the pulse. So there will be red-shifted spectral component at the pulse leading edge and blue-shifted spectral component at the pulse trailing edge (see Fig. 2.1). Considering pure self-phase modulation and looking at Fig.2.1 one can notice that same frequencies are generated at two different times, so each colour could give interference leading to the modulation of the spectrum (Fig. 2.2).

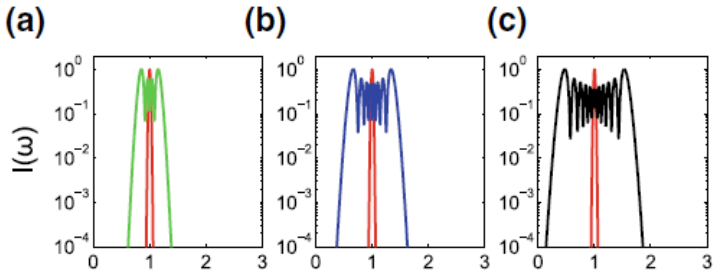

Figure 2.2: Self phase modulation of a pulse whose original spectrum is in red with propagation distance of one (a), two (b) and three (c) length units for a symmetric Gaussian pulse. From [8]

2.4 Nonlinear Absorption and Ionization

As reported in Section2.2, as the beam self-focuses, its intensity increases and so does the nonlinear refractive index, resulting in an enhancement of the effect of self-focusing. If this process continued, it would result on a catastrophic collapse of the beam. Nevertheless, this effect does not actually take place thanks to

saturation processes such as multiphoton absorption and ionization, responsible for energy loss and generation of a free electron plasma, which further absorbs and defocuses the beam. The combination of self-focusing and saturation processes leads the intensity to a certain level called the *clamping intensity*. This quantity depends on the material's order of multiphoton absorption:

$$K = \langle \frac{U_g}{\hbar\omega_0} \rangle + 1 \tag{2.10}$$

where U_g is the bandgap and $\hbar\omega_0$ is the photon energy. The higher the order of multiphoton absorption, the higher the clamping intensity,thus leading to a wider spectral broadening. Hence, the broadest supercontinuum spectrum can be obtained for dielectrics with a wide bandgap.

2.5 Plasma Effects

In presence of ionization of a dielectric medium, electrons are promoted from the valence band to the conduction band and this promotion corresponds to the absorption of K photons with an energy larger than the bandgap. This process results in conduction electrons whose density transition rate varies in time proportionally to the K-th power of the laser intensity I [8]:

$$\frac{\partial \rho}{\partial t} = \frac{\beta_K}{K\hbar\omega_0} I^K \tag{2.11}$$

where β_K is the multiphoton absorption coefficient. The conduction electrons will modify the refractive index of the material, according to the following relationship:

$$n = n_0 - \frac{\rho}{2n_0\rho_c} \tag{2.12}$$

where $\rho_c = \epsilon_0 m_e \omega_0^2 / e^2$ is the critical plasma density beyond which the plasma becomes opaque to an electromagnetic density at ω_0. Considering a Gaussian beam, the plasma density is tipically larger in the center of the beam compared to the feet.Therefore, from Eq.2.12, it follows that there is a bigger reduction of the refractive index in the center of the beam. This means that the electrons in the conduction band will induce a phase curvature similar to that of a beam passing a defocusing lens. The overall effect is that the beam intensity decreases and its diameter increases leading to a so-called *plasma defocusing*.

Another effect, associated with plasma defocusing is the self-phase modulation induced by the plasma. Indeed, the nonlinear phase change is:

$$\phi_{nl}(t) = -\frac{\omega_0 L}{c} \frac{\rho(t)}{2n_0\rho_c} \tag{2.13}$$

Similar to the effect due to third-order non linearity, this non-linear phase shift leads to a variation in time of the instantaneous frequency, that for a Gaussian beam is:

$$\partial\omega(t) = \frac{\omega_0 L}{c}\frac{\beta_K I_0^K}{K\hbar\omega_0 2n_0\rho_c}e^{-\frac{2Kt}{t_p^2}} \tag{2.14}$$

This effect is called *plasma-induced phase-modulation* which gives rise to frequency which are all positive, so to a blueshift of the spectrum.

For the seek of completeness, one can give a mathematical formula to express the clampling intensity. By looking at the refractive index change due to the two different processes (self-focusing and saturation effects), it holds:

$$n_2 I_{cl} = \frac{\rho_{cl}}{2n_0\rho_c} \tag{2.15}$$

Assuming for simplicity a constant pulse with duration t_p, the plasma density can be roughly written as $\rho = \beta_K \left(K\hbar\omega_0\right)^{-1} I_K t_p$, therefore the clamping intensity becomes:

$$I_{cl} = \left(\frac{2n_0 n_2 \rho_c K\hbar\omega_0}{\beta_K t_p}\right)^{\frac{1}{K-1}} \tag{2.16}$$

From Eq. 2.16 it is easy to understand that the clamping intensity depends on the material properties through the nonlinear index coefficient n_2, on the multiphoton absorption coefficient β_K and on number of photon absorbed K and as, we have anticipated before, the higher is the order of multiphoton absorption K the higher is the clamping intensity.

2.6 Chromatic dispersion

Another relevant phenomenon which comes into play when dealing with white light generation is the chromatic dispersion, that is due to the fact that waves of different frequencies travel at different velocities in a dielectric medium, resulting in the temporal spreading of the light pulse. Indeed, the fastest frequencies will eventually propagate in the leading edge of the pulse, while the slowest frequencies in the trailing edge. In this case the pulse is said to be positively chirped. Chromatic dispersion can also lead to a compression of the pulse if the pulse entering the medium is initially negatively chirped.
Chromatic dispersion is due to the dependence of the refractive index of the material $n(\omega)$ on the frequency ω. In order to quantify the chromatic dispersion, one can start by fitting the refractive index curve in the trasparency region with the Sellmeier relations, that express the refractive index as a function of the wavelength:

$$n^2(\lambda) = a_0 + \sum_{j=0} N\frac{a_j}{\lambda_j^2 - \lambda^2}. \tag{2.17}$$

Chromatic dispersion can be classified in normal and anomalous dispersion. In order to distinguish them, the propagation constant of the pulse can be expressed as:

$$k(\omega) = n(\omega)\frac{\omega}{c} \tag{2.18}$$

By expanding it around the central frequency of the laser pulse ω_0, one can write:

$$k(\omega) = k(\omega_0) + k_0'(\omega - \omega_0) + \frac{k_0''}{2}(\omega - \omega_0)^2 \tag{2.19}$$

where $k_0' = \partial k/\partial(\omega)|_{\omega_0}$ is the inverse of the group velocity v_g and $k_0'' = \partial^2 k/\partial(\omega)^2|_{\omega_0}$ is the group velocity dispersion coefficient or GVD. For a given material, the region of normal dispersion corresponds to positive value of GVD, where the red colours travel faster than the blue ones. While, the region of anomalous dispersion corresponds to negative value of GVD, where the blue components travel faster than the red ones.

2.7 Self-steepening and Space-Time Focusing

The combination of the non linear effects and chromatic dispersion gives rise to self-steepening. Indeed, the Kerr nonlinearity modifies not only the refractive index of the medium but also the group index, via the interplay with dispersion:

$$n^{(g)} = n_0^{(g)} + n_2^{(g)} \tag{2.20}$$

where $n_0^{(g)} = n(\omega_0) + \omega_0 dn/d\omega|_{\omega_0}$ and $n_2^{(g)}$ is proportional to n_2 and positive. As a result the intense part of the pulse travels at a smaller velocity with respect to the low intensiry feet, resulting in a steepening of the trailing edge of the pulse. Space-time focusing refers to the effect of diffraction into cone angles for the different frequency components of an ultrashort pulse.

2.8 Femtosecond filamentation

Femtosecond filamentation refers to the ability of powerful femtosecond laser pulses to propagate nonlinearly over distances of several diffraction lengths in a medium with Kerr nonlinearity. The main process which leads to the generation of filamentation is self-focusing through which the laser beam gets narrow and intense enough to deposit its energy into a needle-shaped region along the propagation axis. Because of the strong light-matter interaction in this region, there could be the generation of an electron-hole plasma and the emission of new radiations. This phenomenon was first reported to happen in air by the team of Mourou [43] in 1995, where the femtosecond filamentation was obtained by means of multi-gigawatt femtosecond laser pulses, while the first manifestation in trasparent solids was reported in 2001 [44], using femtosecond laser with few megawatts peak power.
One of the main proof of femtosecond filamentation is represented by the conical emission of white light. It is accompanied by axial supercontinuum generation. By looking at the laser beam cross-section one can observe that several meters after the termination of the filament it shows a white central spot sorrounded

by colored rings, whose wavelengths decrease from the central to the outer rings. The conical filamentation has been observed for filamentation in media of varoius nature and laser of different central wavelengths. Fig.2.3 shows two example of conical emission due to femtosecond filamentation.

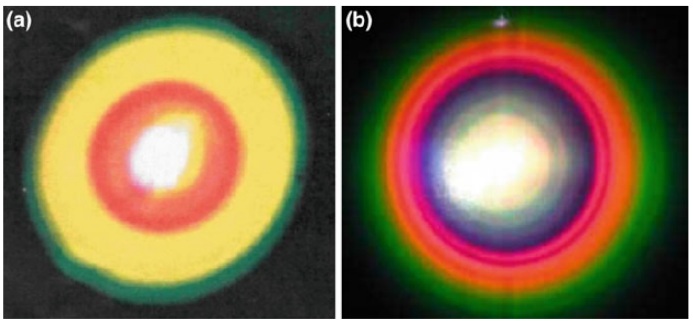

Figure 2.3: a) Conical emission accompanying filamentation in air. Image of the beam crossection after propagation of a terawatt laser pulse over 40 m. b) Conical emission from a filament in a ZK7 glass. From [8]

2.9 Supercontinuum generation in bulk media

This section will briefly explains the processes involved in supercontinuum generation [45] taking into account all the effects we have introduced theoretically in this chapter.
The spectral broadening of a laser pulse impinging onto a nonlinear crystal results from the interplay of nonlinear effects during propagation through a medium: the driving laser is focused inside a crystal at intensities leading to accumulation of nonlinear effects. With self-focusing, the beam size shrinks, leading to increased intensities. The increased intensity generates plasma, freeing electrons, which defocus the beam. When the plasma defocusing compensates the self-focusing, a filament is created. During propagation, other nonlinear effects contribute to the broadening: self-steepening shortens the trailing edge of the pulse in time and leads to a broadening towards shorter wavelengths.

Chapter 3

Linear optics

This chapter deals with a brief theoretical description of the linear propagation of ultrashort pulses in dieletric media, studying the particular case of gaussian pulses and giving an expression of the pulse duration after the propagation in a medium once the initial duration is known. This formula will be useful in Chapter 5 for the calculation of the pulse duration after the propagation in a H-ZF4 rod. Such a rod has been inserted in the setup for a stretching of the pulse before entering into a non-zero dispersion shifted single-mode fiber, used for realizing the photon time stretch-SRS (PTS-SRS) detection stage for the SRG signal retrieval. The final section of this chapter deals with propagation of pulses inside a single-mode (SM) fiber, describing the dispersion properties of different SM fibers. The basic fundamentals of propagation in SM fibers are presented for the understanding of the pulse propagation in the fiber and for the calibration procedure necessary to create a time-to-wavelength map of the broadband pulse propagating in it.

3.1 Linear propagation of ultrashort pulses

In the realization of the optical setup for broadband coherent Raman spectroscopy and imaging, the pulses which are used have a duration which is of the order of hundreds of femtoseconds. In order to get a physical insight in the processes which governs the propagation of such ultrashort pulses, it is necessary to start from the Maxwell's equations which are at the basis of all electromagnetic phenomena [10]. The Maxwell's equation, in the case of a non magnetic medium ($\vec{M} = 0$, $\chi_m = 0$) and no current and charge density sources ($\rho = 0$, $\vec{J} = 0$), have been introduced in Chapter 1 (Eq. 1.31; 1.32; 1.33; 1.34) together with the wave equation for a medium with a refractive index n (Eq. 1.36).
By adopting the scalar approximation, assuming that the electric field is linearly polarized, and the plane wave approximation, for which the electric field is constant in a plane perpendicular to the propagation direction, it is possible to write the electric field as:

$$\begin{aligned} E(z,t) &= A(z,t)cos\left[\omega_0 t - k_0 z + \phi(z,t)\right] \\ &= \Re\{A(z,t)e^{i[\omega_0 t - k_0 z + \phi(z,t)]}\} \end{aligned} \tag{3.1}$$

where (z,t) is called the envelope of the electric field and the sinusoidal term is

the carrier wave which oscillates at a carrier frequency ω_0 and $\phi(z,t)$ is the phase associated to the electric field which varies with time and z (Fig.3.1).

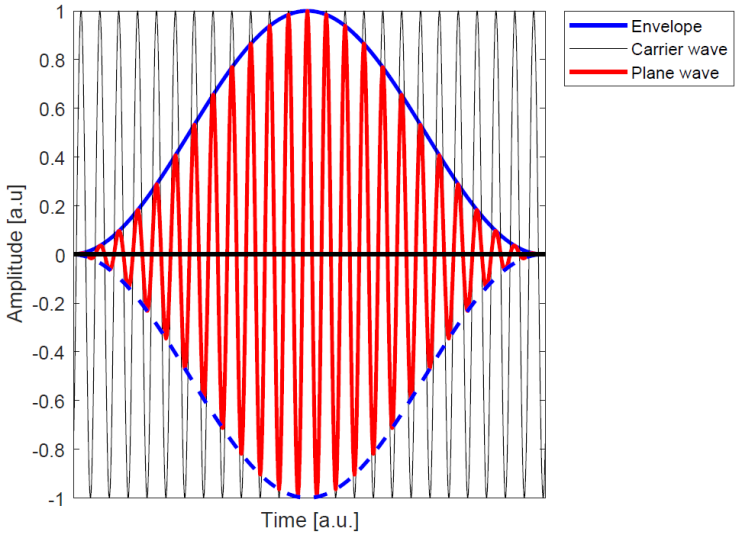

Figure 3.1: Graph representing the electric field shape for a linearly polarized plane-wave propagating in the z-direction (in red). The blue function represents the envelope, while the black one the carrier wave.

Since we are considering the linear propagation of ultrashort pulses in a dispersive medium, we can substitute in P the linear term of polarization($P_L = \epsilon_0 \chi^{(1)} E$) and by doing the Fourier transform, passing into the frequency domain, the wave propagation equation becomes:

$$2ik_0 \frac{\partial \tilde{A}}{\partial z} = \left[k^2(\omega) - k_0^2\right] \tilde{A} \tag{3.2}$$

where Eq. 3.2 has been derived within the slowly varying envelope approximation (SVEA). Recalling that $k(\omega) = 2\pi n(\omega)/\lambda_0$, so considering a dispersive medium in which the refractive index varies with ω, it is possible to write:

$$k^2(\omega) - k_0^2 = (k(\omega) - k_0)\,(k(\omega) + k_0) \approx 2k_0\,(k(\omega) - k_0) \tag{3.3}$$

Doing a Taylor expansion of $k(\omega)$ around ω_0:

$$k(\omega) = k(\omega_0) + \left(\frac{dk}{d\omega}\right)_{\omega_0} (\omega - \omega_0) + \frac{1}{2}\left(\frac{d^2k}{d\omega^2}\right)_{\omega_0} (\omega - \omega_0)^2 + \frac{1}{6}\left(\frac{d^3k}{d\omega^3}\right)_{\omega_0} (\omega - \omega_0)^3 \tag{3.4}$$

At this point, define the phase velocity and the group velocity. The phase velocity is the speed at which the carrier moves and it is defined as:

$$v_p = \frac{\omega}{k} \tag{3.5}$$

While the group velocity is the speed at which the envelope moves and it is defined as:

$$v_g = \frac{d\omega}{dk} \tag{3.6}$$

Hence, in the Eq. 3.4, substitute the first and second derivative of the wavevector k with respect to ω with the following quantity:

$$\left(\frac{dk}{d\omega}\right)_{\omega_0} = \frac{1}{v_g} \tag{3.7}$$

$$\left(\frac{d^2k}{d\omega^2}\right)_{\omega_0} = \mathrm{GVD} \tag{3.8}$$

where GVD stands for the group velocity dispersion of the material.
By inserting Eq.3.4 with the definition of Eq.3.7 and Eq.3.8, coming back to the time domain and by choosing a proper frame of reference ($z' = z$, $t' = t - z/v_{g0}$), it is possible to derive the parabolic equation which tells how the amplitude of the electric field A change in a dispersive medium during propagation:

$$\frac{\partial A}{\partial z} - \frac{i}{2}\mathrm{GVD}\frac{\partial^2 A}{\partial t^2} = 0 \tag{3.9}$$

Eq.3.9 can be solved going back into the frequency domain and find how the amplitude evolve after a propagation distance L and than anti-trasforming it. Following this procedure the generic solution is:

$$A(t, L) = \frac{1}{2\pi}\int_{-\infty}^{+\infty} \tilde{A}(\omega, 0)e^{-\frac{i}{2}\mathrm{GVD}L\omega^2}e^{i\omega t}\, d\omega \tag{3.10}$$

where $\tilde{A}(\omega, 0)$ is the Fourier transform of the amplitude of the electric field at $z = 0$.

Linear propagation of Gaussian pulses in a dispersive medium

The propagation of ultrashort pulses in a dispersive medium can be studied for the case of a Gaussian pulse, for which the calculation in terms of Fourier transform and inverse Fourier transform are easy to be computed. The Gaussian pulse shape at $z = 0$ can be expressed as:

$$A(0, t) = A_0 e^{-\frac{t^2}{2\tau_p^2}} \tag{3.11}$$

where τ_p is defined as the characteristic time constant of the pulse and it corresponds to the time at which its intensity has been attenuated by a factor $1/e$ with respect to the maximum value at $t = 0$. In optics, the pulse duration is defined by looking at the full width at half maximum (FWHM) of the intensity profile of the pulse($|A(0, t)|^2 = A_0^2 \exp(-t^2/\tau_p^2)$). By simple calculation, it is possible to express the pulse duration as a function of the characteristic time constant τ_p:

$$\Delta t_{\mathrm{FWHM}} = 2\tau_p\sqrt{\log 2} \tag{3.12}$$

The pulse profile at the output of the sample, after a propagation distance L can be written as:

$$A(z, t) = \frac{A_0\tau_p}{\sqrt{\tau_p^2 + iD_2}}e^{-\frac{t^2}{2(\tau_p^2 + iD_2)}} \tag{3.13}$$

where $D_2 = \text{GVD} \cdot L$. From previous expression, it is evident that the pulse shape is still a gaussian function, but it is a complex function that can be also expressed as:

$$A(z,t) = \frac{A_0 \tau_p}{\sqrt{\tau_p^2 + iD_2}} e^{-\frac{t^2}{2\tau_{OUT}^2}} e^{-i\phi(t)} \tag{3.14}$$

where τ_{OUT} is the pulse duration at the output and $\phi(t)$ is the phase acquired by the pulse during the propagation, which can be written as:

$$\tau_{OUT} = \tau_p \sqrt{1 + \left(\frac{D_2}{\tau_p^2}\right)^2} \tag{3.15}$$

$$\phi(t) = \frac{D_2 t^2}{2\left(\tau_p^4 + D_2^2\right)} \tag{3.16}$$

The output pulse duration can be also expressed in function of the propagation distance z:

$$\tau_{OUT} = \tau_p \sqrt{1 + \left(\frac{z}{L_D}\right)^2} \tag{3.17}$$

where $L_D = \tau_p^2/\text{GVD}$ is the dispersion length. Hence, for a medium with high GVD, the dispersion length is short and so after a short propagation in that medium the pulse duration increase abruptly after a short propagation distance z. Moreover, the dispersion length is related to the square of the characteristic time constant τ_p of the pulse. This implies that very short pulses are very sensitive to dispersion, since they get longer in time after a short distance, being L_D very short. On the other hand, long pulses are more robust to dispersion.

3.2 Dispersion in single-mode fibers

Single-mode fibers support only one mode, called the fundamental mode [9]. The fiber is designed such that all the higher-modes are cut off at the operating wavelength. While in multimode fibers, the intermodal dispersion plays a relevant role, since the different modes travel at different propagation speeds along the fiber, which means that different modes launched at the same time reach the output end of the fiber at different times; in single-mode fibers, intermodal dispersion is absent, simply because the energy of the injected pulse is transported by a single mode. However, pulse broadening does not disapper. Indeed, the group velocity associated with the fundamental mode is frequency dependent because of chromatic dispersion. As a consequence different spectral components travels with slightly different group velocities, thus having *Group velocity dispersion* (GVD), also called *intramodal dispersion* or simply *fiber dispersion*. Intramodal dispersion has two main contributions: material dispersion and waveguide dispersion.

3.2.1 Group-Velocity Dispersion

Consider a single-mode fiber of length L. A component at frequency ω would arrive at the output of the fiber after a time delay $T = L/v_g$ where v_g is the *group velocity*, defined as:

$$v_g = \left(\frac{d\beta}{d\omega}\right)^{-1} \tag{3.18}$$

where β is the wavevector of the mode propagating into the fiber. By assuming that $\beta = nk_0 = n\omega/c$, one can show that $v_g = c/n_g$, where n_g is the *group index* given by:

$$n_g = n + \omega\left(\frac{dn}{d\omega}\right) \tag{3.19}$$

If $\Delta\omega$ is the spectral width of the pulse, the temporal pulse broadening for a fiber of length L is governed by:

$$\Delta T = \frac{dT}{d\omega}\Delta\omega = \frac{d}{d\omega}\left(\frac{L}{v_g}\right)\Delta\omega = L\frac{d^2\beta}{d\omega^2}\Delta\omega = L\text{GVD}\Delta\omega \tag{3.20}$$

where $\text{GVD} = d^2\beta/d\omega^2$. In some optical communication systems, the frequency spread $\Delta\omega$ is determined by the range of wavelength emitted by the optical source $\Delta\lambda$. Recalling that $\omega = 2\pi c/\lambda$ and $\Delta\omega = (-2\pi c/\lambda^2)\Delta\lambda$, Eq.3.20 can be written as:

$$\Delta T = \frac{d}{d\lambda}\left(\frac{L}{v_g}\right)\Delta\lambda = DL\Delta\lambda \tag{3.21}$$

where

$$D = \frac{d}{d\lambda}\left(\frac{1}{v_g}\right) = -\frac{2\pi c}{\lambda^2}\text{GVD} \tag{3.22}$$

D is called the *dispersion parameter* and is expresses in units of $\text{ps}/(\text{km}\cdot\text{nm})$. Since we have seen that the coefficient GVD is the group velocity dispersion

coefficient, and being $D \propto -\text{GVD}$, we can say that in the spectral region where $D < 0$, the fiber has a normal dispersion, hence the red-shifted components arrive before the blue-shifted ones; while in the spectral region where $D > 0$, the fiber has an anomalous dispersion, hence the red-shifted components arrive after the blue-shifted ones.
The wavelength dependence of D is governed by the frequency dependence of the mode index n. From Eq.3.22, D can be written as:

$$D = -\frac{2\pi c}{\lambda^2}\frac{d}{d\omega}\left(\frac{1}{v_g}\right) = -\frac{2\pi}{\lambda^2}\left(2\frac{dn}{d\omega} + \omega\frac{d^2n}{d\omega^2}\right) \tag{3.23}$$

At this point to express the dispersion parameter D as the sum of waveguide and material dispersion contributions (see [9]) a normalized frequency V or simply V parameter as $V = k_0 a(n_1^2 - n_2^2)^{1/2}$ and a normalized propagation constant b as $b = (\beta/k_0 - n_2)/(n_1 - n_2) = (n - n_2)/(n_1 - n_2)$ are introduced, where n_1 is the core refractive index and n_2 is the cladding refractive index and a is the core radius. Hence, it is possible to substitute $n = n_2 + b(n_1 - n_2)$ to Eq. 3.23 and D can be written as the sum of two terms:

$$D = D_M + D_W \tag{3.24}$$

where the *material dispersion* D_M and the *waveguide dispersion* D_W are given by:

$$D_M = -\frac{2\pi}{\lambda^2}\frac{dn_{2g}}{d\omega} = \frac{1}{c}\frac{dn_{2g}}{d\lambda} \tag{3.25}$$

$$D_W = -\frac{2\pi\Delta}{\lambda^2}\left[\frac{n_{2g}^2}{n_2\omega}\frac{Vd^2(Vb)}{dV^2} + \frac{dn_{2g}}{d\omega}\frac{d(Vb)}{dV}\right] \tag{3.26}$$

with n_{2g} the group index of the cladding material.

Material dispersion arises from the change in a material's refractive index with wavelength. Therefore, it leads to the change of the propagation velocity of light as a function of wavelength. Waveguide dispersion is a separate effect arising from the geometry of the fiber optic waveguide. Waveguide properties are a function of wavelength, consequently, changing the wavelength affects how light is guided in a single mode fiber as a change in the distribution of light in the cladding and core.
For standard step-index single mode fiber (Fig.3.2), the sum of the material and waveguide dispersion is zero near 1310 nm, which makes 1310 nm the zero-dispersion wavelength (ZDW).
By modifying the fiber's waveguide structure, the waveguide dispersion can be shifted up or down, thus shifting the ZDW toward longer or shorter wavelengths, as seen in Fig.3.3. Tipically, if the ZDW is shifted to 1550 nm, the fiber is called dispersion-shifted fiber.
Shifting the ZDW to 1550 nm is not always the best strategy. When multiple optical channels pass through the same fiber at wavelengths where dispersion is very close to zero, they suffer from a type of crosstalk called four-wave mixing.

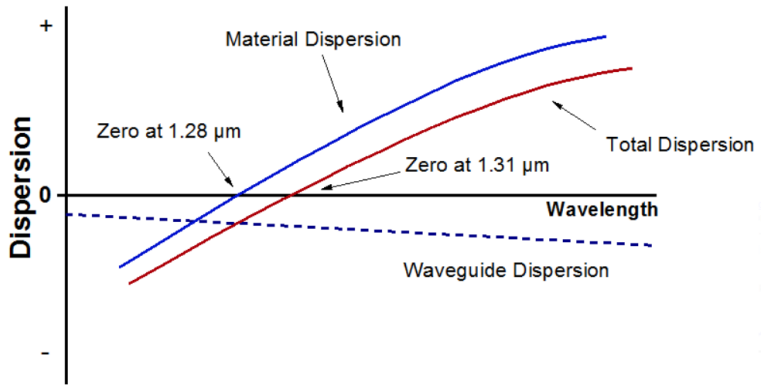

Figure 3.2: Waveguide dispersion offsets chromatic dispersion to produce zero dispersion at 1310 nm in step-index SMF. From [54]

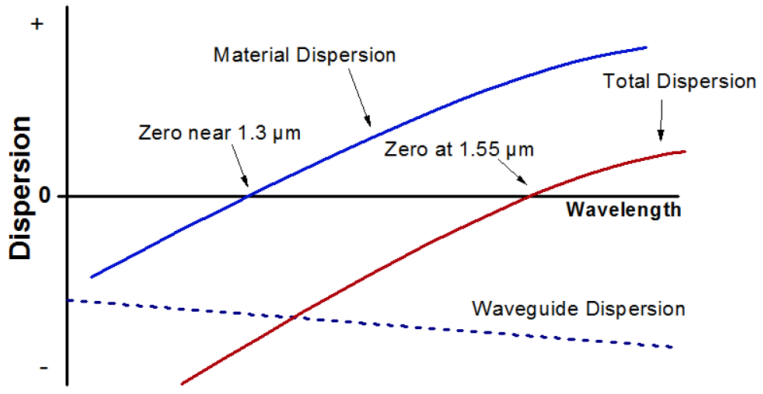

Figure 3.3: A fiber designed with more waveguide dispersion shifts the zero-dispersion wavelength to 1550 nm. From [54]

The degradation is so severe that dispersion-shifted fiber cannot be used for dense WDM systems. To avoid four-wave mixing, the ZDW is moved outside the transmission band, as seen in Fig.3.4. Fibers with this property and a low, but non-zero dispersion in the C-band, are called *non-zero dispersion-shifted fibers*.

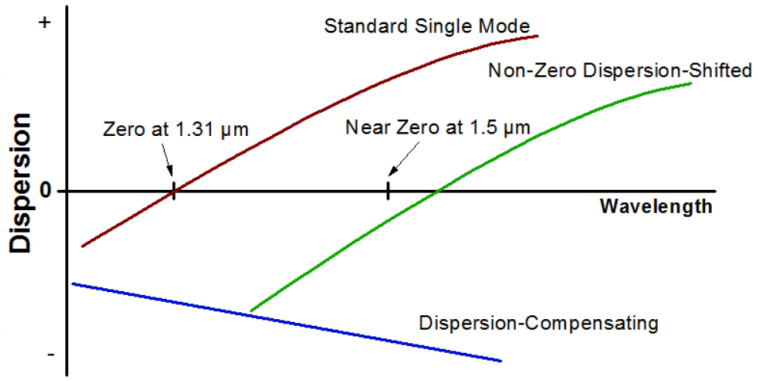

Figure 3.4: This graph shows different types of SMF. In red the non-zero dispersion SMF, where the ZDW is shifted towards wavelengths higher than 1550 nm. From [54]

In our setup we have adopted a non-zero dispersion shifted single-mode fiber to realize a photon time stretch SRS (PTS-SRS). The necessity of using such a fiber has been strictly due to the fact that we would like to stretch a pulse with a broad spectrum spanning from 1050 nm to 1500 nm. Therefore, it has been necessary to choose a fiber for which the dispersion of the material maintains the same sign for all the spectral extension of the impinging pulse, avoiding to have the zero-dispersion wavelength within the pulse wavelength range. This condition is fully satisfied by the non-zero dispersion shifted SM fiber, for which the dispersion parameter remains negative for the whole pulse spectral range. It means that the dispersion introduced by the chosen fiber is a normal dispersion, that is the red-shifted components arrive earlier than the blue-shifted one, as the graphs in section 5.6 shows.

Chapter 4

Frequency-Resolved Optical Gating

In our setup we deal with ultrashort pulses whose duration is of the order of hundreds of fs or several picoseconds. Measurement of pulses on these time scales is an important issue, since the speed required is considerably faster than that of existing photodetectors and oscilloscopes. There are several methods which allow us to resolve femtosecond pulses. Some of them are the so-called correlation measurements, which are widespread experimentally but which offer only partial information about the optical pulse. In order to get a complete information about the pulse shape and than reveal both complete intensity and phase information, it is possible to follow frequency-resolved optical gating approach based on time-frequency analysis concepts as well as techniques based on frequency filtering and on interferometry.
This chapter deals with the main characteristic of a particular technique of frequency resolved optical gating (FROG), which is the second harmonic generation-FROG. It briefly introduces the theory behind the technique, passing then to the description of the part of experimental setup used to perform the FROG measurements.

4.1 Introduction

The main idea behind FROG is that of measuring a spectrogram of the field. The main experimental requirement in measuring ultrafast optical spectrograms is in implementing an ultrafast gate function. In FROG, as in other ultrashort-pulse measurement technique, the pulse is used to gate itself via a non linear optical interaction. Indeed, by changing, with a motorized translational stage, the delay between the pulse-gate and the pulse itself, it is possible to acquire for a given delay the spectrum of the gated signal [10].
Writing the electric field of the pulse as $E(t)$ and that of the delayed pulse as $E(t-\tau)$ where τ is the delay between the two pulses, the gated signal is:

$$E_{gated}(t,\tau) = E(t)E(t-\tau) \tag{4.1}$$

and the correspondent spectrogram:

$$\begin{aligned} S_{FROG}(\omega,\tau) &= \left| \int_{-\infty}^{+\infty} E_{gated} e^{-i\omega t} dt \right|^2 \\ &= \left| \int_{-\infty}^{+\infty} E(t)E(t-\tau)e^{-i\omega t} dt \right|^2 \end{aligned} \tag{4.2}$$

The pulse duration can be retrieved from the intensity autocorrelation plot. Indeed, by integrating the spectrogram for the different value of frequency ω, one obtains the value intensity as a function of the delay τ. Once, the intensity autocorrelation has been retrieved, it can be fitted with a Gaussian or with the squared of an hyperbolic secant. The pulse duration Δt_{pulse} will be related to the full width at half maximum of the intensity autocorrelation according to:

- for a Gaussian fit:

$$\Delta t_{pulse} = \frac{\Delta t_{AC}}{1.44} \tag{4.3}$$

- for a $sech^2(\cdot)$ fit:

$$\Delta t_{pulse} = \frac{\Delta t_{AC}}{1.55} \tag{4.4}$$

4.2 SHG-FROG

There are several non linear interactions which can be used in FROG measurements, the one which has been used for the pulse duration retrieval in our setup is based on second harmonic generation (SHG), which is a second-order nonlinearity, known as SHG-FROG. The geometry which is used in SHG-FROG is similar to the noncollinear SHG intensity autocorrelation setup, where a spectrometer is used in place of the detector. By defining the spectrogram as in Eq.4.2 is evident that it is a symmetric function of τ, indeed:

$$S_{FROG}(\omega,\tau) = S_{FROG}(\omega,-\tau) \tag{4.5}$$

This is not surprising, since the pulse and the gating function are identical and therefore one cannot tell whether the pulse is ahead the gating function or the gating function is ahead the pulse.
A further consequence of Eq.4.2 is that the fields $E(t)$ and $E(-t)$ have identical SHG-FROG traces. Moreover, measuring the traces of a transform-limited Gaussian pulse or of a linearly chirped Gaussian pulse, one can notice that there are qualitatively differences between the two traces, since as the chirp is increased, the trace gets wider along the axis relative to the delay τ. Nevertheless, identical traces are obtained for equal-magnitude positive and negative linear chirps. This last feature illustrates the main disadvantage of SHG-FROG: the inability to determine the sign of a chirp.

4.3 Signal Recovery from FROG Trace

From FROG traces, as it has been pointed out from previous discussions, it is possible to retrieve electric field pulse shape. With respect to the correlation measurements which are widely used for detecting ultrashort pulses but which allow us only to reconstruct the amplitude of the pulse, FROG measurements are particularly useful to reconstruct the pulse both in terms of amplitude and phase. Indeed, if $E_{sig}(t,\tau)$ is known, $E(t)$ can be obtained by direct integration:

$$\int E_{sig}(t,\tau)d\tau = \int E(t)g(t-\tau)d\tau \approx E(t) \tag{4.6}$$

Therefore, the problem is how to determine the signal $E(t,\tau)$. In order to do it, it is possible to express the FROG trace in terms of $\tilde{E}_{sig}(t,\Omega)$, which is the Fourier transform of $E(t,\tau)$ with respect to τ:

$$S_{FROG}(\omega,\tau) \approx \left| \int \int \tilde{E}_{sig}(t,\Omega)e^{-j\omega t}dtd\Omega \right|^2 \tag{4.7}$$

where

$$\tilde{E}_{sig}(t,\Omega) = \int E_{sig}(t,\tau)e{-}j\Omega\tau, d\tau \tag{4.8}$$

Eq. 4.7 represents a phase-retrieval problem, since the main purpose is to recover $\tilde{E}_{sig}(t,\Omega)$ and hence $E_{sig}(t,\tau)$ from its two dimensional power spectrum. While this problem has not a unique solution in a one dimensional problem, it turns out that in a two-dimensional problem it is possible almost always to recover a unique solution.

Trebino and co-workers have published several algorithms for recovering electric field profile from FROG data [42]. Indeed, there is no possibility in reconstructing the pulse directly, but in an indirect way using an iterative algorithm (see Fig. 4.1).

The first step is to guess for $E(t)$, than we multiply it for the gate function $g(t-\tau)$ thus finding $E_{sig}(t,\tau)$, then we do the Fourier transform with respect to t, obtaining $\tilde{E}_{sig}(\omega,\tau)$. At this point one applies the experimental data by replacing the magnitude of $\tilde{E}_{sig}(\omega,\tau)$ with the magnitude of the FROG data while leaving it phase unchanged, that is,

$$\tilde{E}_{sig}(\omega,\tau) \to \frac{\tilde{E}_{sig}(\omega,\tau)}{\left|\tilde{E}_{sig}(\omega,\tau)\right|}\sqrt{S_{FROG}(\omega,\tau)} \tag{4.9}$$

Obtained the new value of $\tilde{E}'_{sig}(\omega,\tau)$, inversing Fourier transform it with respect to ω to get a new $E'_{sig}(t,\tau)$ and then integrating it with respect to τ, one obtains an estimate of $E(t)$ which is called $E'(t)$. This completes one iteration. The algorithm continues by using the updated version of $E(t)$ until the solution converges.

One way to check for convergence is to compare the results corresponding to iteration k , that is $E^{(k)}(t)$ ans $\tilde{E}^{(k)}_{sig}(\omega,\tau)$ with that of the previous iteration. Another way is to compute the error between the computed and experimental values. Since

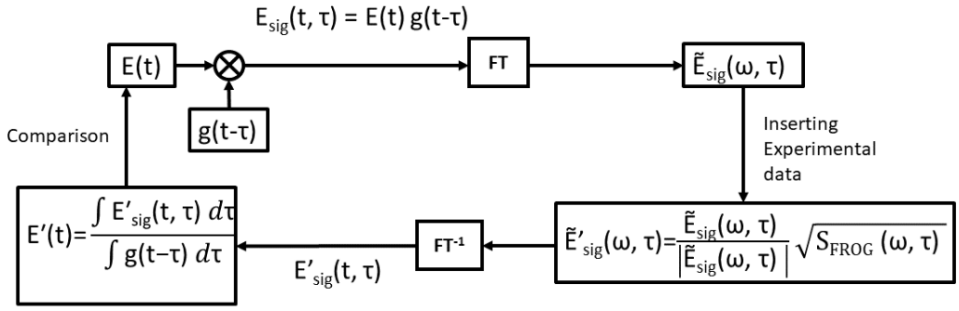

Figure 4.1: Iterative Fourier transform algorithm for retrieving the ultrashort-pulse amplitude and phase from FROG Data.

$E(t)$ is not known directly from the experiments, one cannot compute the error in $E^{(k)}(t)$. However, one can use $\tilde{E}^{(k)}_{sig}(\omega,\tau)$ for comparison with actual FROG data. In particular it is defined the rms FROG error, defined by [10]:

$$\epsilon_{FROG} = \left\{ \frac{1}{N^2} \sum_{i=1}^{N} \left[S^{(k)}_{FROG}(\omega_i,\tau_i) - S_{FROG}(\omega_i,\tau_i) \right]^2 \right\}^{1/2} \tag{4.10}$$

where $I^{(k)}_{FROG}(\omega,\tau) = \left|\tilde{E}^{(k)}_{sig}(\omega,\tau)\right|^2$. The algorithm should be run until the FROG error cannot be made any smaller.

4.4 Experimental setup

In Fig. 4.2 is represented the geometry that has been used to perform SHG-FROG. After the first mirror, the beam is splitted in two beams by a beam splitter (BS1) which undergoes different paths. One of the two beams goes in a delay line which is implemented by using an MMC-PI motor whose minimum step is 14 nm. The delay is, indeed, controlled by the position of the motor and each step of the motor corresponds to a delay equal to 14/300 fs . By mean of a second beam splitter (BS2) the two beams are than collimated and the second pinhole (PH2) is used just to align the two beams. Through a concave mirror the two beams which are now in a non-collinear configuration cross in correspondence of a BBO crystal, which is is a nonlinear optical crystal with wide transparency region, broad phase-matching range, large nonlinear coefficient and high damage threshold. Because of the large nonlinear coefficient ($\chi^{(2)} \neq 0$), after the crystal a second harmonic signal emerges together with the input signal. The signal in which we are interested in is the sum frequency signal which travels straight in between the two emerging signal. This signal varies its intensity according to the delay between the two pulses impinging onto the crystal, showing a peak in correspondence of the zero of the delay. By blocking the input signal through a third pinhole (PH3), the sum frequency signal is collimated through a CaF_2 lens of 50 mm focal length onto the spectrometer (Ocean Optics USB2000-UV+VIS-ES), which just acquires the spectrum for each position of the MMC-PI motor.

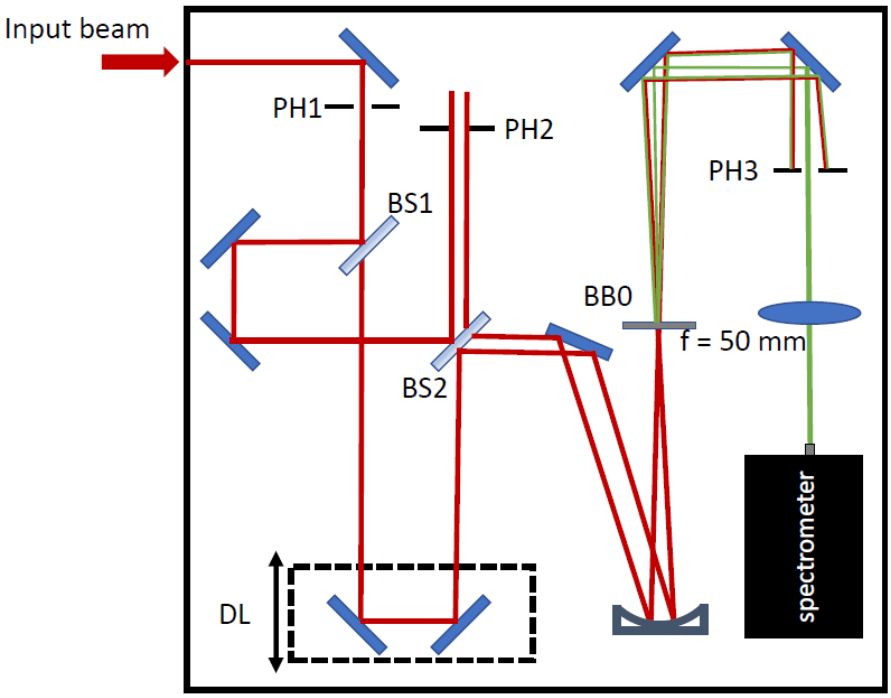

Figure 4.2: Scheme of the SHG-FROG setup. Legend: PH(pinhole) , BS (beam splitter), DL(delay line), BBO (second harmonic generation crystal).

In order to find the position of the crystal which satisfy the phase matching condition, it has been necessary to use a 1 mm BBO crystal since from theory the Intensity of the SHG signal in case of perfect phase-matching condition grows quadratically with the length of the crystal. For the measurements acquisition, a 10 μm BBO crystal has been used which allows a higher phase-matching bandwidth being from theory $\Delta\omega_{\mathrm{FWHM}} \propto 1/L$, with L the length of the SHG crystal. This last requirements is extremely useful for our measurements, since we need a quite large phase-matching bandwidth to acquire the spectrogram relative to the supercontinuum generation.

Chapter 5

Experimental setup

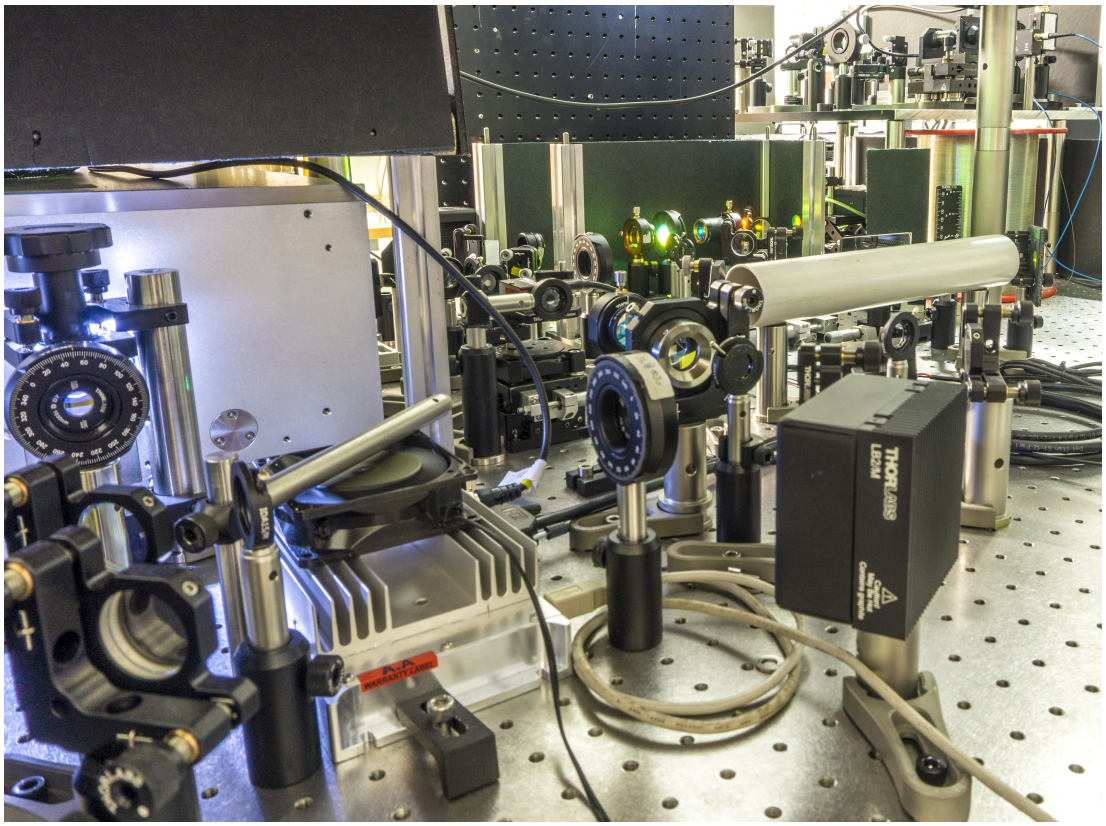

Figure 5.1: Picture of the experimental setup representing the pump and Stokes line.

The overall experimental setup for broadband CRS microscopy and spectroscopy is sketched in Fig.5.2, where the main components have been highlighted. The source is an Ytterbium laser, Coherent Monaco, which works at a repetition rate of 50 MHz, at a wavelength of 1035±5 nm. It provides an energy per pulse greater than 80 μJ, it has an adjustable repetition rate from single-shot to 1 MHz and it works without AOM pulsepicking from 1 to 50 MHz. It provides an output power of 60 W. The pulse width goes from values lower than 350 fs to values higher than 10 ps. For our purpose, we have fixed the time duration of the pulses at 268 fs and a repetition rate of 2 MHz. After the laser, a half-wavelength plate is used to rotate the polarization of the beam so to control the laser power injected into the setup. A first polarizing plate beamsplitter (PBSW-1030) at 1030 nm is used to reflect at 90° the S-polarization of the beam and to transmit the P-polarization. A second half-wavelength plate is used to rotate the polarization and regulate the power which goes into the pump line and the one which goes into the Stokes line. The two lines are created by means of a second PBSW-1030, which transmits the P-polarization for the Stokes line and reflects the S-polarization for the pump line. The two half-wavelength plates are set in such a way that the power of the pump beam is of the order of 100 mW, while the power of the Stokes line is 3.5 W. Such a high avarage power, is necessary for the white light generation (WLG) in a 6 mm-thick YAG crystal. Indeed, from literature [8] [45], it is known that the critical peak power for self-focusing in a YAG crystal is 1.36 MW calculated for a central wavelength of 1030 nm. Considering that the pulse duration of the pump before the crystal is around 270 fs, the energy required is 0.4 μJ. In our setup, we see that the ratio P_{peak}/P_{cr} is of the order of 3-4. Indeed, the average power before the crystal is 2.4 W and the correspondent energy per pulse at 2 MHz rep. rate is 1.2 μJ. These operating condition allows one to operate with a stable supercontinuum light at an avarage power of 100 mW.

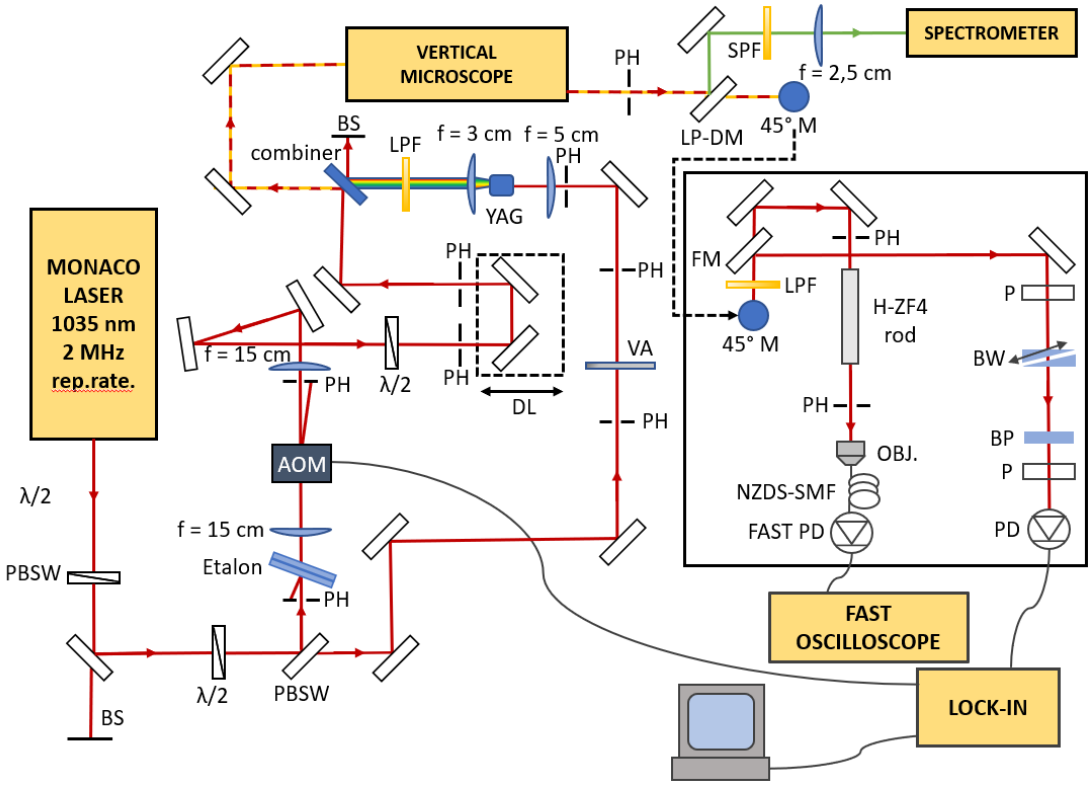

Figure 5.2: Schematic of the experimental setup realized for broadband Coherent Raman scattering microscopy and spectroscopy. Legend: PH, pinhole; BS, beam stopper; PBSW, polarizing plate beam splitter; $\lambda/2$, half-wavelength plate; AOM, acousto-optic modulator; DL, delay line; VA, variable attenuator; LP-DM, long pass dichroic mirror; 45° M, mirror at 45°; LPF, long-pass filter; SPF, short-pass filter; NZDS-SMF, non-zero dispersion shifted single mode fiber; OBJ., objective; PD, photodiode; P, polarizer; BW, birefringent wedges; BP, birefringent plate.

5.1 Pump line

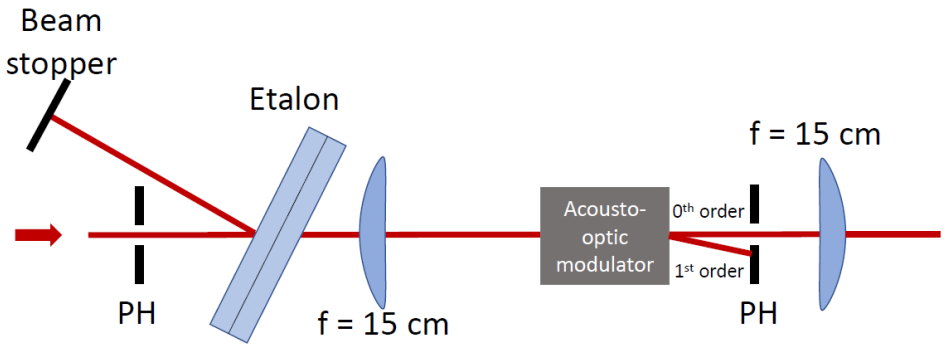

Figure 5.3: Scheme of the pump line after the PBSW. PH, pinhole; The red arrow indicates the propagation direction of the beam (red line).

Fig.5.3 represents schematically the pump stage before the delay line, realized through a mechanic translational stage. The pump line is constituted by a pinhole used to align the beam towards the etalon (see Appendix B). The etalon is inserted in the setup at an angle such that the transmitted intensity is maximized and spectrally centered at 1035 nm and the reflected beam is blocked by a beam stopper. The transmitted part goes into a plano-convex lens with focal length of 15 cm. The converging lens is meant to focalize the beam into an acousto-optic modulator or AOM (AA Opto-Electronic, MT200-A0.2-1064). The AOM is coated in order to properly operate in the wavelength range between 800 nm and 1064 nm. The acusto-optic modulator works at a picking ratio of 1/2, in a way such that the pump at 2 MHz repetition rate is modulated at 1 MHz. The focalized beam after the AOM is diffracted, thus having two orders after it: order zero and order one. The pinhole positioned after the AOM is meant to select the beam at order zero, because the modulation efficiency is high (84 %) and the beam is more intense than the one at order one. Eventually a second converging plano-convex lens of 15 cm focal length collimates the beam. As shown in Fig. 5.2, after the etalon the pump goes into the delay line, constituted by a mechanical translational stage, to temporally synchronize pump and Stokes. To rotate the polarization of the pump, that now is S-polarized, a third half-wavelength plate is inserted in this stage. In this way, before the combiner, pump and Stokes have the same polarization. The combiner is a 1064 nm single-edge laser dichroic beam splitter (Di02-R1064-25x36, Semrock) whose transmission is shown in Fig. 5.4.

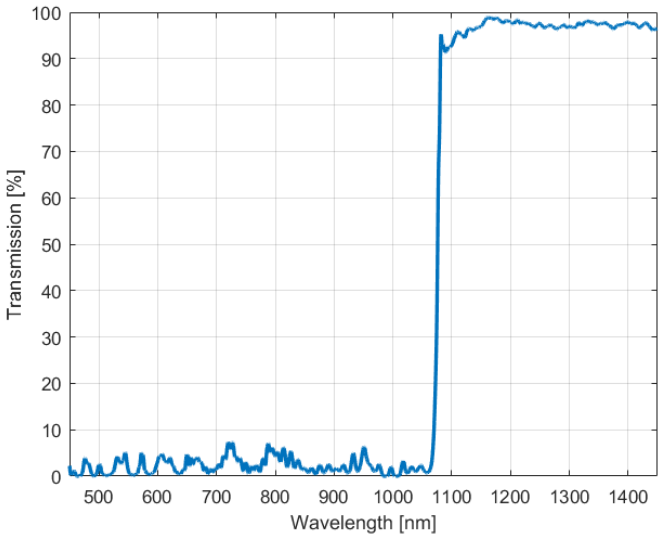

Figure 5.4: Transmission of the 1064 nm single-edge laser dichroic beam splitter using as combiner of pump and Stokes. Adapted from [56]

5.1.1 Characterization of the pump beam

This subsection shows some measurements performed on the pump beam before and after the etalon. In particular, the pulse has been reconstructed using the SHG-FROG approach, described in Chapter 4. By means of a software, it has been possible to characterize the pulse in term of duration in time and also to determine its temporal shape, retrieving the relative spectrum, by Fourier transforming it. In the end, the reconstructed spectrum of the pump before and after the etalon has been compared with the measurements performed with a spectrometer with a good agreement between the two results.
Fig.5.5 shows the FROG trace measured using a spectrometer (Ocean Optics USB2000-UV+VIS-ES). The motorized translational stage has been set in a way such that the delay between the two replicas of the pulse goes from -900 fs to 900 fs. While the number of spectra that have been acquired is 201. As expected from theory, the FROG trace is symmetric.
From the FROG trace, it is possible to reconstruct the temporal shape of the pulse by using the algorithm we presented in Fig. 4.1. The result is shown in Fig.5.6, where the pulse has a Gaussian shape as the Gaussian fit (red line) shows. From this pulse reconstruction we can estimate the duration of the pump pulse before the etalon which is 282 fs, not too far from the expected value of 268 fs we have chosen from the interface of the Monaco laser.
Another way from which one can retrieve the pulse duration is by extrapolating from the FROG trace the intensity autocorrelation of the pulse. The procedure which has been used consists in intengrating the intensity of the beam for different wavelengths and then plotting the overall intensity as a function of time, thus obtaining the graph in Fig. 5.7. As already explained in Chapter 4, the pulse duration can be retrieved by fitting the graph using a Gaussian function or the square of the hyperbolic secant function and than calculating the FWHM

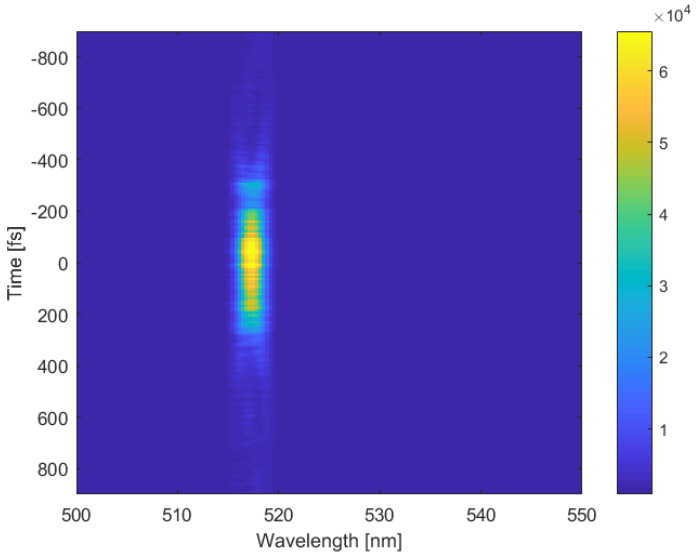

Figure 5.5: FROG trace for the pump before the etalon which is obtained by scanning the motorized translational stage from -900 fs to 900 fs and acquiring 201 spectra. The colorbar represents the intensity of the beam in terms of counts.

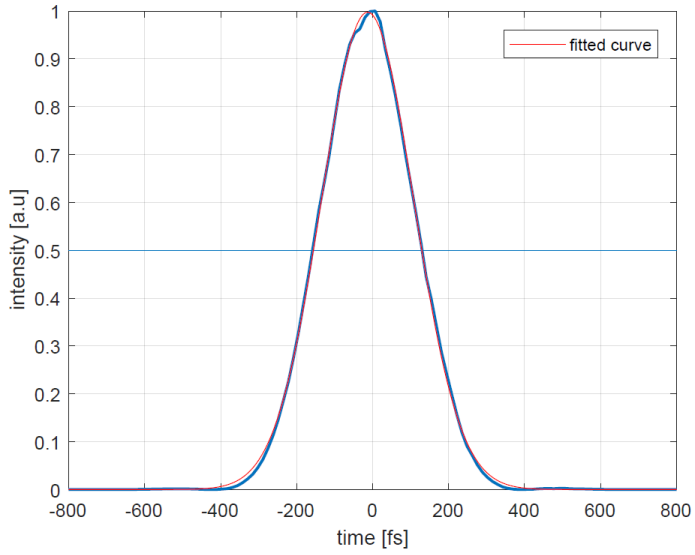

Figure 5.6: Pulse reconstruction in time using the SHG-FROG algorithm seen in Chapter 4 for the pulse before the etalon. Fitting of the pulse reconstruction through a gaussian. The pulse duration calculated as FWHM is 282 fs.

of the fitting function. Without lose of generality, I have fitted the intensity autocorrelation with a sech^2 function of the type:

$$a \cdot \text{sech}^2(b(x-c)) \tag{5.1}$$

where a,b and c are adjustable coefficients. Recalling that the pulse duration in this case is related to the FWHM of the intensity autocorrelation by the following relation:

$$\Delta t_{pulse} = \frac{\Delta t_{AC}}{1.55} \tag{5.2}$$

a pulse duration of $\Delta t_{pulse} = 272fs$ has been calculated, which is close to the expected value of 268 fs.

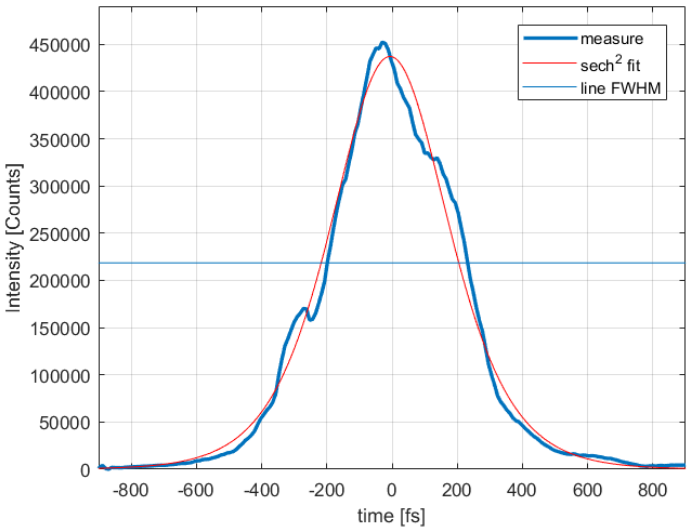

Figure 5.7: Intensity autocorrelation of the pump before the etalon (blue curve). Fitting of the curve with a sech^2 (red curve) and calculation of the duration of the pulse from the FWHM (light blue line) of the curve which is 272 fs.

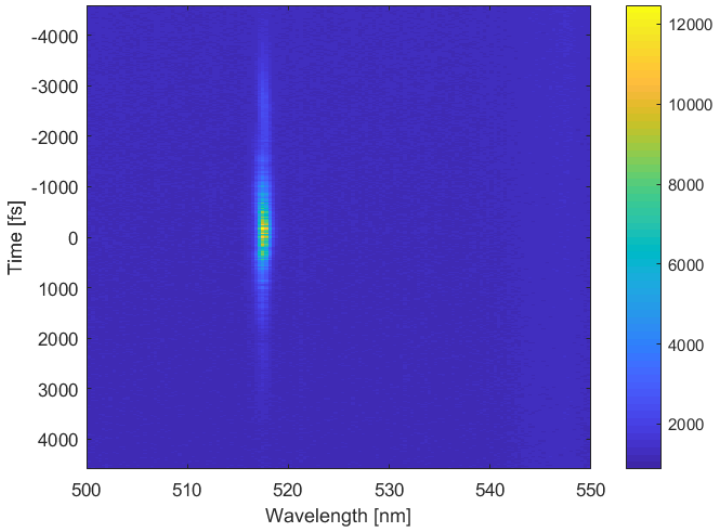

Figure 5.8: Frog trace for the pump before the etalon which is obtained by scanning the motorized translational stage from -4600 to 4600 fs and acquiring 401 spectra. The colorbar represents the intensity of the beam in terms of counts.

The same approach has been followed for the case of the pump after the etalon. In this case the FROG trace obtained by setting the motorized translational stage such that the delay between the pulses varies between -4600 fs and 4600 fs and acquiring 401 spectra is presented in Fig. 5.8.
Also in this case, it has been possible to reconstruct the temporal shape of the pulse, as shown in Fig.5.9. In this case, the pump after the etalon does not have anymore a perfect gaussian shape as the best fitting with a gaussian function shows. The pulse duration calculated as the FWHM of the temporal shape of the pulse is 612 fs.
A better estimation of the pulse duration can be obtained by plotting the intensity autocorrelation and fitting it with the square of an hyperbolic secant function. Fig. 5.10 shows the intensity autocorrelation and the fitting function (red curve). The pulse duration in this case is 980 fs. As expected, since the etalon shrinks the spectrum of the pump, the duration which at the beginning is of the order of 272 fs, now becomes almost 1 ps.

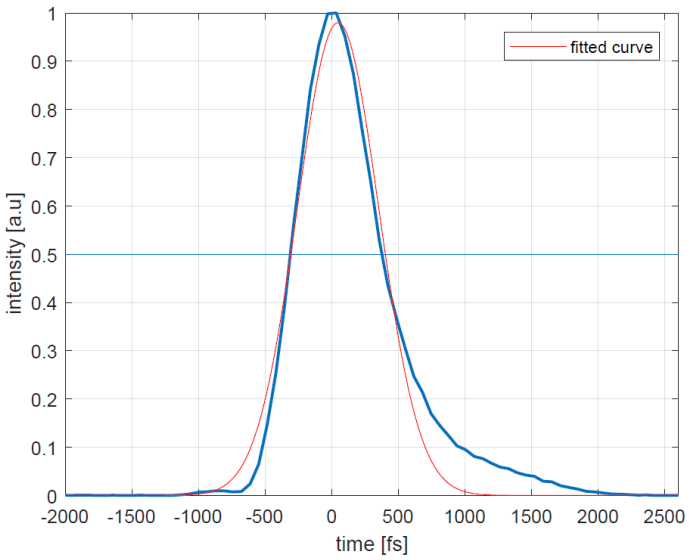

Figure 5.9: Pulse reconstruction in time using the SHG-FROG algorithm seen in Chapter 4 for the pulse after the etalon. Fitting of the pulse reconstruction through a gaussian. The pulse duration calculated as FWHM is 612 fs.

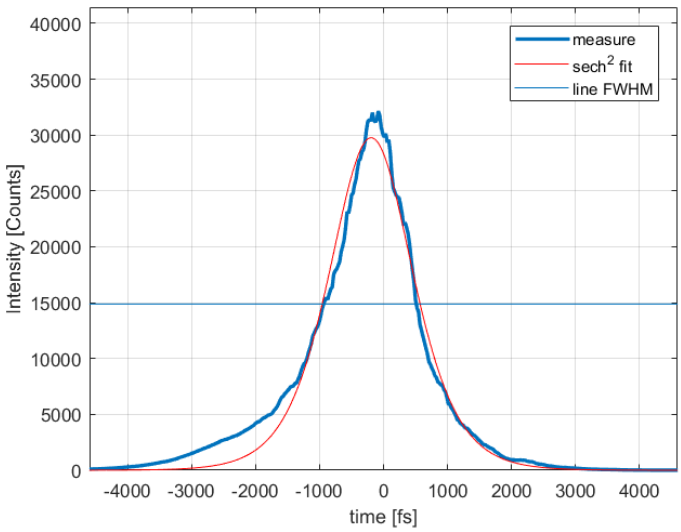

Figure 5.10: Intensity autocorrelation of the pump after the etalon (blue curve). Fitting of the curve with a sech^2 (red curve) and calculation of the duration of the pulse as the FWHM (light blue line) of the curve which is 980 fs.

The pulse shape reconstruction which has been done using the SHG-FROG reconstruction algorithm allows us also to retrieve the spectrum of the pulse before and after the etalon, by simply Fourier transforming the two temporal shape. Fig.5.11 shows the two spectra relative to the pump before (blue line) and the pump after (red line) the etalon. It is evident that the main function of the etalon is to reduce the bandwidth of the pulse, indeed the FWHM before of the pulse before the etalon is 6.5 nm, while after the etalon it becomes 1.4 nm. The central wavelength of the pulse after the etalon, according to this spectral reconstruction, is at 1030.2 nm. The reason why the spectra of the pump before and after the etalon are not centered at the same wavelength can be explained considering that the measurements have not be taken at the same moment, so also the angle with which the beam enters the spectrometer can play an important role in determining the position in wavelength of the peak.

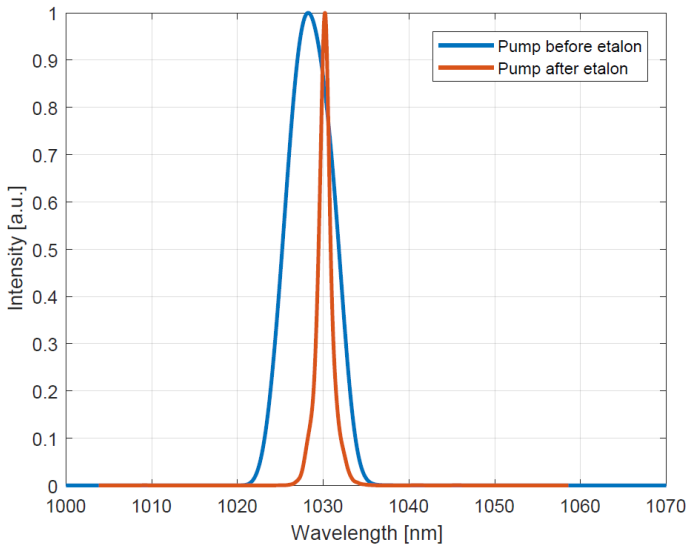

Figure 5.11: Normalized spectrum of the pump before (blue line) and after (red line) the etalon obtained by Fourier transforming the two reconstructed pulses. Central wavelength for the pulse before the etalon 1028.2 nm; central wavelength for the pulse after the etalon 1030.2 nm.

The spectrum that has been found by using the SHG-FROG setup can be compared with the one measured with a spectrometer (Ocean Optics, NIR 256-2.5). Fig. 5.12 shows the spectra of the pump before and after the etalon. In this case, the central wavelength of the pump is at 1035 nm while the bandwidth of the spectrum calculated as FWHM of the pulse before and after the etalon are 18.85 nm and 1.45 nm, respectively. The mismatch between the values of the central wavelengths measured with the two methods can be explained considering the fact they have been measured using two different spectrometer. In any case, the main purpose was to show the fact the the beam is narrowed in bandwidth after the etalon till to 1.4 nm.

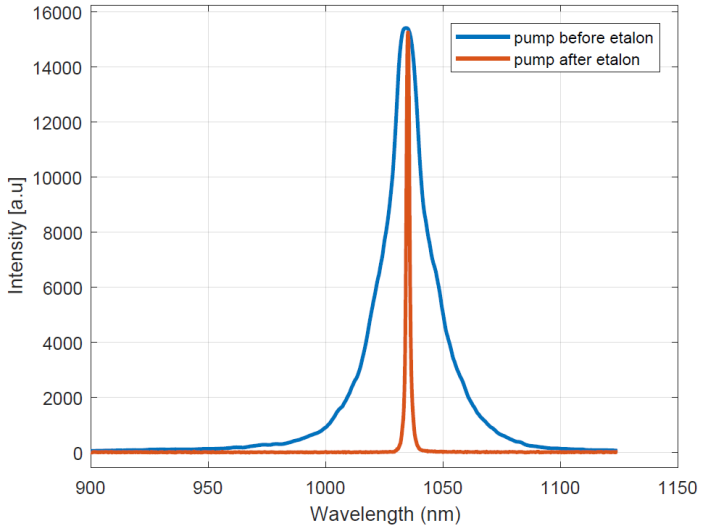

Figure 5.12: Spectrum of the pump before (blue line) and after (red line) the etalon measured using a spectrometer. Central wavelength for the pulse before the etalon 1035.2 nm; central wavelength for the pulse after the etalon 1035 nm.

5.2 Stokes line: white light generation stage

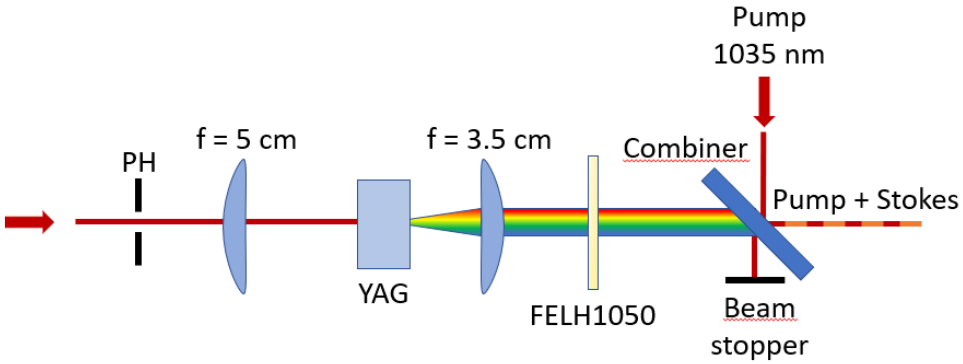

Figure 5.13: Schematic of the white light generation stage. PH, pinhole. The red arrow indicates the direction of propagation of the beam (red line).

Fig.5.16 shows the white light generation stage. The P-polarized beam, transmitted by the PBSW, goes into a plano-convex lens of focal length f = 5 cm. A pinhole, positioned before the lens, is used to regulate the ray bundle which illuminates the YAG crystal. The aperture of the pinhole has an impact on the spectral width of the supercontinuum, because it allows one to act on the diffraction of the beam. After the crystal, positioned in corrispondence of the focus of the first lens, a second plano-convex lens of f = 3.5 cm collects the WLG. This lens is positioned such that the Stokes beam stays collimated for a very long distance, without diverging. Since the WLG has a very large spectrum that spans from the visible till the NIR, a FELH1050 filter is put soon after the lens in order to filter out the wavelengths below 1050 nm and so to reject the pump beam which is still

present after the YAG crystal. A combiner (Di02-R1064-25x36, Semrock) is used to further remove the components below 1064 nm, indeed these components are reflected and stopped by a beam stopper, while it transmits all the components above 1064 nm (see image 5.4 in section 5.1).

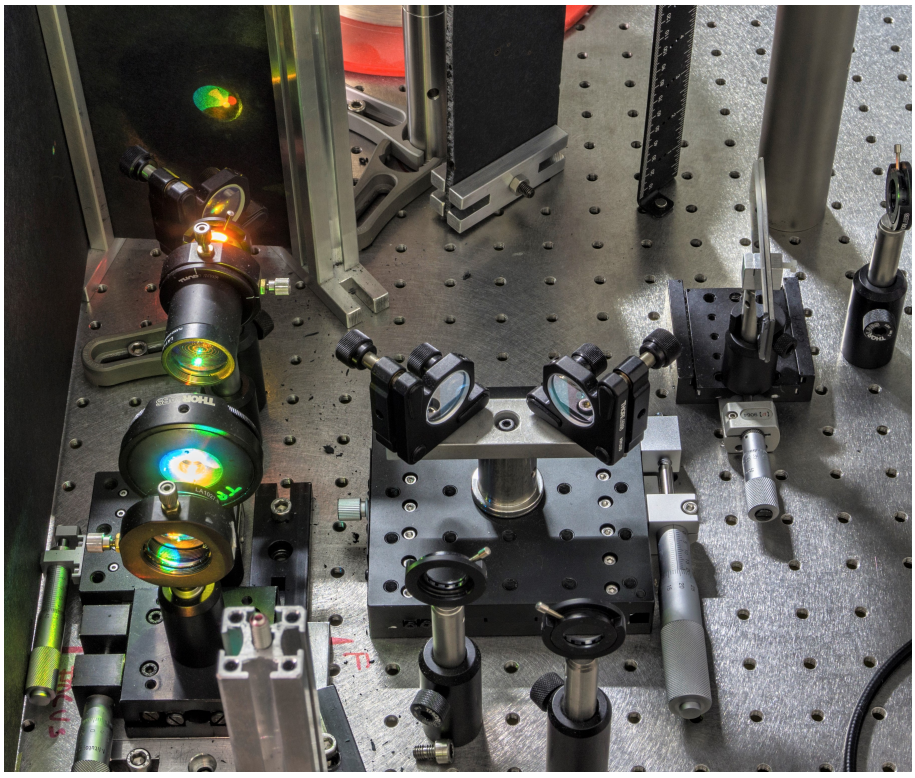

Figure 5.14: Picture of the white light generation.

5.2.1 Measurements on the Stokes line

The WLG has represented one of the most challenging part of the setup, indeed, the main difficulty is to realize a supercontinuum (shown in Fig. 5.14) with high stability. From the practical point of view, the parameters that play an important role for the stabilization of the WLG are:

- the power of the laser shined onto the YAG crystal, which has been controlled by a variable attenuator (see Fig.5.2);
- the focal length of the lens before the crystal; indeed, we have noticed that a long focal length will result in a long Rayleigh distance of the gaussian beam after the lens, resulting in a damaging of the crystal and in a blinking of the WLG which shuts down after few minutes from its generation;
- the pinhole positioned before the lens, through which one regulates the diffraction of the beam which impinges on the YAG crystal, thus the numerical aperture;

- the position of the YAG crystal which has to be placed with the first face in correspondence of the focus of the first converging lens;
- isolation of the WLG stage to avoid thermal fluctuation.

Notice that no problem have been encountered relative to the cooling of the crystal. To test it, we have tried to mount the crystal on a rotational plate but no difference in terms of stability came out rotating it. Different measurements of stability have been done and the parameter we have tried to minimize is the rms (root mean square). We have considered sequence of 20000 consecutive pulses, acquiring the data by mean of a fast oscilloscope (Teledyne Le Croy, HDO 6104) and then we have computed the energy per each pulse and represented the data using an histogram (Fig. 5.15). The rms relative to the distribution has been defined as:

$$\text{rms} = \frac{\sigma_{\text{energy}}}{< E >} \tag{5.3}$$

where σ_{energy} is the standard deviation of the energy distribution and $< E >$ is the mean value of the energy over the ensemble of the 20000 pulses. The energy of each pulse has been calculated by integrating the pulse over its duration. The best result we have obtained is a rms = 0.5 % which is the one shown in Fig. 5.15. We have performed numerous measurements on stability and the value does not differ too much from this value. The maximum value of rms measured is around 0.6 %.

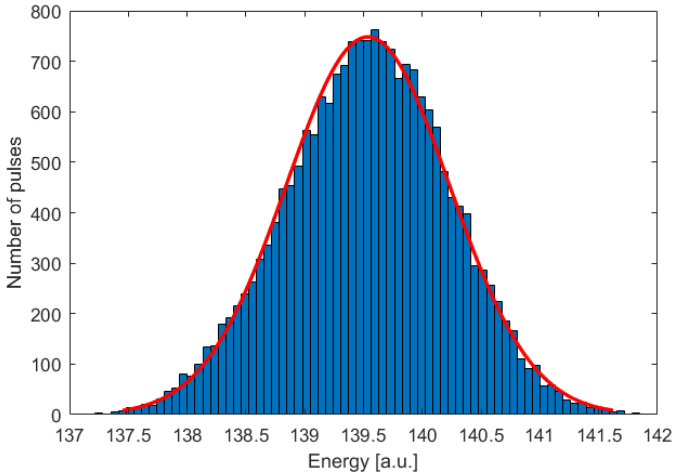

Figure 5.15: Histogram representing the distribution of the pulse energy of the WLG. Statistics on a sequence of 20000 consecutive pulses.rms = 0.5 %

The spectrum of the white light generation, acquired with a spectrometer (Ocean Optics, NIR 256-2.5) is reported in Fig. 5.16. It has an edge at 1050 nm due to the FELH1050 and to the combiner, that suppresses all the wavelengths below 1050 nm, and it extends up to 1500 nm. The corrisponding interval of vibrational resonances that can be probed can be computed as follows. Recalling that the CARS angular frequency is:

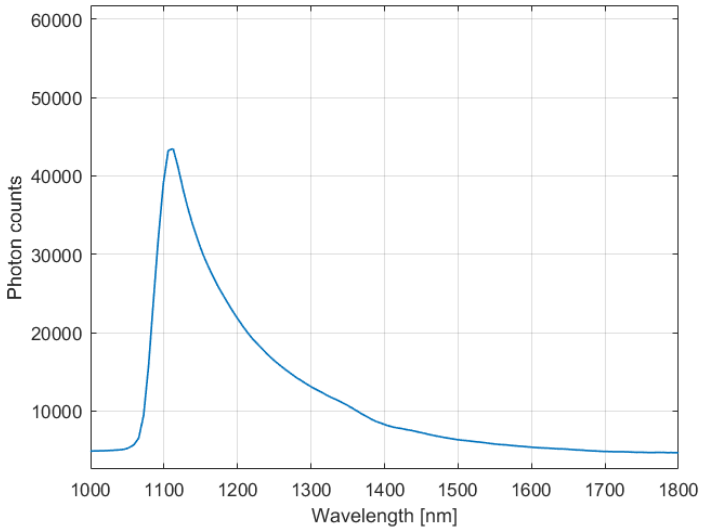

Figure 5.16: Spectrum of the WLG measured using a spectrometer (Ocean Optics, NIR 256-2.5).

$$\omega_{\text{CARS}} = \omega_p - \Omega = \omega_p - (\omega_s - \omega_p) = 2\omega_p - \omega_s \tag{5.4}$$

Substituting $\omega = 2\pi/\lambda$:

$$\frac{2\pi}{\lambda_{\text{CARS}}} = 2\frac{2\pi}{\lambda_p} - \frac{2\pi}{\lambda_s} \tag{5.5}$$

The CARS wavelength is:

$$\lambda_{CARS} = \frac{1}{\frac{2}{\lambda_p} - \frac{1}{\lambda_s}} \tag{5.6}$$

Inserting $\lambda_p = 1035$ nm and the outer value of the Stokes wavelengths (1050 nm and 1500 nm, respectively), the CARS signal spans:

$$\lambda_{\text{CARS}} = 790.1 - 1020.4 \text{ nm} \tag{5.7}$$

The relationship between the CARS wavelength and the wavelength corresponding to the vibrational transition λ_{vibr} is:

$$\omega_{\text{CARS}} - \omega_p = \Omega \rightarrow \frac{2\pi}{\lambda_{\text{CARS}}} - \frac{2\pi}{\lambda_p} = \frac{2\pi}{\lambda_{vibr}} \tag{5.8}$$

In literature, one prefer to express the vibrational transition in cm^{-1}, since $\tilde{\nu}_{vibr} = 10^7/\lambda_{vibr}\ [\text{cm}^{-1}]$, therefore:

$$\tilde{\nu}_{vibr} = 10^7 \left(\frac{1}{\lambda_{\text{CARS}}} - \frac{1}{\lambda_p} \right) \tag{5.9}$$

Inserting the value of λ_p and λ_{CARS}, $\tilde{\nu}_{vibr}$ varies in the range:

$$\tilde{\nu}_{vibr} = 138 - 2995 \text{ cm}^{-1} \tag{5.10}$$

which is sufficient to cover the whole fingerprint region (600-1800 cm^{-1}), where the spectrum contains the contributions from proteins and nucleic acids, and part of the high wavenumber window (2700-3100 cm^{-1}) corresponding to the stretching of the hydrogen bonds (C-H, N-H, O-H).

As we have already done for the pump line, we have performed some measurements for the characterization of the WLG pulse, in particular to have an estimation of its duration. By using the SHG-FROG setup, we have discussed in chapter 4, we acquired the FROG trace of the WLG pulse.

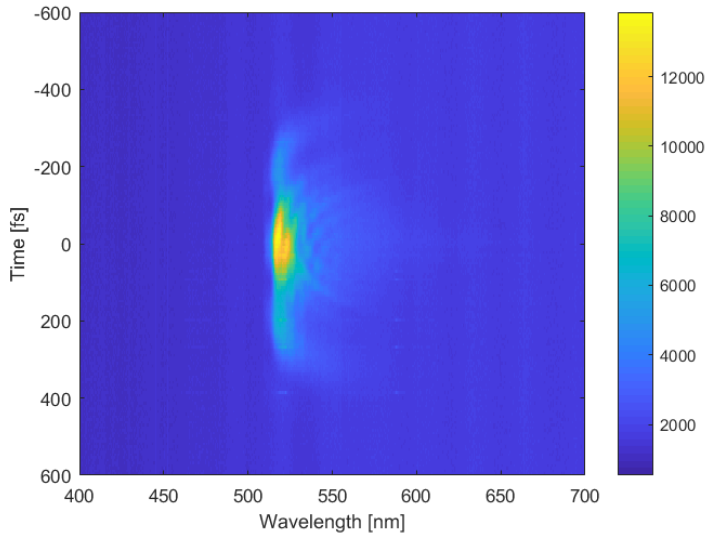

Figure 5.17: Frog trace for the WLG obtained by scanning the motorized translational stage from -600 to 600 fs and acquiring 201 spectra. The colorbar represents the intensity of the beam in terms of counts.

Fig.5.17 represents the trace obtained by scanning the motorized translational stage between -600 fs and 600 fs and acquiring 201 spectra. In this case, since the WLG has no a narrow bandwidth, as the pump has, the corresponding trace is extended in wavelengths. From the FROG map is possible to reconstruct the intensity autocorrelation of the pulse, integrating over a larger range of wavelengths in order to consider all the components of the WLG pulse (Fig 5.18). Following the same procedure we have already analyzed, it is possible to recover the pulse duration of the WLG which is $\Delta t_{WLG} = 203.9$ fs. This result leads to the conclusion that the WLG pulse has a duration which is shorter than that of the pump has generated it (≈ 270 fs). It does not mean there is an error on our measurement, but is due to the fact that we are measuring the pulse duration after we filter out the component below 1050 nm, to remove the pump beam from the Stokes line. Since we are measuring only the components above 1050 nm, the WLG is related to the leading edge of the pulse only, responsible of the red-shifted components of the spectrum (see Fig. 2.1).

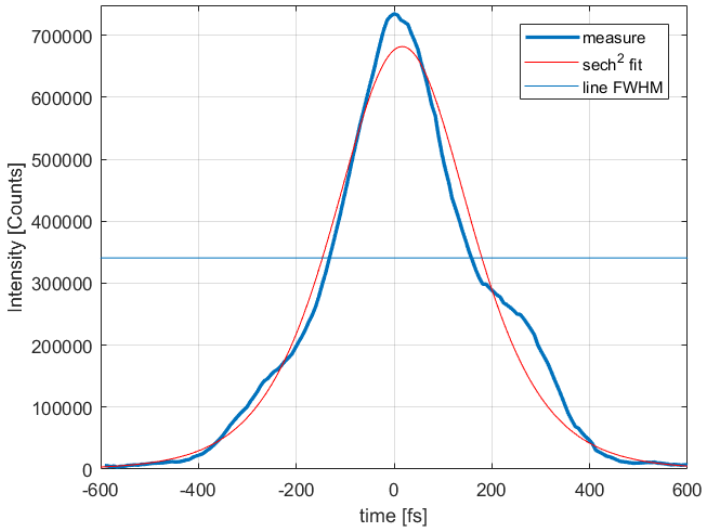

Figure 5.18: Intensity autocorrelation of the WLG (blue curve). Fitting of the curve with a sech^2 (red curve) and calculation of the duration of the pulse as the FWHM (light blue line) of the curve which is 203.9 fs.

5.3 Vertical microscope

Fig. 5.19 shows the microscope we have realized in our experimental setup. The red arrow shows the direction of propagation of the two beams in the microscope. The pump and the Stokes beam which arrive at the microscope are such that they are identically polarized and spatially and temporally synchronized. By means of an HR mirror and a mirror placed at 45°, the two beams are sent in the vertical microscope, the two pinholes shown in Fig. 5.19 are meant to allign the two beams before their arrival onto the sample. The illumination of the sample is guaranteed by an optical objective (M = 20x, NA = 0.3) and after the sample stage, placed on a x-y-z translational stage, another objective,identical to the first one, is used to collect the transmitted light. The sample is positioned such that the two beams form a focus in correspondence of it. Other two 45° HR mirrors are used to guide the beam onto the optical table to send it towards the CARS and SRS detection chains.
A dichroic mirror (DMLP1000), whose characteristic transmittance and reflectance curve are reported in Fig. 5.20, is used to separate the CARS signal from the Stokes and the pump, in a way such that one can analyze separately the CARS signal and contemporarily perform measurements of the SRG signal.

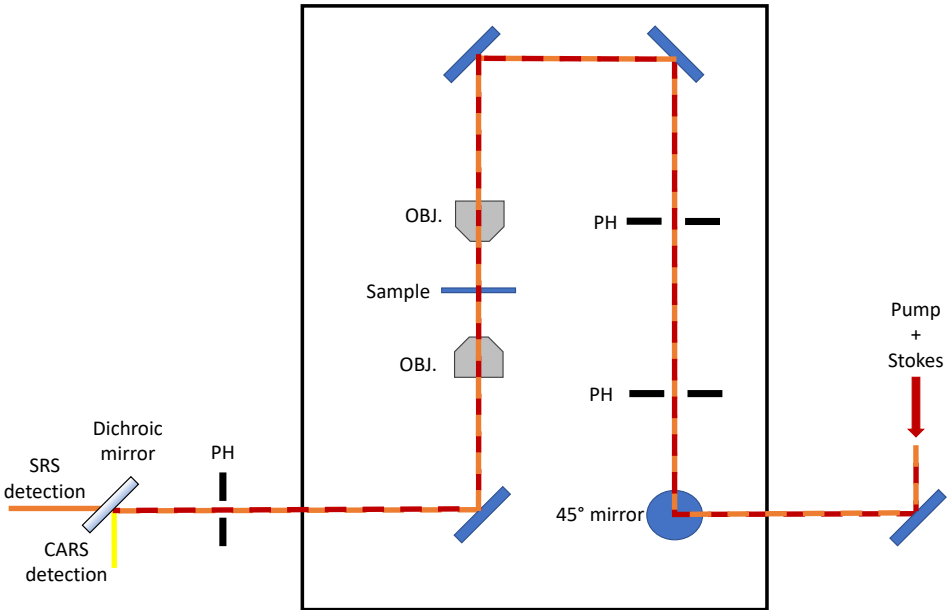

Figure 5.19: Scheme of the home-made vertical microscope. PH, pinhole; OBJ., objective. The red arrow indicates the direction of propagation of the two beams (pump in red and Stokes in orange).

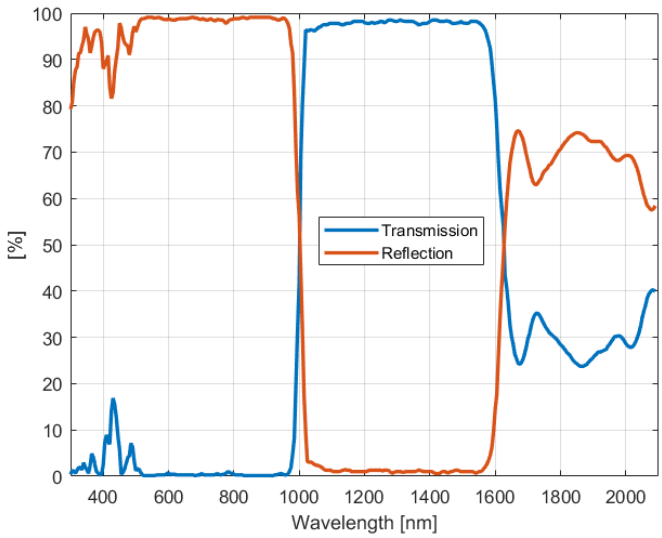

Figure 5.20: Transmittance and reflectance of the dichroic mirror long pass 1000 nm - DMLP1000 Thorlabs. Adapted from [55]

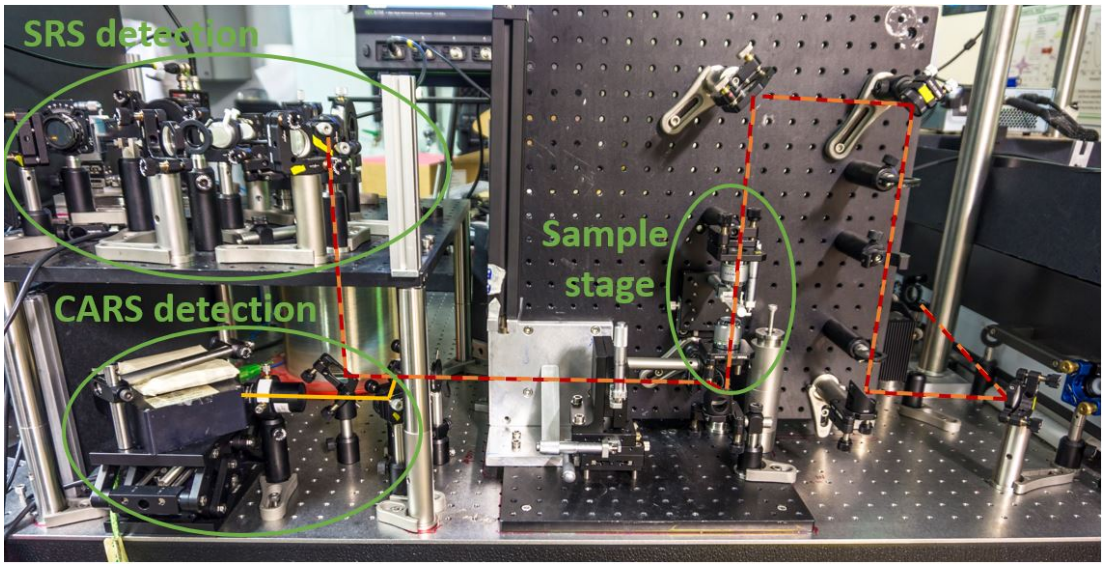

Figure 5.21: Picture of the vertical microscope, highlighting the sample stage and the CARS and SRS detection optical chains. The red and orange lines represent the pump and Stokes beam, respectively. The yellow line represents the CARS signal which is reflected by the DMLP1000 and sent to a spectrometer for CARS detection. The DMLP1000 transmits the Pump and Stokes signal. In the SRS detection stage, the pump is removed by means of a FELH1050 to maintain on the upper stage only the Stokes beam.

5.4 Cars detection

This section deals with the CARS detection chain that has been implemented to detect the broadband CARS signal. The main problem of CARS microscopy is the presence of the NRB, which may distort the resonant contribution coming from the sample. In particular, the single-frequency CARS microscopy works very well in the C-H stretching region where the resonant contribution is predominant with respect to the non-resonant background and so it can be used for imaging of lipids and studying their metabolism. Instead, for the fingerprint region, the NRB makes difficult to distinguish the resonant signal coming from the sample. In the broadband case, and in particular for the case of multiplex CARS, the resonant signal is still mixed with the NRB, but in this case the NRB is not as detrimental as in the single-frequency configuration. Indeed, on the one hand the NRB acts as a local oscillator, intrinsically phase locked to the nonlinear CARS signal, that allows its heterodyne amplification. On the other hand, the availability of the complete CARS spectrum enables to apply analytic techniques to retrieve the spectral phase [11].

The CARS detection chain we have realized is shown schematically in Fig. 5.22. The dichroic mirror (DMLP1000) reflects the portion of the spectrum below 1000 nm which is sent towards a spectrometer (Ocean Optics, HR2000). A series of filters FESH1050 suppresses the remaining components above 1050 nm, in a way such that the Stokes is completely filtered and the spectrometer is not saturated. A short-focal length (f = 2.5 cm) plano-convex lens is used to make the beam

to form a focus in correspondence of the grating of the spectrometer, where the spectrum of the CARS signal is detected.

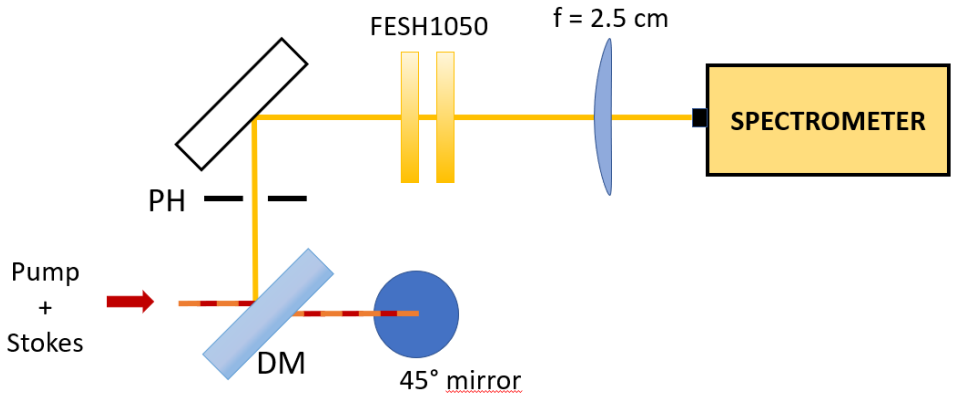

Figure 5.22: Schematic of the CARS detection stage. PH, pinhole; DM, dichroic mirror. The red arrow indicates the direction of propagation of the two beams (pump in red and Stokes in orange). In yellow the CARS signal that is delivered towards the spectrometer (Ocean Optics, HR2000).

5.4.1 Results

The CARS detection optical chain has been tested with two different solvents: acetone (C_3H_6O) and ethanol (C_2H_5OH). After placing the sample (*cuvette* + solvent) on the x-y-z stage, we have properly synchronized the two beams in time, by moving the delay line on the pump beam path, and in space by playing with the combiner, in a way such that the two beams arrives contemporarily and illuminate the same portion of the sample. The z-position of the *cuvette* has been set in order to be certain that the focus of the two beam is on the solvent and not on the *cuvette*. The WLG light has been attenuated such that one avoid to create other no-desired nonlinear effect on the sample. Indeed, we have noticed that by using all the power of the WLG (100 mW) the spectrum read by the spectrometer on the CARS detection chain shows the appearance of a residual supercontinuum light which could be due or to the residual WLG below 1000 nm which is not filtered by the filters placed before the detection stage or other white light generated by the intense beam on the sample. In any case, it is important to emphasize that the introduction of attenuators on the WLG stage has to be taken into consideration when temporally synchronizing the two beams, since the optical path of the Stokes beam gets longer. Soon after the sample, the second objective is placed in a way such that the beam remains collimated for a very long distance.
Fig. 5.23 shows the Raman spectrum of acetone we have acquired with our setup. The graph shows the spectrum in function of the wavenumber in cm^{-1} (bottom x-axis) or in function of the wavelength in nm (top x-axis). The positions of the peaks of acetone have been highlighted in the graph. By comparing this spectrum

with the one in Fig.5.24 [57], we notice that the main peaks of acetone which are the one at 790 cm^{-1} (CC stretching), 1078 cm^{-1} (CH_3 rocking), 1234 cm^{-1} (CH_3 s-deformation) and at 1440 cm^{-1} (CH_3 d-deformation) are present also in the spectrum we have acquired with a small shift of the peaks with respect to their position. Moreover, we see also the peaks below 790 cm^{-1}, that are in our case at 433 cm^{-1} and at 598 cm^{-1} (CCC deformation), which are shifted with respect to their actual position. Eventually we see also the peaks at higher wavenumber which are the one at 1706 cm^{-1} (CO stretching) and the one at 2931 cm^{-1}. This last peak is reported also in literature [58] and is due to the CH_3 stretching of acetone. The fact we measure this peak is in agreement with what has been discussed in section 5.2, the broadband Stokes allows us to detect a wide portion of the Raman spectrum ($138 - 2995$ cm^{-1}), including the fingerprint region and the high wavenumber region associated to the vibration of the hydrogen bonds. Note that respect to the Raman spectrum shown in Fig.5.24, the spectrum reported in Fig.5.23 is immersed in the Four-wave-mixing (FWM) signal, present because of the high power of the pump and of the Stokes impinging on the sample ($P_{pump} = 50$ mW, $P_{Stokes} = 50$ mW). Moreover, the FWM is predominant in the region of the spectrum corresponding to the most intense part of the Stokes
Eventually it is also possible to estimate the resolution we can have in the Raman spectrum. We expect the resolution is related to the spectral width of the narrower pulse that illuminates the sample, in our case the pump. In section 5.1 we have seen that the spectral width of the pump is 1.45 nm corresponding to 13 cm^{-1} . By looking at the most intense peak of the Raman spectrum of acetone, that is the one at 790 cm^{-1}, we notice that the resolution is ≈ 34 cm^{-1}.

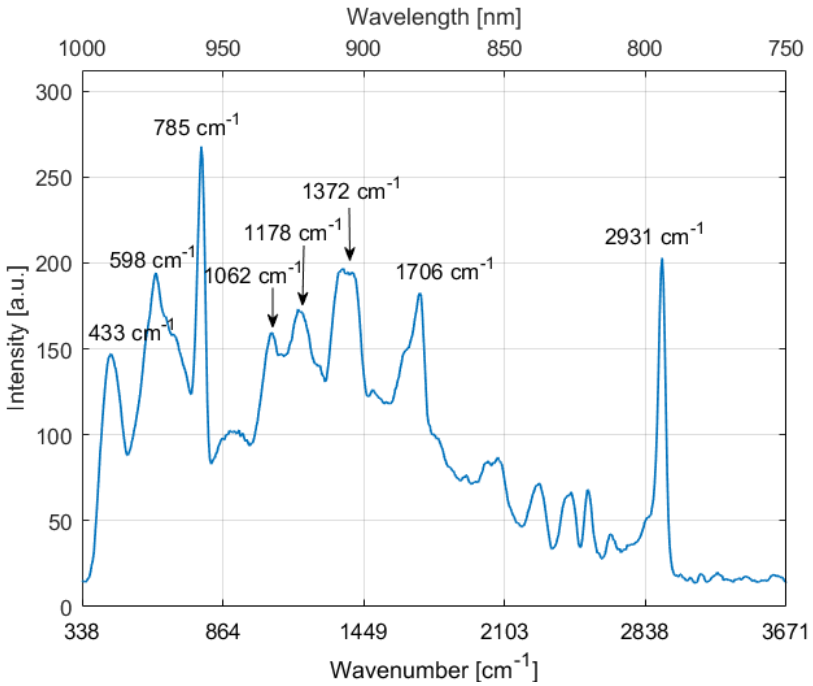

Figure 5.23: Raman spectrum of the acetone acquired with the CARS detetction chain.

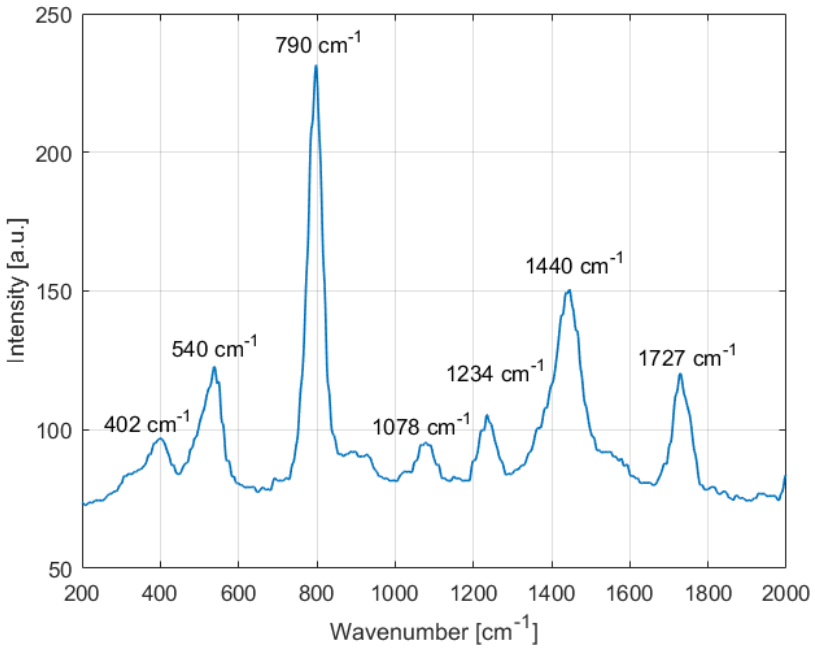

Figure 5.24: Raman spectrum of the acetone taken from literature. Adapted from [57].

Fig.5.25 shows the CARS spectrum of ethanol. Also for the case of ethanol, there is a good agreement between the spectrum we have acquired and the one present in literature, in Fig.5.26 [49]. Indeed, in our spectrum the most intense peak is the one at 878 cm^{-1} (C-C stretching) as in the reference spectrum. Then one can identify all the peaks at higher wavenumber, that is the couple of peaks at 1048 cm^{-1} and at 1090 cm^{-1} (CO stretching), then the peak at 1248 cm^{-1} and the one at 1447 cm^{-1} (C=C stretching). The peak at lower wavenumber (431 cm^{-1}) in our spectrum is immersed in the FWM signal, therefore it is hard to reveal it. Indeed, in Fig. 5.25, before the main peak at 878 cm^{-1} there are two peaks probably due to FWM at 518 cm^{-1} and at 665 cm^{-1}, not present in the Raman spectrum of ethanol taken as reference. Moreover, thanks to the broadband Stokes arriving till 1500 nm, it is possible to reveal the peaks in the high wavenumber window, correspondent to the CH_3 bonds of ethanol. In particular, we see 4 peaks at 2712 cm^{-1}, 2885 cm^{-1}, 2940 cm^{-1} and at 2988 cm^{-1}. These peaks are slightly shifted with respect to the one shown in Fig. 5.26, but there is a good agreement as regard the intensity of the Raman signal corrispondent to the four different vibrational transition. Also for this case, one can estimate the resolution the CARS spectroscopy allows one to reach referring to the FWHM of the main peak of ethanol which is the one at 878 cm^{-1}. In this case the resolution is 50 cm^{-1}.

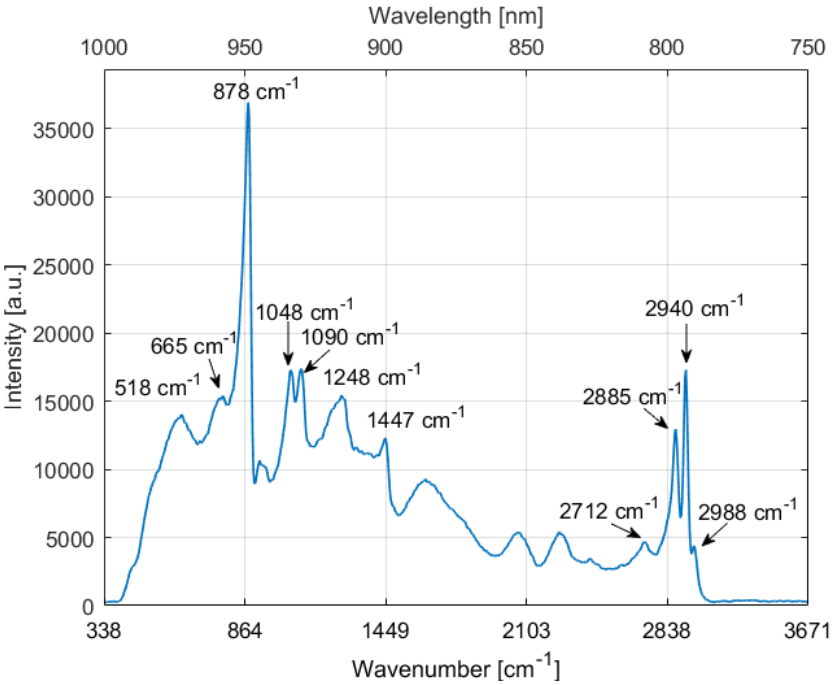

Figure 5.25: Raman spectrum of the ethanol acquired with the CARS detection chain.

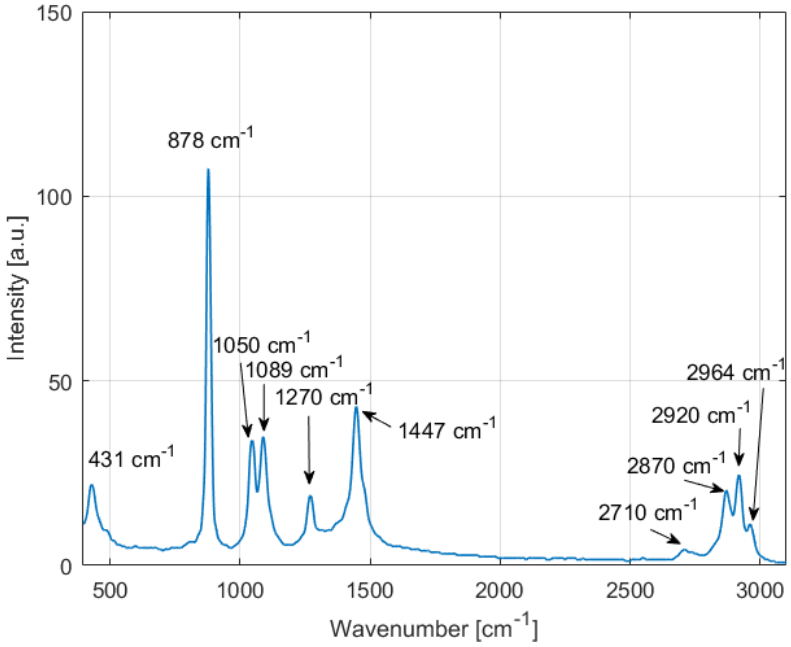

Figure 5.26: Raman spectrum of the ethanol taken from literature. Adapted from [49]

.

5.5 SRS detection

This section deals with the two different detection stages have been implemented for multiplex SRS (see Fig.5.27). The most widely spread approach to broadband CRS is a serial spectral acquisition approach (hyperspectral CRS), in which the sample is raster scanned at every single frequency detuning frame by frame or line by line, obtaining a stack of single-frequency images which can be presented as a multi-spectral data set. The biggest limitation of hyperspectral CRS is that the broader is the Raman spectrum to be analyzed the longer will be the acquisition time. Moreover, Hyperspectral CRS implies the *a priori* knowledge of the Raman resonances of the sample to investigate. An alternative to this serial spectral detection is the parallel spectral detection, this technique is known as multiplex CRS. With respect to multiplex CARS, where only photon counting is enough to retrieve the signal, multiplex SRS requires more sophisticated instrumentation (i.e. lock-in amplifiers) to detect the SRG signal from the huge background. One possible way to do multiplex SRS is implemented by multiplexing the single detector and single channel-lock-in amplifier with a certain amount of detectors and lock-in amplifiers proportional to the spectral bandwidth dimension to be detected. It is evident that such a system due to the complexity of the electronics needed is difficult to be realized. Moreover the spectral resolution is limited by the high number of detectors that can be integrated in the platform. We will present in the following two novel techniques which relies on a simple setup which uses a single photodiode detection and guarantees broadband spectral coverage and high spectral resolution: Photonic Time Stretch SRS (PTS-SRS) and Fourier Transform SRS (FT-SRS).

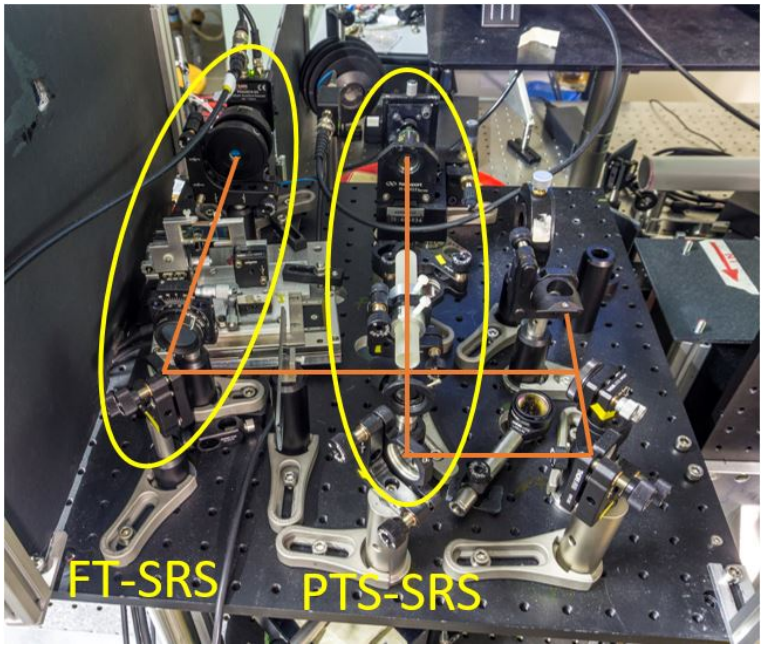

Figure 5.27: Picture of the SRS detection stage. The orange line corresponds to the Stokes beam which could go, through a flip mirror, in the FT-SRS detection stage or in the PTS-SRS detection stage.

5.6 PTS-SRS detection stage

Photons time stretch SRS (PTS-SRS) combines the time stretch dispersive Fourier transform (TS-DFT) with stimulated Raman scattering in order to measure single-shot SRG broadband spectra. In PTS-SRS the modulated narrowband pump and the broadband Stokes interact with the sample,then the broadband Stokes at 2 MHz repetition rate is stretched in time in a non-zero dispersion shifted single-mode fiber, eventually the signal is read by a fast photodiode.
Fig.5.28 shows the PTS-SRS detection stage we have implemented in our setup.

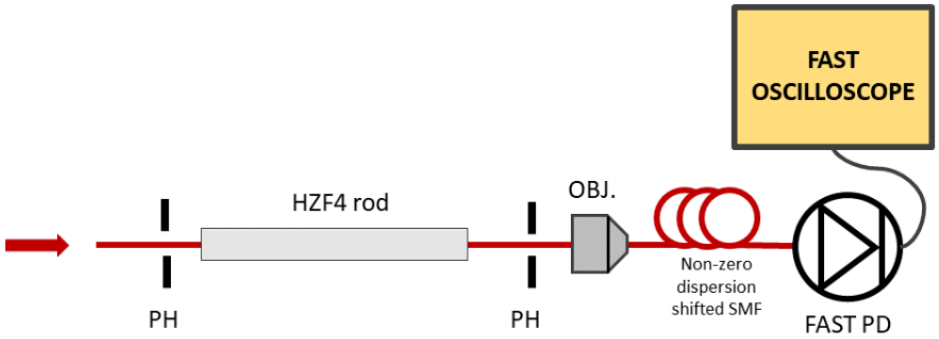

Figure 5.28: Schematic of the PTS-SRS detection stage. PH, pinhole; OBJ., objective; FAST PD, fast photodiode; SMF, single-mode fiber. The red arrow indicates the direction of propagation of the beam (red line).

After the interaction with the sample, the two beams (modulated pump and Stokes) are separated from the CARS signal by a dichroic mirror (see Fig.5.22). The white light generation signal which contains the SRG information, goes into a H-ZF4 rod to stretch the pulse before entering the optical fiber. This process is necessary to prevent nonlinear effect due to the high peak power of the pulse into the optical fiber, thus avoiding strange modulation of the pulse. The signal is than read by a fast photodiode (DET08CFC/M-5 GHz, InGaAs) and sent to a fast oscilloscope (Teledyne Le Croy HDO6104) with 1 GHZ bandwidth, 2.5 GS/s sampling rate and high resolution (12-bit digitization).
The choice of the rod has been done by performing proper calculation of the pulse duration after the rod, in order to choose the material and also the length of the glass. We have done calculation on two different glasses ZF_2 and H-ZF4. Both glasses were a valid choices for our purposes, but in the end we have chosen the second one. Calculation on the refractive index of the H-ZF4 and on its dispersive properties are reported in Fig.5.29. By inserting the coefficient reported in Fig. 5.30 in the Sellmeier equation:

$$n^2 = A_0 + A_1\lambda^2 + A_2\lambda^{-2} + A_3\lambda^{-4} + A_4\lambda^{-6} + A_5\lambda^{-8} + ... \qquad (5.11)$$

where λ is the wavelength expressed in μm, it is possible to derive the refractive index behaviour of the H-ZF4.

Fig. 5.29 reports the refractive index of the glass and its second derative $d^2n/d\lambda^2$ in function of the wavelength. The second derivative is necessary to calculate the pulse duration after the rod as we have seen in Chapter 3. Considering a variable length, the pulse duration is plotted in Fig. 5.31.

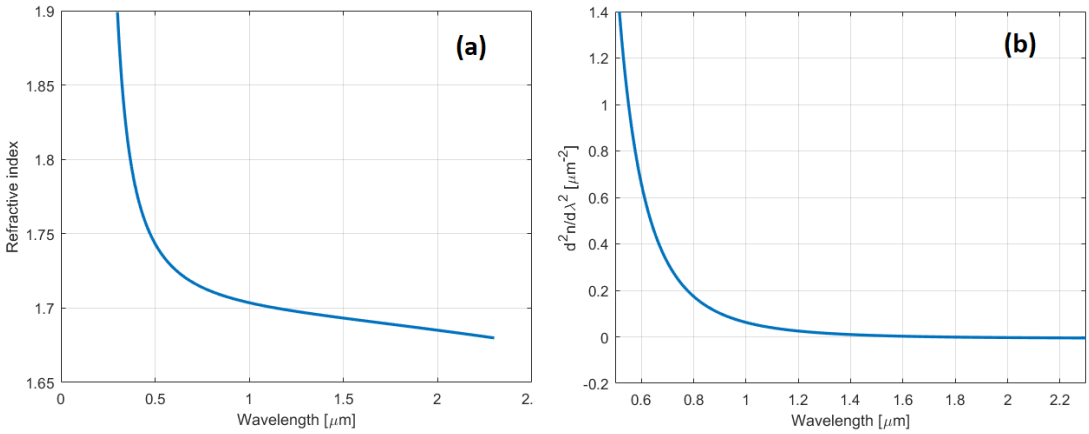

Figure 5.29: a) Refractive index of the H-ZF4 rod in function of the wavelength [μm]; b) Second derivative of the refractive index with respect to the wavelength.

Constants of Dispersion Formula	
A_0	2.87833860E+00
A_1	-1.18585043E-02
A_2	3.41292688E-02
A_3	1.67815401E-03
A_4	-5.56455694E-05
A_5	1.43620134E-05

Figure 5.30: Coefficients for the determination of the refractive index of H-ZF4.

For our purposes, a length of the crystal of 10 cm is sufficient, since it guarantees a pulse duration after the propagation into the rod of the order of 1 ps ($GDD_{HZF4} \approx 9 \cdot 10^3$ fs^2 at 1100 nm). Measurements of the pulse duration of the WLG after rod have been done using the SHG-FROG setup. The FROG trace has been obtained by scanning the motorized delay line from -2800 fs to 2800 fs is reported in Fig.5.32 and acquiring 601 spectra. The correspondent intensity autocorrelation, we have extrapulated from this FROG map, is shown in Fig.5.33.
Using the same procedure we have seen before, it is possible to retrieve the pulse duration from the FWHM of the intensity autocorrelation, properly fitted using the square of an hyperbolic secant function. For this pulse, a pulse duration of $\Delta t_{pulse} = 793 fs$ has been obtained.

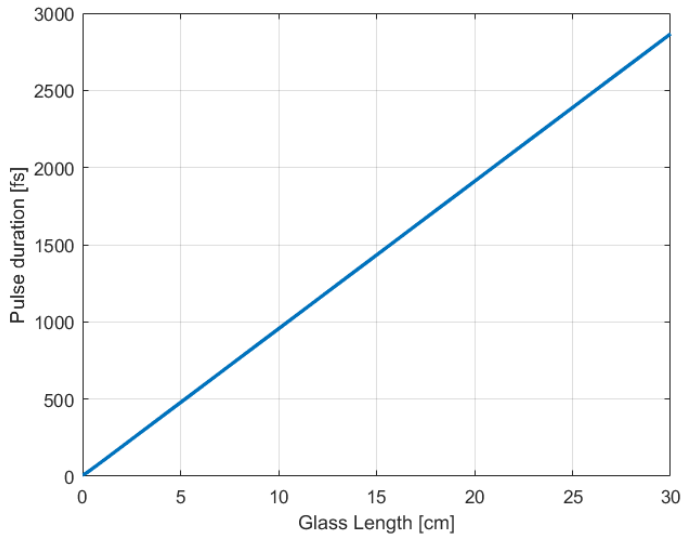

Figure 5.31: Pulse duration after the propagation in a rod of HZF4 in function of the rod length.

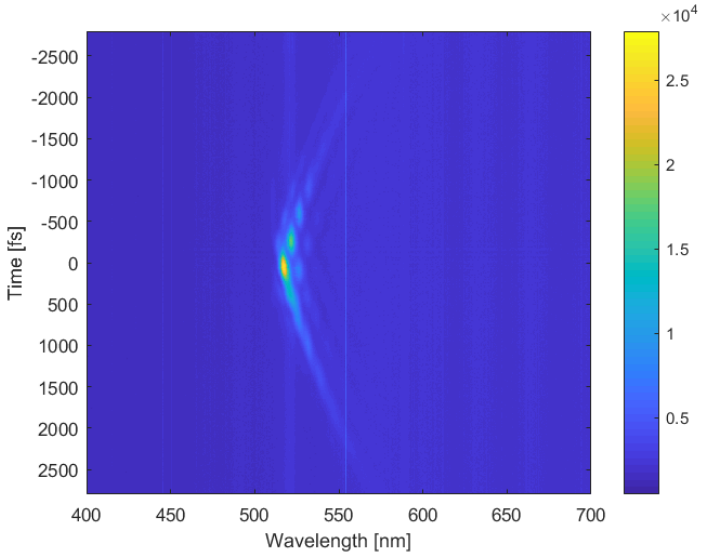

Figure 5.32: Frog trace for the WLG after the rod obtained by scanning the motorized translational stage from -2800 to 2800 fs and acquiring 601 spectra. The colorbar represents the intensity of the beam in terms of counts.

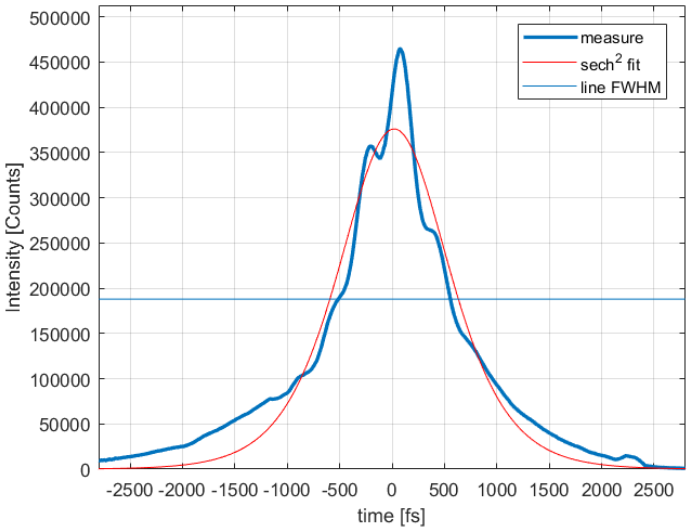

Figure 5.33: Intensity autocorrelation of the WLG after the rod (blue curve). Fitting of the curve with a $sech^2$ (red curve) and calculation of the duration of the pulse as the FWHM (light blue line) of the curve which is 793 fs.

After the rod stage, the beam is centered onto an objective (Melles Griot Microscope 160/0.17F 25/0.5 Objective Lens) and then enters into the non-zero dispersion shifted single-mode fiber. The signal is then acquired by using a fast oscilloscope (Teledyne Le Croy, HDO 6104). The SM fiber in the spectral region of the Stokes has a negative dispersion parameter D. The fiber has at 1550 nm a $D = -4$ ps/(nm·km) and a dispersion slope at ZDW of 12ps/(nm^2·km) (see Fig. 3.3). It means that it introduces normal dispersion, hence in the oscilloscope the pulse has the red-shifted components that arrive earlier, while the blue-shifted ones arrive later.

5.6.1 Calibration procedure of the SM fiber

The calibration of the optical fiber is depicted in Fig. 5.34. In order to calibrate the fiber and associate to each wavelength a proper arrival time, it has been necessary to use four interferential filters positioned before the objective. The filters at 1064 nm, 1100 nm, 1200 nm and 1300 nm allow one to establish the arrival time of these four colours. The calibration curve is then obtained fitting the four points with a polynomial curve of order two. The temporal traces of the trigger of the laser and of the four components, measured via the 12-bit 1-GHz oscilloscope (Teledyne Le Croy, HDO 6104), are represented in Fig.5.35. The duration of each pulse of the supercontinuum light is $\approx$ 16 ns, corresponding to 40 samples per pulse at 2.5 GSamples/s. The alignment of the pulse temporal traces is crucial in order to calculate the arrival time of each single wavelength. A reference signal to trigger the oscilloscope would guarantee that all the pulses are sampled at same time points and so that the measurements of the different colours are coherent between them. As a reference signal the trigger of the laser has been used and the zero of the temporal axis has been fixed on the rising

edge of the laser trigger. Notice that the pulse that arrives at the output of the fiber is synchronized with a trigger pulse which is not the one we have chosen for establishing the zero of the temporal axis. Indeed, the propagation velocity in the fiber can be calculated as $v = c/n_{\text{core}}$, where $n_{\text{core}} \approx 1.4492$ is the refractive index of the core of the single-mode fiber at 1100 nm. Assuming that in the range of wavelengths of the WLG, the refractive index does not change too much, $v = 2.07 \cdot 10^8$ m/s. The time taken by a pulse to propagate in $L = 3$ Km of the fiber is $\Delta t = v \cdot L \approx 14.5\mu$s. The pulse repetition period of the laser at 2 MHz is 0.5 μs, then when the pulses arrive at the end of the fiber it corresponds to the 29^{th} pulses of the laser after the one chosen to trigger the oscilloscope. Despite that, we have checked that there are not problem in choosing the trigger of the laser as reference signal, since the jitter is very low and does not compromise the precision of the calibration.

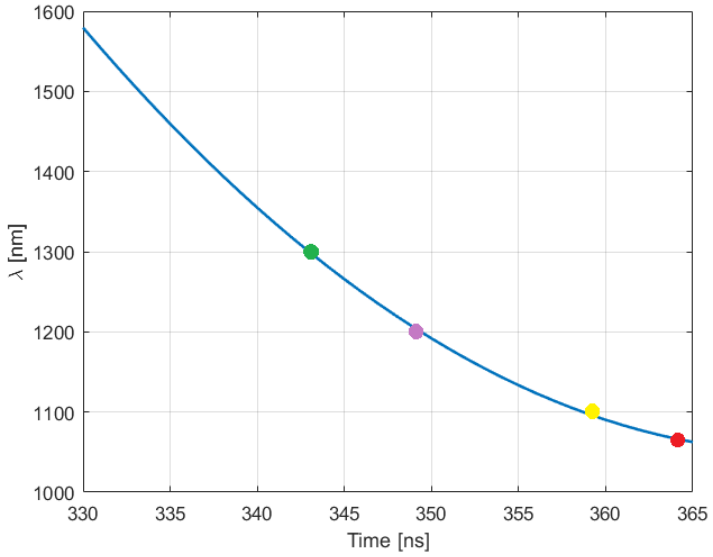

Figure 5.34: Calibration curve representing the arrival time of the different wavelengths after the propagation in the fiber.

The calibration procedure allows one to obtain a time-to-wavelength mapping, which is fundamental for measuring the SRG signal with PTS-SRS. Indeed, by means of the oscilloscope the Stokes pulse is read as a function of time. The calibration curve is used to transpose the pulse trace as a function of time in a pulse trace as a function of the wavelength. To measure the SRG signal, a sequence of N pulses is acquired. This sequence is reshaped such that the two adjacent pulses, correspondent to the Stokes pulse with pump ON and with pump OFF, are subtracted and the resulting spectrum is normalized, dividing it by the Stokes spectrum with pump OFF. The overall SRG signal, measured as $\Delta I_s/I_s$, is then obtained by averaging the N/2 signals.
Same experiment has been done by Saltarelli et al. [38] using a 80 kHz Yb laser at 1026 nm and 8 cm^{-1} bandwidth as pump beam. The Stokes beam is a ≈50 nm FWHM bandwidth tunable in the 1420-1540 nm range, covering a frequency detuning of ≈400 cm^{-1} in the 2700-3250 cm^{-1} region, enabling full coverage of

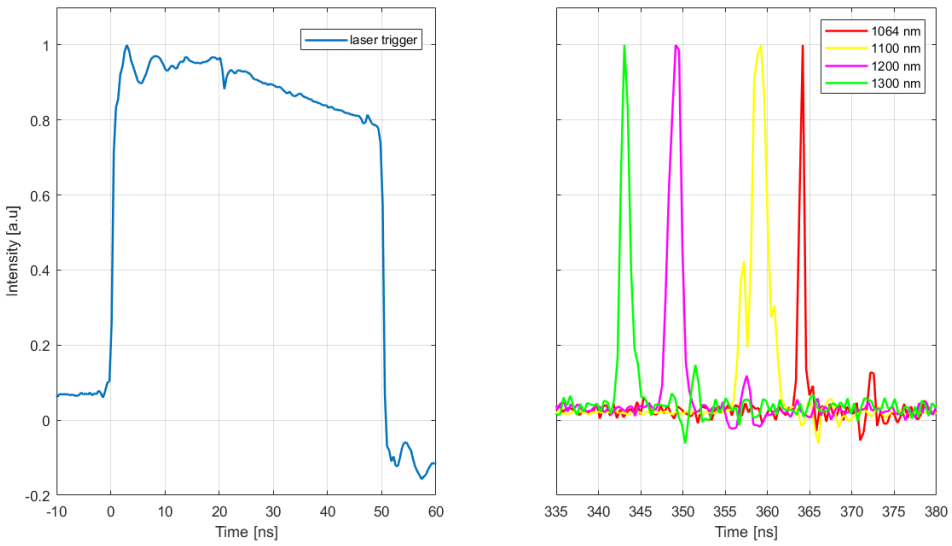

Figure 5.35: Data acquisition of the trigger and of the (normalized) pulses at 1064 nm (red) , 1100 nm (yellow), 1200 nm (violet), 1300 nm (green) through the fast oscilloscope after the propagation into the optical fiber. The plot has been separated to clearly distinguish the 4 different colours on the temporal axis which is the same for all the traces.

the C-H stretching band. In our case, we aim in investigating the fingerprint region of molecules, whose lines are associated to the stretching or deformation of carbon atoms bonded with hydrogen, nitrogen as well as other carbon atoms. The importance of the fingerprint region is that each different compound produces a different pattern of peaks in this part of the spectrum, enabling one to distinguish which compounds characterize a given sample. We will exploit PTS-SRS detection, with its unique capability to measure single-shot spectra at high repetition rates at a fast acquisition speed, to acquire spectra in the fingerprint region and in future to perform high-speed coherent Raman imaging of samples with their entire vibrational signature.

5.7 FT-SRS detection stage

FT-SRS is a technique which exploits a time-domain Fourier-transform detection system to have access to broadband coverage of the stimulated Raman gain spectrum [48]. It makes use of a passive biregringent interferometer in the detection chain that generates two phase-locked replicas of the Stokes and permits to retrieve the Stokes and the SRG spectra using the FT technique. This approach is extremely powerful because of the simplicity of the setup, since the retrieval of the SRG signal does not requires many detectors and a multi-channel lock-in amplifier, as it common for multiplex SRS, but it use a single pixel detector and a commercially available high-sensitivity single-channel lock-in amplifier, guaranteeing a broad spectral coverage and high spectral resolution of the FT spectroscopy.
The experimental setup we have implemented for broadband FT-SRS is sketched in Fig. 5.36. The narrowband pump (modulated at 1 MHz) and the broadband Stokes are temporally and spatially synchronised and collinearly are focused into the sample. After the sample, the pump is filtered out using a long-pass filter and the broadband Stokes is sent to a common-path birefringent interferometer. The advantage of using such an interferometer is that with respect to the Michelson interferometer, where the two replicas of the pulse undergo different paths, in a common-path birefringent interferometer the noise related to mechanical vibrations is reduced due to the fact that both the replicas travel the same optical path, thus experiencing the same mechanical vibration and maintaining the same phase relation during all the optical path. This results in attosecond control of the delay between the two pulses, which grants a precise reconstruction of the interferogram that oscillates at the optical carrier frequency.

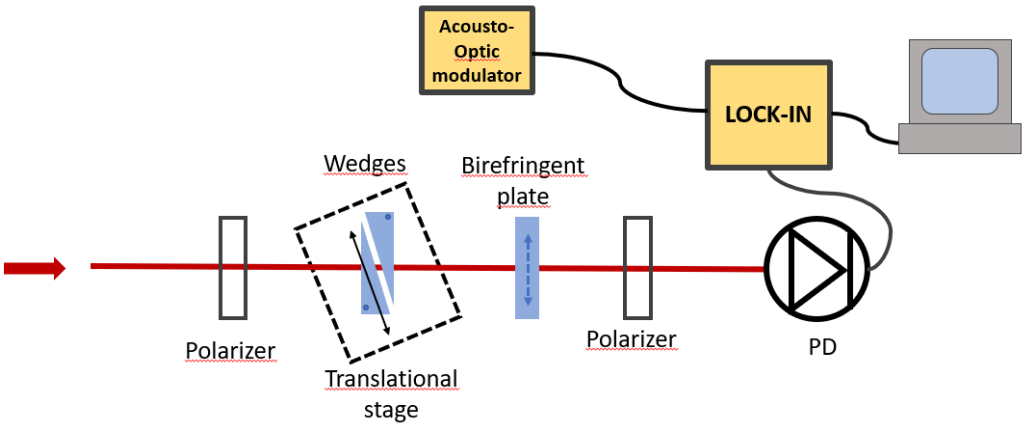

Figure 5.36: Schematic of the FT-SRS detection stage. FAST PD, fast photodiode. The red arrow indicates the direction of propagation of the beam (red line).

In Fig.5.36, the common-path birefringent interferometer is realized using a first polarizer which projects the pulse with 45° polarization with respect to the fast axis (n_o) of the birefringent material of the two wedges of Yttrium orthovanadate (YVO4). YVO4, with respect to the other commonly used birefringent crystals,

is a positive uniaxial birefringent material, that is $n_e > n_o$; hence, the fast axis is the one correspondent to the ordinary refractive index. These wedges are inserted in the beam path in a way such that the face of the first wedge is orthogonal to the propagation direction of the beam. By means of a motorized translational stage (SMC Hydra CM 2 axis Motion controller), the first wedge is scanned along an axis parallel to the oblique face. The second wedge is positioned so that the two wedges constitute a plate with parallel outer faces and with variable thickness. When the pulse of the Stokes beam arrives on the first wedge, it splits its energy into two perpendicularly polarized components that collinearly propagate along the fast and the slow axis of the birefringent material. Due to the birefringence of the material (YVO4), the two orthogonally polarized replicas see a different refractive index (the ordinary group index n_o^g and the extraordinary group index n_e^g) and thus different group velocities (c_0/n_o^g and c_0/n_e^g respectively). The group velocity mismatch between the two replicas produces a relative time-delay τ between them which is controllable by varying the thickness L of the birefringent material in which the pulses are propagating ($\tau = L/c_0\,(n_o^g - n_e^g)$). The two orthogonal replicas then go into a birefringent plate of YVO4, which introduces a constant delay between the two replicas. The optical axis of this plate is perpendicular to the one of the wedges (see Fig.5.36), such that when the thickness of the wedges is the same of that of the birefringent plate the delay between the two replicas is zero. Such a delay can be varied around the delay-zero by properly tuning the two wedges, changing the overall thickness of the material in which the replicas propagate. A second polarizer projects the two replicas onto a common polarization state in order to make them interfere at the detector (PDA20CS-EC - InGaAs Switchable Gain Amplified Detector, Thorlabs). The interference pattern of the two replicas as a function of the delay between the two replicas is called interferogram. The output signal of the detector is sent to a data acquisition (DAQ) system, to record the Stokes interferogram, and to a lock-in amplifier, to measure the SRS interferogram. To reconstruct the SRG signal, which contains the vibrational information of the sample under analysis, is necessary to do the FT of the difference of the interferograms acquired with and without the pump. Thanks to the linearity of the FT operator, the difference between the FTs of two signals is equal to the FT of the difference of the two signals. In our case, the signals are the interferograms and their FTs are the corresponding spectra. We take advantage of this property, by first obtaining directly the difference of the two Stokes pulse interferograms using a lock-in amplifier. Indeed, the lock-in amplifier demodulates the Stokes signal, using the signal at 1 MHz coming from the AOM. The signal is sent to a computer to reveal the SRS interferogram and the corresponding SRG spectrum is obtained by Fourier transforming the SRS interferogram and diving it by the Stokes spectrum, obtained Fourier transforming the Stokes interferogram acquired with the DAQ.

The FT-SRS measurements are carried out translating the first wedge using the step-scan mode. Indeed, after each step of the motor, whose size can be arbitrarily changed via software, the value of the signal given by the interference of the two replicas is processed by the lock-in amplifier. This procedure requires a calibration of the absolute position axis which can be executed acquiring the interferogram

of a spectrally narrow signal like the one given by a CW Helium-Neon laser [35]. Indeed, the interferogram of a monochromatic light is a cosine function, that can be written as:

$$y_n = cos(a \cdot x_n) \tag{5.12}$$

where a is the cosine angular frequency and x_n is the generic interferometer position at the sampling step n. Conceptually, from the measured interferogram y_n of a monochromatic light it is possible to extract the true interferometer position x_n; the most accurate method is based on the Fourier transform approach. In fact, Eq.5.12 can be written as:

$$y_n = \frac{1}{2}e^{i(a \cdot x_n)} + \frac{1}{2}e^{-i(a \cdot x_n)} \tag{5.13}$$

By taking the Fourier transform of y_n and then inverse Fourier transforming only the spectrum at positive frequencies, one isolates the first exponential, obtaining the complex function:

$$\bar{y}_n = \frac{1}{2}e^{i(a \cdot x_n)} \tag{5.14}$$

in which the exact interferometer position x_n is proportional to the phase of y_n. To calibrate the wavelength axis of the spectrum is necessary to establish a correspondence between the inverse of the position of the motor in mm^{-1} and the wavelength in nm, indeed, between these two quantities there is no a linear relation. This calibration procedure has been executed using three different narrowband laser, the He-Ne at 632.8 nm, the Monaco at 1035 nm and a green diode at 530 nm.

5.7.1 Results

The FT-SRS detection stage has been tested on acetone and ethanol, contained in a 1mm-*cuvette*. Fig.5.37 reproduces the Stokes interferogram acquired sending the output signal of the detector to the ADC of the lock-in amplifier and removing the average value. Moreover, such an interferogram is obtained by scanning the position of the two wedges from 4.5 mm to 15 mm. Fig.5.37.a shows that the zero of the delay between the two replicas is at 5.3 mm. We chose to acquire only half of the interferogram, going from the zero of the delay to positive delay to have a better resolution on the reconstructed spectrum. Indeed, from theory [50], the resolution of a spectrum measured interferometrically depends on the maximum retardation of the scan. The greater the retardation, the higher the resolution. In order to remove the side-lobes of the Stokes interferogram, we apodized with the apodization function (orange curve) shown in Fig.5.37.a. The correspondent interferogram, we used to derive the Stokes spectrum, is the one in Fig.5.37.b. The spectrum of the Stokes signal, in Fig.5.38, is obtained by taking the absolute value of the Fourier transform of the interferogram. It shows a spectral range of the white light from 1050 nm to 1300 nm, corresponding to an SRS spectral coverage of $\approx$1800 cm^{-1}.
The SRS interferogram is shown in Fig.5.39. It is obtained by scanning the absolute position of the wedges for 10.5 mm and sending the output signal of

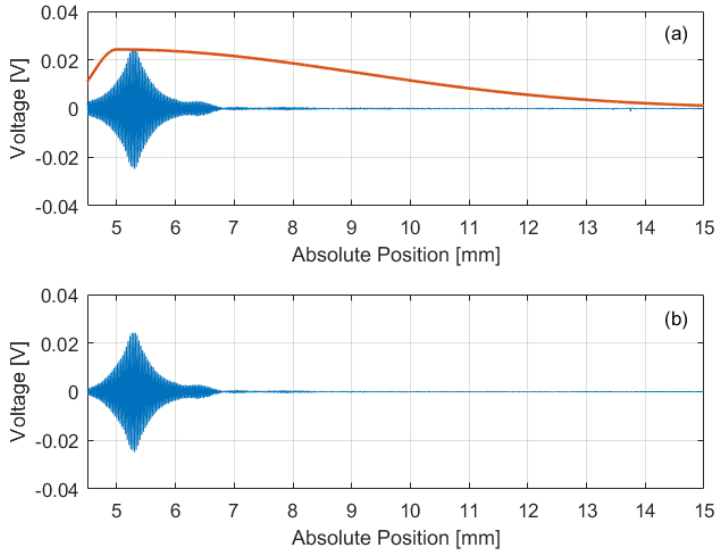

Figure 5.37: a) Stokes interferogram directly acquired from the ADC of the lock-in amplifier (blue curve) and apodization function used to apodize the interferogram (orange curve). b) Apodized Stokes interferogram, from which the corresponding Stokes spectrum has been rietrieved through Fourier transformation.

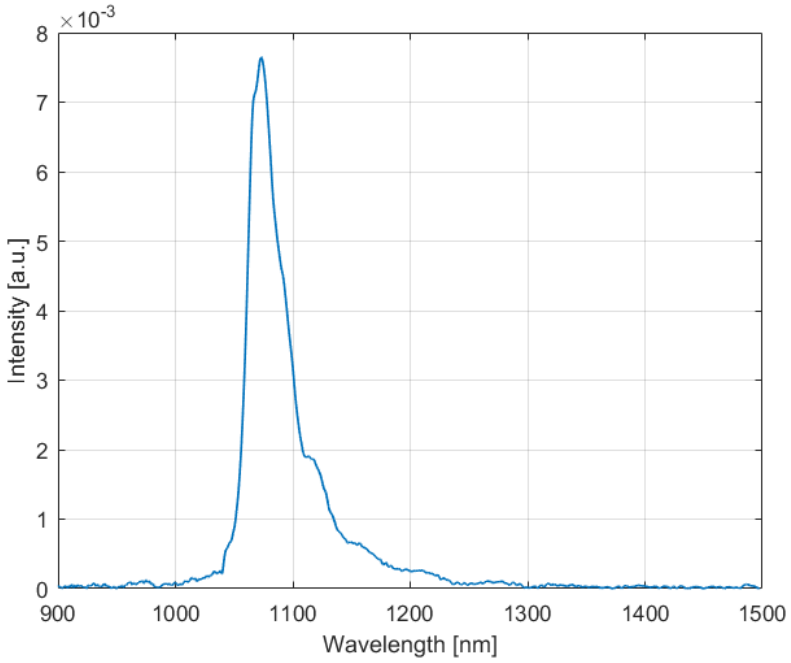

Figure 5.38: Spectrum of the Stokes pulse, obtained as the absolute value of the FT of Fig. 5.37.b

the detector to a lock in amplifier, which demodulates it using as demodulation function the signal coming from the AOM at 1 MHz. Fig.5.39.a shows the interferogram (blue curve) and also the apodization function (orange curve) which has been used to remove the side lobes from the interferogram [50]. In particular, we sent to zero the portion due to the Stokes which is the one at shorter delay, to minimize the noise contribution around the zero delay given by the Stokes Moreover, we suppressed also the portion at higher delay. The corresponding apodized interferogram is shown in Fig.5.39.b.
Taking the absolute value of the Fourier trasform of this apodized SRS interferogram and normalizing it with the Stokes spectrum in Fig.5.38, the resulting SRG signal is reported in Fig. 5.40. The SRG is calculated as $\Delta I_s/I_s$. Three clearly distinguishable peaks at 428, 529 and at 781 cm^{-1} are observed and addressed to the CCC deform and to the CC stretching of acetone. Moreover, a fourth peak at 201 cm^{-1} is present that could be associated to the torsion of acetone [58]. The lock-in integration time is set to 0.1 s. A 60 cm^{-1} resolution, limited by the delay range chosen for acquiring the data, is presented in the main peak of acetone at 781 cm^{-1}. It could be improved by further incresing the scanning of the absolute position of the two wedges. 50 mW of pump power and 100 mW of Stokes power reach the sample, limiting the maximum SRG signal to $1.5{\cdot}10^{-5}$.

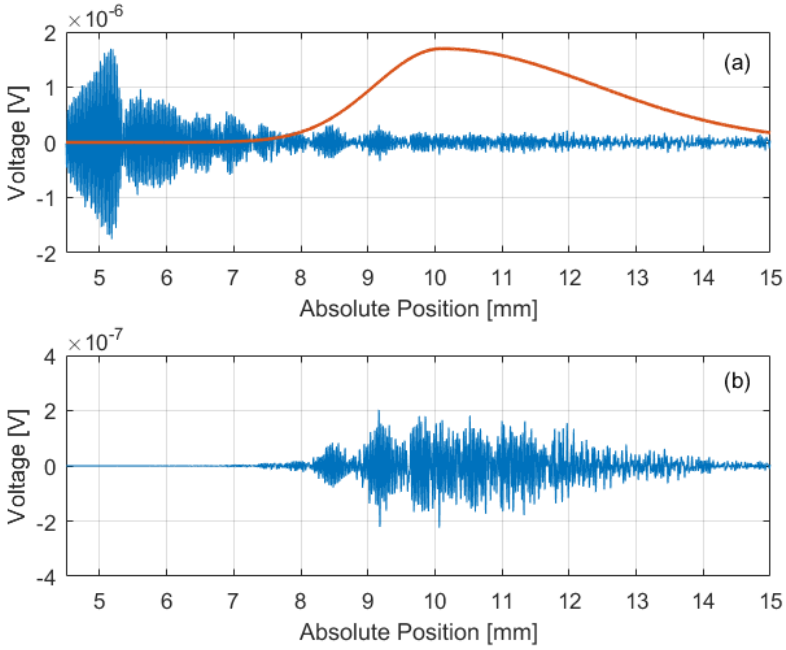

Figure 5.39: a) SRS interferogram of acetone from the output of the lock-in amplifier (blue curve) and apodization function used to apodize the interferogram (orange curve). b) Apodized SRS interferogram of acetone.

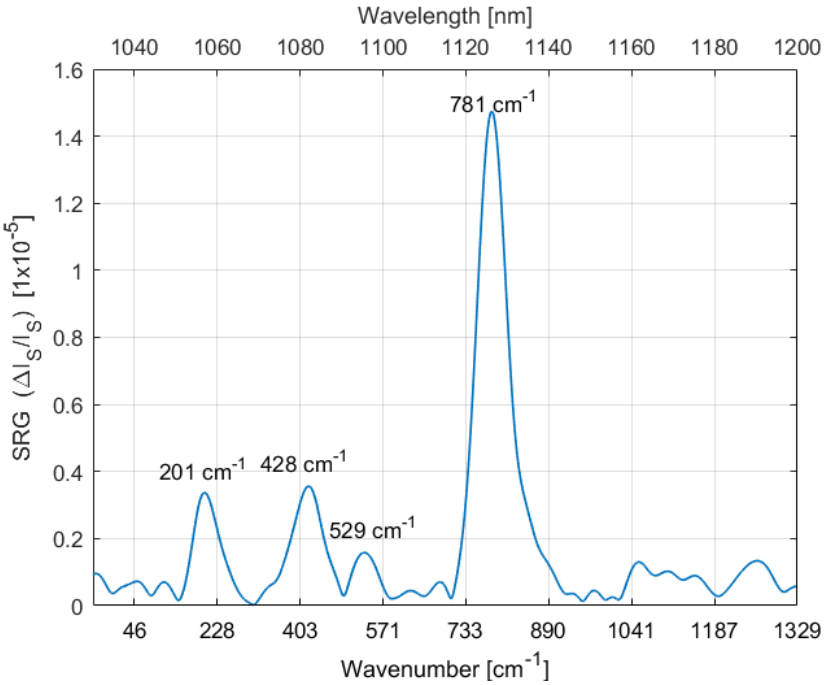

Figure 5.40: SRG spectrum of acetone obtained by normalizing the absolute value of the FT of Fig.5.39.b on the Stokes spectrum Fig.5.38.

Same procedure and same working conditions are adopted to retrieve the SRG signal of the ethanol, whose SRS interferogram is shown in Fig.5.41. The panel in Fig.5.41.a shows the interferogram acquired with the lock-in amplifier and the function (orange curve) used to apodize the interferogram. The apodized interferogram, used to retrieve the SRG signal is the one represented in Fig.5.41.b. The SRG signal is reported in Fig.5.42. The peak at 874 cm^{-1} corresponds to the main peak of ethanol in the fingerprint region associated to C-C stretching of ethanol. The peak at 537 cm^{-1} could corresponds to the peak of ethanol at lower wavenumber. Than three peaks at 1063, 1172 and 1363 cm^{-1} are distinguishable and they can be associated to the C=O stretching and to the C=C stretching of ethanol. Actually, these peaks do not perfectly match with the one presented in literature and reported in Fig.5.26. It could be due to the calibration of the wavelength axis, which can be improved by using as reference the known peaks of some test solvents or by measuring the Stokes pulse spectrum with a commercial spectrometer and compare it with the one obtained using the common-path birefringent interferometer. In this case a maximum SRG signal of $3.7 \cdot 10^{-5}$ has been detected, with a spectral resolution of 54 cm^{-1}.
These measurements on acetone and ethanol shows the first important results of our experimental activity. Indeed, we managed in acquiring SRG spectra in the fingerprint region, achieving a good agreement of the data with the one present in literature. The following steps of the FT-SRS stage consist in improving the resolution, by increasing the scan range of the wedges, and in adjusting the calibration of the wavelength axis, by using as reference the vibrational spectrum of some solvents.

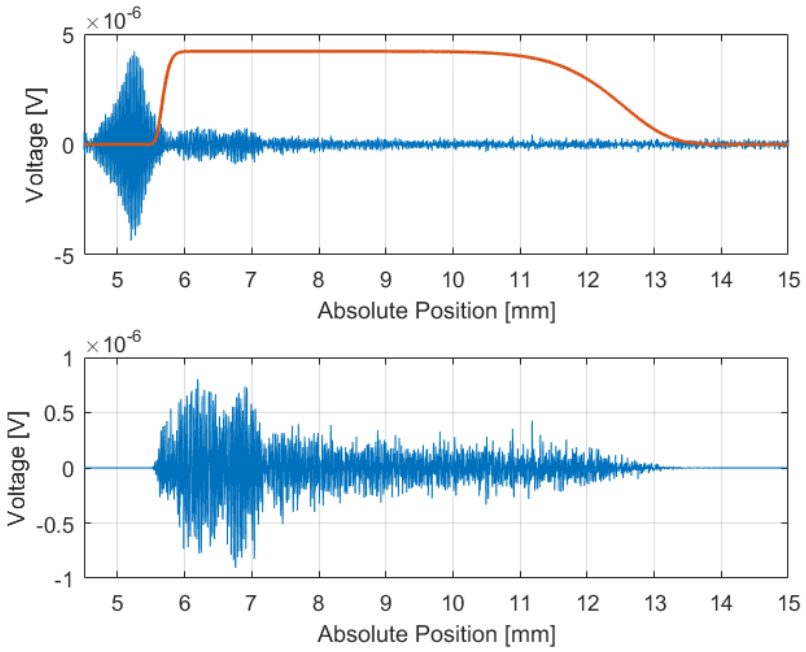

Figure 5.41: a) SRS interferogram of ethanol from the output of the lock-in amplifier (blue curve) and apodization function used to apodize the interferogram (orange curve). a) Apodized SRS interferogram of acetone.

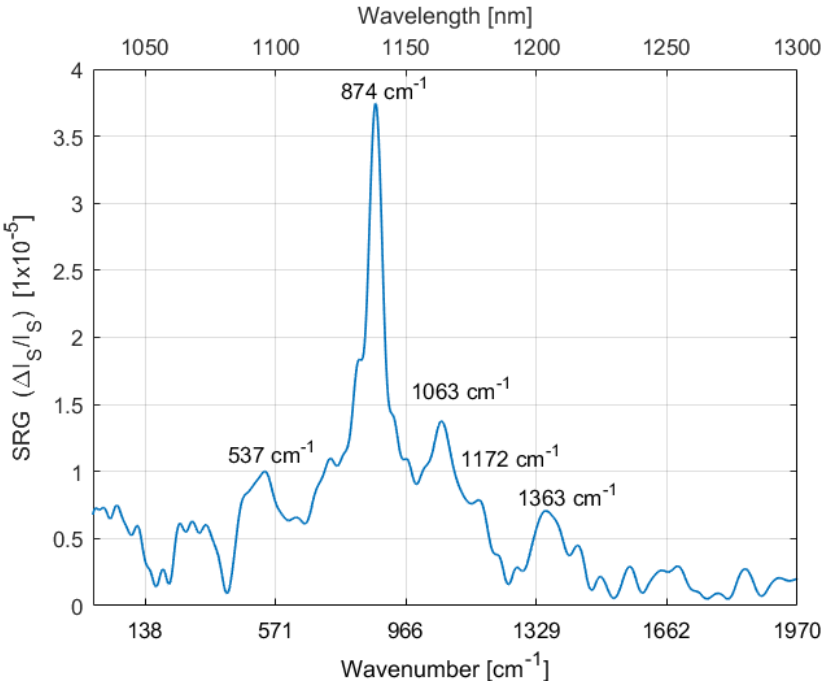

Figure 5.42: SRG spectrum of ethanol obtained by normalizing the absolute value of the FT of Fig.5.41.b on the Stokes spectrum Fig.5.38.

Chapter 6

Conclusions

This master thesis is focused on broadband Coherent Raman spectroscopy and microscopy. Broadband CRS microscopy has found mainly application in recovering the CARS signal, since it is in the anti-Stokes frequency region where no linear background is present, enabling direct signal detection by photon counting. Despite this advantage, CARS suffers from the so-called non-resonant background (NRB), that may strongly distort or even overwhelm the molecular vibrational spectrum of interest. Furthermore, since the CARS signal is homodyne detected, it scales quadratically with the number of oscillators in the focal volume, making it hard to perform quantitative measurements and to probe dilute species. SRS does not suffer from NRB and, since the signal is heterodyne detected, it inherently provides a linear dependence of the signal on the sample concentration but its extension to the broadband modality is technically challenging. This thesis describes two novel time-encoded implementations for broadband SRS, namely Photon Time Stretch SRS (PTS-SRS) and Fourier Transform SRS (FT-SRS).

More precisely, the thesis consists mainly in the design of the experimental setup for broadband Coherent Raman spectroscopy and microscopy, using as source a 60 W femtosecond laser, Coherent Monaco. The source is used to generate two beams, pump and Stokes, that are characterized in terms of sprectral content and temporal length using linear and nonlinear optical techniques. The pump spectral bandwidth has been narrowed using an etalon, obtaining a beam with $\approx$1.4 nm bandwidth, central wavelength at 1035 nm, average power of 50 mW and a duration of 1 ps. The Stokes beam has been produced through white light generation in a 6 mm-thick YAG crystal. This stage has constituted one of the most challenging part of the setup, expecially with respect to the temporal stability of the beam. Acting on all the degrees of freedom described in Chapter 5, we managed in generating a supercontinuum with rms = 0.5%, a spectrum spanning from 1050 nm to 1500 nm and average power of 100 mW. Such a wide spectral coverage allows us to probe the vibrational transition of the samples in the fingerprint region as well as in the high wavenumber region, corresponding to the stretching of the hydrogen bonds (C-H, N-H, O-H). The WLG has been characterized also in terms of the pulse duration, for which a duration of $\approx$200 fs has been measured. An home-made vertical microscope has been realized to easily insert the sample in the setup and adjust the collimation of the beam through the

objectives and the position of the sample. After the microscope, the CARS signal is measured through a spectrometer, while two time-encoded SRS techniques have been suitably implemented. The first time-encoded SRS implementation is PTS-SRS; it exploits the propagation of the Stokes beam into a non-zero dispersion shifted single mode fiber to stretch the pulse to a duration of few nanosecond, so that it can be sampled by a high-frequency ADC. A calibration procedure allows us to associate each point of the sampled temporal profile to a specific wavelength, using it for measuring single-shot spectra at 1 MHz repetition rate. The second time-encoded SRS implementation is FT-SRS; it is based on the propagation of the Stokes beam into a birefringent common-path interferometer, that creates two replicas of the pulse whose delay can be finely tuned. The signal read by the detector is sent to a lock-in amplifier which demodulates it at 1 MHz. The resulting SRS interferogram is then Fourier transformed thus obtaining the SRG signal.
The setup has been tested acquiring CARS spectra of some solvents. Comparing the spectra with those available in literature, we noted a good agreement with our measurements. Indeed, all the peaks are retrieved with a spectral resolution of 30-40 cm^{-1}. Nevertheless, the acquired spectra suffer the presence of FWM that is predominant for those peaks corresponding to the wavelengths around 1100 nm, where the Stokes beam is much more intense.
FT-SRS spectra of some solvents have been acquired, obtaining a good agreement with literature especially in the fingerprint region, with a maximum SRG signal of $1.5\text{-}3.7 \cdot 10^{-5}$ and a resolution of ≈ 54 cm^{-1}.
Further developments of the setup consist in adding in the vertical microscope a piezo-stage to perform xy-scanning of the sample, thus using the system for broadband CRS microscopy. This would allow the setup to perform imaging, exploiting the broad spectral coverage, the high power and high spectral resolution available.

Appendices

Appendix A

Relative intensity noise (RIN)

The output intensity of a laser shows power fluctuation due to intensity noise. The contribution of the intensity variations of the laser due to the total electrical noise at the receiver defines the relative intensity noise (RIN) [53]. The measurement of RIN serves as a quality indicator of laser devices. It can be thought of as a type of inverse carrier-to-noise-ratio measurement [52]. Therefore, the higher the RIN value, the more noisy the laser and a higher power penalty from RIN is induced. The RIN definition in linear form is as follows; we assume that RIN is white noise (constant for all frequencies). Moreover, for convenience, RIN is always normalized to a 1–Hz bandwidth, so that it becomes easier to compare the intensity fluctuations of the laser when receivers with different bandwidths are used [51]:

$$\mathrm{RIN_{Lin}} = \frac{< \partial P^2(t) >}{P_0^2 \cdot \Delta f} \ [1/\mathrm{Hz}] \tag{A.1}$$

where $\partial P(t)$ is the optical intensity fluctuations, the $< >$ denotes the time average, P_0 is the dc optical power, and Δf is the noise bandwidth (detection system bandwidth).
In dB unit, the RIN is the ratio of the laser noise power normalized to 1–Hz bandwidth, and the average (or d.c.) power of the photocurrent- both considered in electrical domain [51]:

$$\mathrm{RIN\,[dB/Hz]} = 10\log\left(\frac{< \partial P^2(t) >}{P_0^2}\right)[\mathrm{dB}] - 10\log\left(\Delta f\,[\mathrm{Hz}]\right) \tag{A.2}$$

The predominant source of RIN is spontaneous emission. Lasers above their lasing threshold, mostly emit stimulated emission and also a small amount of spontaneous emission. Since the spontaneous emission photons have random wavelength, polarization, direction, and phase, they can coincide with the wavelength and the direction of the stimulated emission photons and produce variations in the output intensity and output frequency of the laser. Depending on the receiver properties in the photodetection process, this beating noise component is detectable if it exceeds the other noise sources in the receiver electronics, which are thermal noise, shot noise of photocurrent, noise from electrical amplifier, noise from electrical spectrum analyzer, etc. Therefore, it is more reasonable to define the intensity noise of the laser after converting it to the electrical domain.

A.1 Intensity noise spectrum

In reality, relative intensity noise is not white noise. The spectrum of the RIN can be written as $\mathrm{RIN}(f) = 2S_P(f)/ < P_0 >^2$, where $S_P(f)$ is the double-sided spectral density of the output power. Since intensity noise typically is proportional to the intensity, the relative intensity noise is typically independent of laser power. Hence, when the signal to noise ratio (SNR) is limited by RIN, it does not depend on laser power. In contrast, when SNR is limited by shot noise, it improves with increasing laser power. RIN typically peaks at the relaxation oscillation frequency of the laser then falls off at higher frequencies until it converges to the shot noise level. The roll off frequency sets what is specified as the RIN bandwidth. RIN is sometimes referred to as a kind of 1/f noise otherwise known as pink noise. Relative intensity noise is measured by sampling the output current of a photodetector over time and transforming this data set into frequency with a fast Fourier transform. The shape of a RIN spectrum of Coherent Monaco at 1035 nm and 2 Mhz repetition rate is depicted in Fig.A.1. The RIN shows a peak at 2 MHz and several peaks due to relaxation oscillations at lower frequencies. Notice that at 1 MHz, the frequency chosen to modulate the pump for SRS detection, the RIN is around -110 dB/Hz.

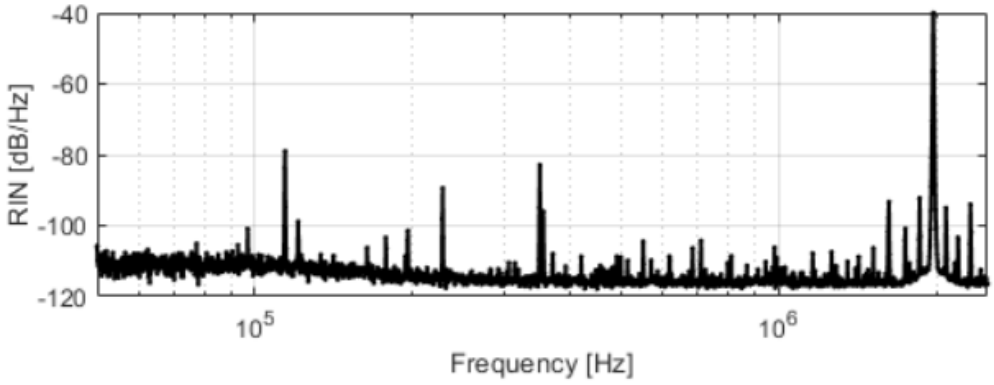

Figure A.1: Relative intensity noise spectrum of Coherent Monaco at 1035 nm and 2 MHz repetition rate with 100 mW average output power. There is a pronounced peak from relaxation oscillations at 2 MHz and excess noise at low frequencies introduced by the pump source.

In the relaxation oscillation, there is a coupling effect between the carrier and photon densities. Thereby any increase in carrier density will increase the optical gain and consequently the photon density. On the other hand, this increase in photon density contributes to more consumption of carriers in the cavity. Thus, the optical gain saturates, which causes the photon density to decrease. This, in turn, increases the carrier density due to reduced saturation effect. This resonance process, so called relaxation oscillation, is strong for a specific frequency which is close to the resonance frequency f_r. For the frequencies much higher than the relaxation oscillation frequency, this coupling effect gradually vanishes and becomes weak. Hence, the intensity noise spectrum increases with frequency and

has the peak around the resonance frequency, f_r, and it decreases again in higher frequencies.

Appendix B

Fabry-Perot Etalon

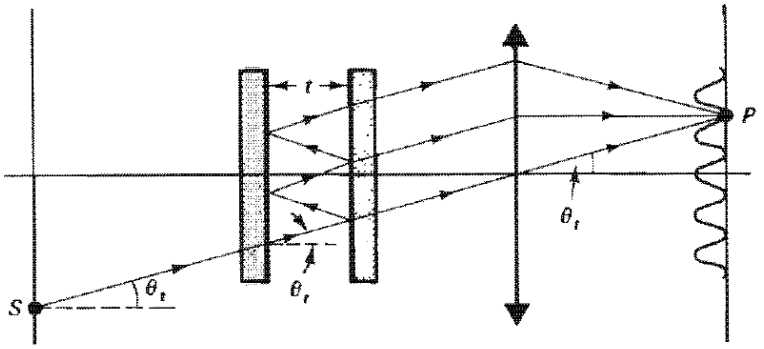

Figure B.1: Fabry-Perot interferometer. Image from [22]

The etalon is a Fabry-Perot interferometer with fixed spacing between the two plane parallel plates [22]. The Fabry-Perot interferometer makes use of two thick glass or quartz plates to enclose a plane parallel "plate" of air between them, which forms the medium within which the beams are multiply reflected. The important surfaces of the glass plates are therefore the inner ones, which are generally polished to a flatness better than $\lambda/50$ and coated with a highly reflective layer of silver or aluminum. Of course the films are thin enough to be partially trasmitting. Optimum thickness for the coating is 50 nm. The outer surfaces are formed at a small angle relative to the inner faces to eliminate spurious fringe patterns that can arise from the glass itself acting as a parallel plate. The spacing of the air gap t is an important parameter of the interferometer.
Consider a narrow, monochromatic beam from a source point S which forms an angle θ_i with respect to the normal to the first surface of the Fabry-Perot interferometer (see Fig.B.1). The emerging set of parallel ray is collimated by a converging in lens in a point P. The condition for brightness, considering an air gap ($n_f = 1$) is:

$$2t \cos \theta_i = m\lambda \tag{B.1}$$

Note that all the beams forming an angle θ_i but starting from different point

sources, will arrive at the same point P. When the thickeness t of the air layer is fixed, Eq.B.1 is satisfied only for certain incident angle θ_i. The variation of the irradiance in the fringe pattern of the Fabry-Perot as a function of the phase or path difference is called *fringe profile*. The sharpness of the fringe is important for the resolving power of the instrument. Indeed, it can been demonstrated [22] that the transmitted intensity of the beams is:

$$I_T = \left[\frac{(1-r^2)^2}{1+r^4-2r^2\cos\delta} \right] I_i \tag{B.2}$$

where r is the reflection coefficient of the inner surfaces of the plate, I_i is the intensity of the incident beam and $\delta = k2t\cos\theta_i$ is the phase difference between successive reflected beams into the air plate. After some manipulation, the *transmittance* T, or *Airy function*, of the interferometer can be expressed as:

$$T = \frac{I_T}{I_i} = \frac{1}{1+F\sin^2(\delta/2)} \tag{B.3}$$

where F is called *coefficient of finesse* and is defined as:

$$F = \frac{4r^2}{(1-r^2)^2} \tag{B.4}$$

From the Airy formula B.3 $T_{max} = 1$ when $\sin(\delta/2) = 0$ and $T_{min} = 1/(1+F)$ when $\sin(\delta/2) = \pm 1$. Note that T_{min} approaches to zero when r approaches to 1, while $T_{max} = 1$ indipendently on r (see Fig.B.2).

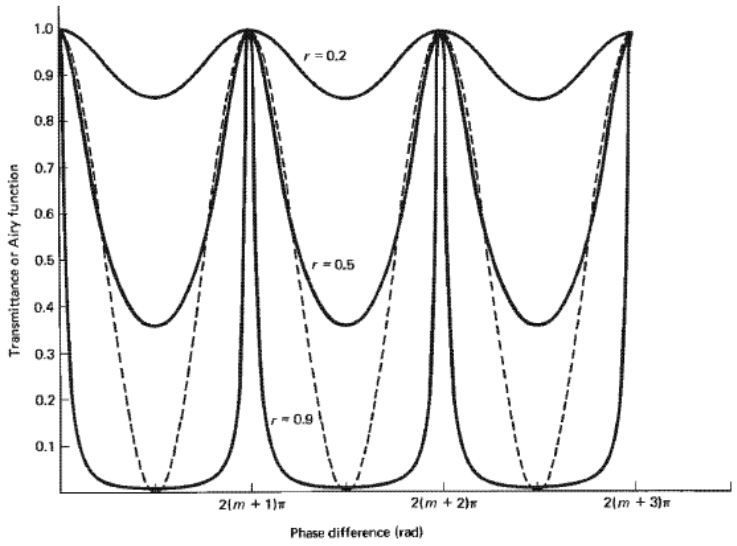

Figure B.2: Airy function or Transmittance of a Fabry-Perot interferometer in function of the phase difference δ. Note that increasing the value of the reflection coefficient r towards 1, T_{min} approaches to zero. Image from [22]

One of the main figure of merit of a Fabry-Perot interferometer is its resolving power which is defined as the ratio between the central wavelength of the beam

and the minimum separation in wavelength that one can distinguish by looking at the Airy patterns associated to two different wavelengths. The criterion which is adopted to estimate the resolving power is the Rayleigh's criterion, which establishes that two wavelengths can be distinguished if the dip caused by identical peaks may not be less than about 20% of the maximum irradiance. Since this criterion cannot be easily applied in this situation, it is sufficient to approximate that criterion by requiering that the crossover point between the two peaks be not more than half the maximum irradiance of either individual peak. This condition from Eq. B.3 implies that:

$$sin\left(\frac{\delta_c}{2}\right) = \frac{1}{\sqrt{F}} \tag{B.5}$$

Since δ_c, which is half of the full width at half maximum of the lobe, will be small, it follows that $\delta_c = 2/\sqrt{F}$. Hence, the minimum phase difference between the two fringe maxima is twice this value:

$$(\Delta\delta)_{min} = \frac{4}{\sqrt{F}} \tag{B.6}$$

It is possible to demonstrate [22] that the corrisponding minimum separation in wavelength you can distinguish is:

$$(\Delta\lambda)_{min} = \frac{2\lambda}{m\pi\sqrt{F}} \tag{B.7}$$

Eventually the resolving power is:

$$\mathcal{R} \equiv \frac{\lambda}{(\Delta\lambda)_{min}} = \left(\frac{\pi}{2}\right) m\sqrt{F}. \tag{B.8}$$

Another important figure of merit of the Fabry-Perot interferometer is the *free spectral range* (fsr) which is defined as the difference in wavelength $\Delta\lambda$ such that the mth order of λ_2 falls on the $(m+1)$ order of λ_1 with $\lambda_2 = \lambda_1 + \Delta\lambda$. It can be easily calculated by imposing that:

$$m\lambda_2 = (m+1)\lambda_1 \tag{B.9}$$

and recalling the relationship between the two wavelengths, we find:

$$(\Delta\lambda)_{fsr} = \frac{\lambda_1}{m} \tag{B.10}$$

To avoid associating fringes of one order with those of the next, then, one should have:

$$\Delta\lambda < \frac{(\Delta\lambda)_{fsr}}{2} \tag{B.11}$$

Notice that a large order m is detrimental to a large fsr (Eq. B.10), whereas it is favorable to good resolution (Eq. B.7). Therefore, for a Fabry-Perot interferometer one would like to maximize the following quantity which is defined simply *Finesse*:

$$\mathcal{F} = \frac{(\Delta\lambda)_{fsr}}{(\Delta\lambda)_{min}} = \frac{\pi\sqrt{F}}{2}. \tag{B.12}$$

Bibliography

[1] Christian W Freudiger, Wei Min, Brian G Saar, Sijia Lu, Gary R Holtom, Chengwei He, Jason C Tsai, Jing X Kang, and X Sunney Xie. *Label-free biomedical imaging with high sensitivity by stimulated raman scattering microscopy.* Science, 322(5909):1857–1861, 2008.

[2] M. Bruchez Jr., M. Moronne, P. Gin, S. Weiss, A. Paul Alivisatos,*Science 1998*,281, 2013.

[3] R. Y. Tsien, *Annu. Rev. Biochem. 1998*,67, 509.

[4] R. Bhargava, *Appl. Spectrosc. 2012*,66, 1091.

[5] G. Turrell, J. Corset, *Raman Microscopy: Developments and Applications*,Academic, Cambridge, MA, USA 1996.

[6] C. Evans, X. S. Xie, *Annu. Rev. Anal. Chem. 2008*, 1, 883.

[7] Cheng Ji-Xin; Xie Xiaoliang Sunney [2013], *Coherent Raman Scattering Microscopy*, Taylor & Francis Group.

[8] Audrius Dubietis; Arnaud Couairon [2019], *Ultrafast Supercontinuum Generation in Trasparent Solid-State Media*, Springer.

[9] Govind P. Agrawal [2002], *Fiber-Optic Communication Systems*, Third edition, John Wiley & Sons.

[10] Andrew M. Weiner [2009], *Ultrafast Optics*, John- Wiley & Sons.

[11] D. Polli; V. Kumar; C.M. Valensise; M. Marangoni; G. Cerullo [2018], *Broadband Coherent Raman Scattering Microscopy*, Laser & Photonics Reviews.

[12] Joseph R. Lakowicz. *Principles of Fluorescence Spectroscopy.* Springer,2006.

[13] Stefan W Hell.*Far-field optical nanoscopy*, 2007.

[14] G L Eesley.*Coherent Raman Spectroscopy.* Journal of Quantitative Spectroscopy Radiative Transfer, 22(6):507–576, 1979.

[15] T. H. Maiman. *Stimulated optical radiation in Ruby.* Nature, 187(4736):493–494, 1960.

[16] Y. R. Shen and N. Bloembergen. *Theory of stimulated brillouin and raman scattering*. Physical Review, 137(6A):A1787–A1805, 1965

[17] N. Bloembergen. *The Stimulated Raman Effect*. American Journal of Physics, 35(11):989–1023, 1967.

[18] R. W. Terhune, P. D. Maker, and C. M. Savage. *Measurements of nonlinear light scattering*. Physical Review Letters, 14(17):681–684, 1965.

[19] R. F. Begley, A. B. Harvey, and R. L. Byer. *Coherent anti-Stokes Raman spectroscopy*. Applied Physics Letters, 25(7):387–390, 1974.

[20] Conor L. Evans and X. Sunney Xie. *Coherent Anti-Stokes Raman Scattering Microscopy: Chemical Imaging for Biology and Medicine*. Annual Review of Analytical Chemistry, 1(1):883–909, 2008.

[21] Anthony Anderson and Chandrasekhara Venkata Raman. *The Raman effect*. M. Dekker, 1971.

[22] Frank L.Pedrotti; Leno S. Pedrotti [1993], *Introduction to Optics*, Prentice-Hall, Second Edition.

[23] R. W. Hellwarth. *Theory of stimulated raman scattering*. Physical Review, 130(5):1850–1852, 1963.

[24] Wei Min, Christian W. Freudiger, Sijia Lu, and X. Sunney Xie. *Coherent Nonlinear Optical Imaging: Beyond Fluorescence Microscopy*. Annual Review of Physical Chemistry, 62(1):507–530, 2011.

[25] M. Muller, J. M. Schins, J. *Phys. Chem. B 2002*, 106, 3715.

[26] J. X. Cheng, A. Volkmer, L. D. Book, X. S. Xie, J. *Phys. Chem. B 2002*,106, 8493.

[27] T. W. Kee, M. T. Cicerone, *Opt. Lett. 2004*, 29, 2701.

[28] H. Kano, H. Hamaguchi. *Appl. Phys. Lett.2005*, 86, 121113.

[29] H. Kano, H. Hamaguchi,*Opt. Express 2005*, 13, 1322.

[30] B. G. Saar, C.W. Freudiger, J. Reichman, C. M. Stanley, G. R. Holtom,X. S. Xie, *Science 2010*, 330, 1368.

[31] H. T. Beier, G. D. Noojin, B. A. Rockwell, *Opt. Express 2011*, 19, 18885.

[32] E. R. Andresen, P. Berto, H. Rigneault, *Opt. Lett. 2011*, 36, 2387.

[33] C. W. Freudiger, W. Min, G. R. Holtom, B. Xu, M. Dantus, X. S. Xie,*Nat. Photonics 2011*, 5, 103.

[34] Y. Ozeki, W. Umemura, Y. Otsuka, S. Satoh, H. Hashimoto, K. Sumimura,N. Nishizawa, K. Fukui, K. Itoh, *Nat. Photonics 2012*, 6, 845.

[35] A. Perri, B. E. Noguiera De Faria, D. C. Teles Ferreira, D.Comelli, G. Valentini, F. Preda, D. Polli, A. M. De Paula, G.Cerullo, C. Manzoni. *Hyperspectral imaging with a TWINS birefringent interferometer*, Optics Express, 2019.

[36] B. Liu, H. J. Lee, D. Zhang, C. S. Liao, N. Ji, Y. Xia, J.-X. Cheng, *Appl. Phys. Lett. 2015*, 106, 173704.

[37] D. Huang, E. A. Swanson, C. P. Lin, J. S. Schuman,W. G. Stinson,W.Chang, M. R. Hee, T. Flotte, K. Gregory, C. A. Puliafito, J. G. Fujimoto,*Science 1991*, 254, 1178.

[38] F. Saltarelli, V. Kumar, D. Viola, F. Crisafi, F. Preda, G. Cerullo, D.Polli,*Opt. Express 2016*, 24, 21264.

[39] S. Dobner, C. Fallnich, *Appl. Phys. B 2016*, 122, 278.

[40] A. Papoulis,*Signal Analysis*. McGraw-Hill, New York 1977.

[41] P. Polynkin, M. Kolesik, *Critical power for self-focusing in the case of ultrashort laser pulses*.Phys. review A 87, 053829 (2013).

[42] R. Trebino and D. J. Kane. *Using phase retrieval to measure the intensity and phase of ultrashort pulses: frequency-resolved optical gating*. J. Opt. Soc. Am. A, 10(5):1101–1111,1993.

[43] Braun A., Korn G., Liu X., Du D., Squier J., Mourou G.. *Self-channeling of high-peak powerfemtosecond laser pulses in air*. Opt. Lett. 20, 73–75 (1995).

[44] Tzortzakis, S., Sudrie, L., Franco,M., Prade, B., Mysyrowicz, A., Couairon, A., Bergé, L..*Selfguided propagation of ultrashort IR laser pulses in fused silica*. Phys. Rev. Lett. 87, 213902(2001).

[45] Anne-Laure Calendron, Hüseyin Çankaya, Giovanni Cirmi,Franz X. Kärtner. *White-light generation with sub-ps pulses*. Opt. Express. 10.1364/OE.23.013866, 2015.

[46] Julien Réhault, Margherita Maiuri, Cristian Manzoni, Daniele Brida, Jan Helbing, and Giulio Cerullo. *2D IR spectroscopy with phase-locked pulse pairs from a birefringent delay line*. Opt. Express, 22(8):9063–9072, 2014.

[47] Julien Réhault, Margherita Maiuri, Aurelio Oriana, and Giulio Cerullo. *Two-dimensional electronic spectroscopy with birefringent wedges*. Review of Scientific Instruments, 85(12):123107, 2014.

[48] Julien Réhault, Francesco Crisafi, Vikas Kumar, Gustavo Ciardi, Marco Marangoni, Giulio Cerullo, Dario Polli. *Broadband stimulated Raman scattering with Fourier-transform detection*, 10.1364/OE.23.025235.Opt. Express 25235, 2015.

[49] Güneş Açikgöz, Berna Hamamci, Abdulkadir Yildiz. *Determination of Ethanol in Blood Samples Using Partial Least Square Regression Applied to Surface Enhanced Raman Spectroscopy*. Toxilogical Res. 2018.

[50] Peter R. Griffiths, James A. de Haseth. *Fourier Transform Infrared Spectrometry*. Second edition, John Wiley & Sons, inc., publication, 2007.

[51] L. A. Coldren and S. W. Corzine. *Diode lasers and photonics integrated circuits*. John Wiley sons, New York, USA, 1995.

[52] *Lightwave signal analyzers measure relative intensity noise*. Product Note 71400-1, Agilent Technologies, 2000.

[53] RP Photonics Encyclopedia, *Relative Intensity Noise*.

[54] *www.thorlabs.com*. Non-zero dispersion shifted SMF.

[55] *www.thorlabs.com*. DMLP1000.

[56] *www.semrock.com*. di02-r1064-25x36.

[57] *www.sacher-laser.com*

[58] *National Institute of Standards and Technology (NIST)*. Chemistry WebBook, SRD 69.